ALMA MATER STUDIORUM
UNIVERSITÀ DI BOLOGNA

DOTTORATO DI RICERCA IN

IL FUTURO DELLA TERRA, CAMBIAMENTI CLIMATICI E SFIDE SOCIALI

Ciclo 36

Settore Concorsuale: 04/A4 - GEOFISICA

Settore Scientifico Disciplinare: GEO/12 - OCEANOGRAFIA E FISICA DELL'ATMOSFERA

ANALYSIS OF THE EFFECTS OF BAROTROPIC AND INTERNAL TIDES ON THE MEDITERRANEAN SEA DYNAMICS THROUGH NUMERICAL EXPERIMENTS

Presentata da: Bethany Alice McDonagh

Coordinatore Dottorato

Silvana Di Sabatino

Supervisore

Emanuela Clementi

Co-supervisore

Nadia Pinardi

Esame finale anno 2024

Abstract

Tides in the Mediterranean Sea are low in amplitude compared to many regions of the global ocean, but they have impacts beyond their own temporal and spatial scales, affecting temperature, salinity, currents, and vertical mixing. Additionally, due to the complex geometry and bathymetry of this semi-enclosed basin, they can generate intense and complex internal waves. A numerical modelling approach can be used to investigate these impacts and understand the scales at which tides affect the Mediterranean Sea dynamics. Twin experiments using a high-resolution general circulation model of the Mediterranean Sea, with and without tides, were used for this initial investigation. It was found that tides amplify several basin and sub-basin modes (seiches) of the Mediterranean Sea, and their effects on kinetic energy are nonlinear, including interactions between baroclinic tides and near-inertial internal waves. Tides also increase the mixed layer depth of the Mediterranean Sea and increase the western Mediterranean deep water formation rates. Following this initial study, the vertical motion and mixing results were analysed in more detail. Firstly, sensitivity tests modifying the bathymetry of the Gibraltar Strait were carried out to improve the representation of vertical motion and mass transport in the region, finding that a smoothed bathymetry in the Gibraltar Strait gives the most accurate mass transport, thus highlighting the need for a well-considered numerical set-up to represent this region. Secondly, a mixing scheme based on a turbulent kinetic energy closure model was compared to a Richardson number-based control parameterization. Despite having improved physics, the turbulent kinetic energy scheme can only match, but not improve upon, the accuracy of temperature and salinity representation in the model when comparing with observations, thus suggesting the need to perform dedicated experiments testing alternative vertical mixing parameterizations. Finally, a further set of experiments were carried out to

map the generation sites and regions of propagation of internal tides at the Mediterranean Sea basin level. Implementations of two numerical models, NEMO and ICON-O, were used, unveiling the effects of internal tides in the Mediterranean Sea in more detail. Internal tides are primarily generated in the Gibraltar Strait, the Sicily Strait/Malta Bank, and the Hellenic Arc regions. Long-distance propagation of semidiurnal internal tides on the scale of hundreds of kilometres was discovered, affecting mainly the Algerian Sea, Tyrrhenian Sea, and Ionian Sea. Additionally, bottom-trapped diurnal internal tides are found in several regions. The models depict two modes of the M2 internal tide and three modes of the K1 internal tide, as revealed by wavenumber spectra. The two models show similar regions of internal tide generation and propagation, but are not identical, which is attributed to differences in modelling set-up, stratification, bathymetry, and the barotropic tidal forcing implemented in the models.

Acknowledgements

There are many people who supported me during these three years, without whom I wouldn't have been able to complete this thesis. I'd like to begin by thanking my supervisors Emanuela Clementi and Nadia Pinardi, who endlessly supported me with their expertise, feedback, and advice. I am very grateful to have been given the freedom to always pursue the most interesting science throughout my PhD, and I could not have asked for better supervisors.

I want to sincerely thank my colleagues at CMCC and the University of Bologna, particularly Anna Chiara Goglio, who shared with me her huge knowledge about tides and their implementation in NEMO, and contributed to the paper. Thank you also to Aimie Moulin and Federica Borile, for giving me advice and technical help whenever I asked. Thank you to Paola Cessi for helping me understand why details are important and for helping me to refine my work on tides, making it what it is today. Thank you also to Paolo Oddo who generously shared his knowledge on internal tides in the Mediterranean Sea and advised me on many occasions.

I would like to thank everybody who welcomed me for my visit to the Max Planck Institute for Meteorology in Hamburg. In particular, I would like to acknowledge the support of Jin-Song von Storch, who welcomed me into her research group and shared her expertise on internal tides, supporting the study on internal tides in the Mediterranean Sea. Thank you also to the Climate Energetics group for providing feedback on my work, and to the colleagues who made my stay in Hamburg much more enjoyable.

Thank you to the other PhD students at CMCC and the wider group of colleagues, who were always there for coffee breaks, advice, and support during this journey, and especially to the amazing women with whom I have shared an office during these years.

Thank you also to Robin Waldman and Jin-Song von Storch for giving their time to review this thesis, leading to the improved version that you see today.

Many people from outside the world of oceanography also supported me. I would like to

thank my parents, Linda and Malcolm, for their unconditional support and encouragement, my siblings Rhiannon and Travis, and all of my family, especially my grandmother Maeve, who made me always want to visit home. Thank you to my friends in the UK who were always at the other end of the phone, and a special thank you to the Funzone, for ten years of fun.

I never believed I could feel so at home in a place so far away, and for this I have many friends to thank. Thank you to Francesco Leva, who was the first person to tell me that Bologna is a great place to live and for helping me get started here, from the very first day. Thank you to the friends I made in Bologna, who were there for me through the best days and the most difficult times.

This thesis is dedicated to the memory of my wonderful aunts Pauline Kelly and Patricia Keaney.

Contents

Chapter 1: Introduction

1.1 The Mediterranean Sea

The Mediterranean Sea is a semi-enclosed basin, located between the land regions of southern Europe, northern Africa, and the Middle East, covering the region of 6°W–36°E, and 30°–46°N. It is enclosed by a western entrance at the Gibraltar Strait, connecting with the Atlantic Ocean, and to the east by the Dardanelles Strait, connecting the Mediterranean Sea with the Marmara Sea, Bosphorus Strait, and the Black Sea. Figure 1.1 shows a map of the Mediterranean Sea, highlighting some key regions.

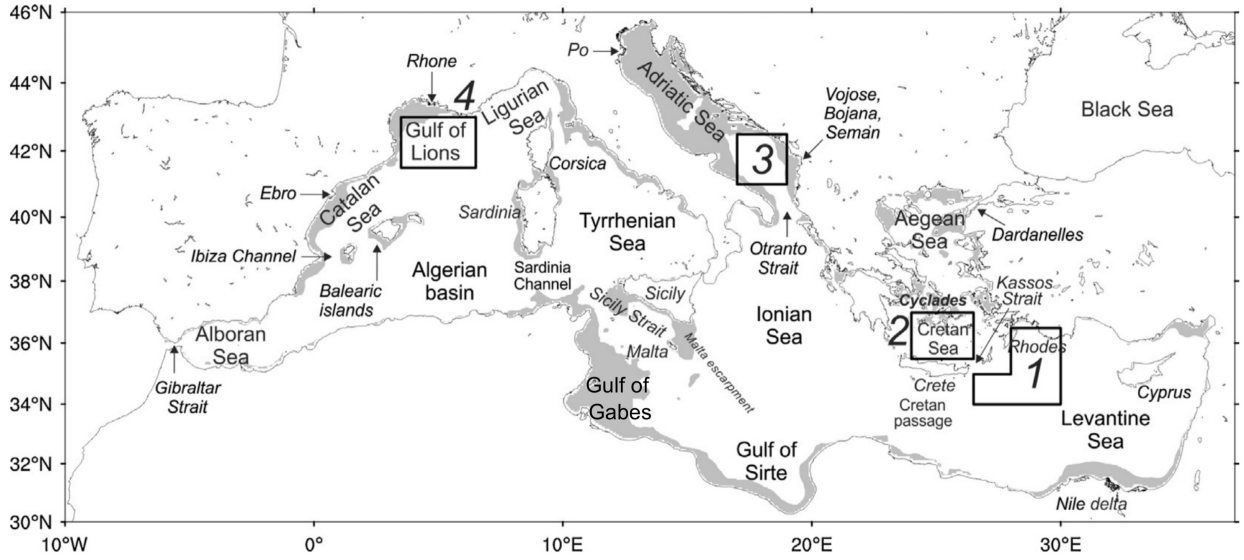

Figure 1.1: Map of the Mediterranean Sea, highlighting major seas, rivers, islands, straits, and regions of open-ocean deep water formation (1. Rhodes Gyre, 2. Cretan Sea, 3. South Adraitic Sea, and 4. Gulf of Lions). Grey areas identify shelf regions. Adapted from Pinardi et al. (2015).

Forecasting the Mediterranean Sea, both in the short and long term, impacts the lives and livelihoods of its population of over 500 million, many of whom live close to the coast and in regions which are vulnerable to the impacts of climate change, including sea-level rise, desertification, and damage to ecosystems (Ali et al., 2022). Accurate forecasting on shorter timescales is needed to predict impacts of storms at the coasts such as medicanes

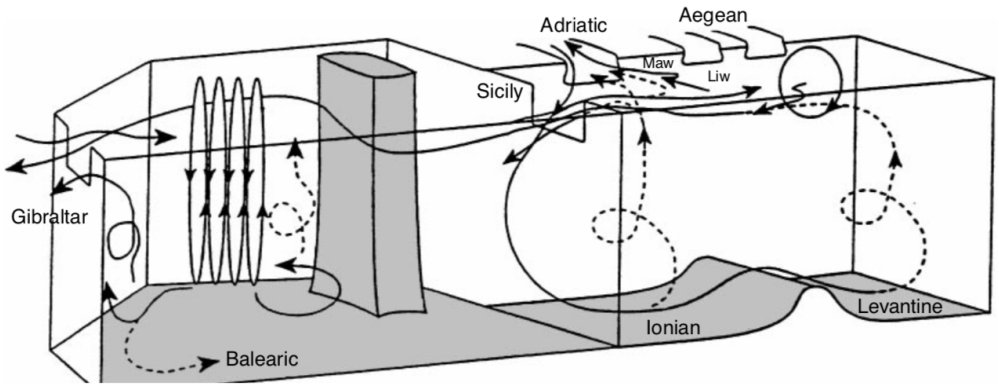

Figure 1.2: Schematic of the overturning circulation in the Mediterranean Sea, from Robinson et al. (2001).

(Di Muzio et al., 2019; Maicu, 2023), as well as marine heatwaves (Jacox et al., 2022), and for extreme sea level events in urban areas such as the Venice Acqua Alta (Bertotti et al., 2011).

The Mediterranean Sea region has several unique features which make it interesting as a region of study from the perspective of ocean dynamics. The Mediterranean Sea has its own overturning circulation, described first by Wüst (1961) and more recently by Waldman et al. (2018) and Pinardi et al. (2019). This vertical circulation is summarised in Figure 1.2. The Mediterranean Sea overturning circulation is important for the production of deep and intermediate waters in the Mediterranean Sea, which exit into the Atlantic Ocean in the form of saline intermediate waters (Mauritzen et al., 2001). The principal regions for open ocean deep water formation in the Mediterranean Sea are the Gulf of Lions, South Adriatic Sea, Cretan Sea, and Rhodes Gyre (Pinardi et al., 2015) (see Figure 1.1).

The mean horizontal circulation of the Mediterranean Sea is shown in Figure 1.3. The surface level currents show the principal inflowing current from the Gibraltar Strait along the African coast, and a rich field of gyres and eddies in the basin. At the intermediate levels (Figure 1.3B), the currents are weakened and reversed, with waters exiting through the Gibraltar Strait.

Moreover, the semi-enclosed shape of the Mediterranean Sea allows for free barotropic oscillations to resonate in the basin, which are induced by wind and atmospheric pressure forcing. The first four basin modes are at 38.8, 11.4, 8.4, and 7.4 hours according to Schwab and Rao (1983), and at 8 hours according to Lamy et al. (1981) and Lozano and

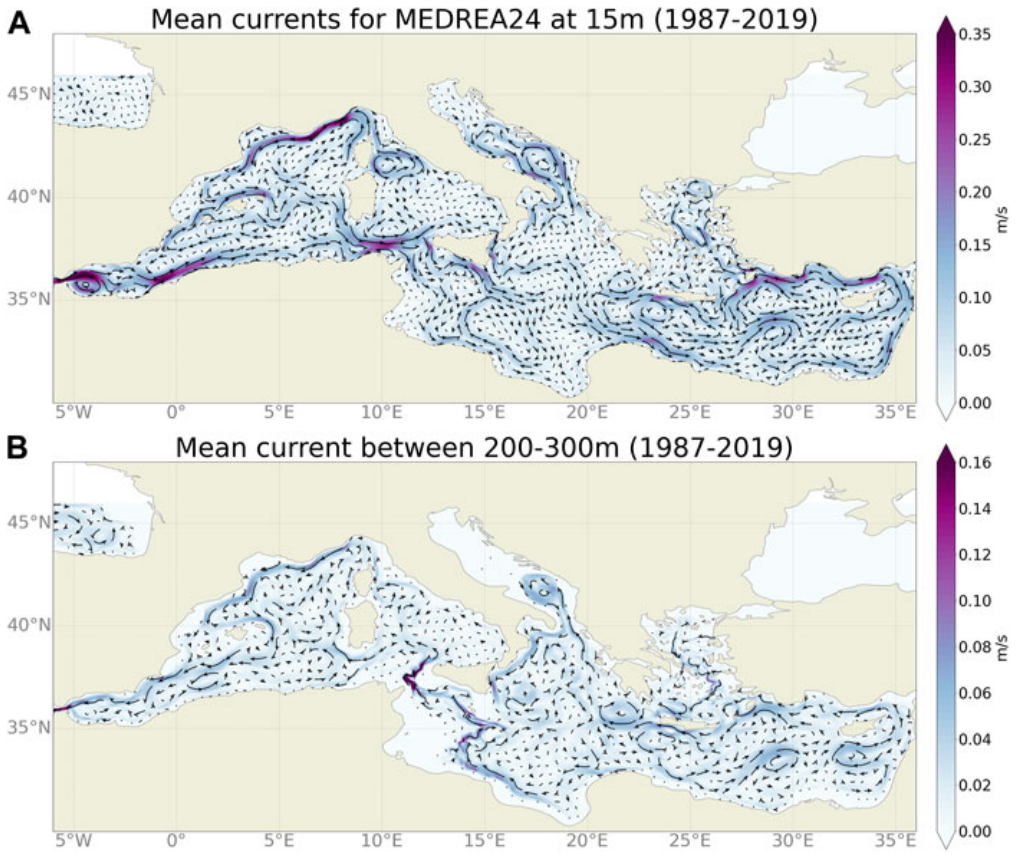

Figure 1.3: Mean horizontal circulation of the Mediterranean Sea at 15m and 200-300m in the period 1987-2019, from reanalysis by Escudier et al. (2021).

Candela (1995). In particular, the semi-enclosed Adriatic Sea has its own modes at 12.0 hours (Lozano and Candela, 1995), and 21.9 and 10.7 hours (Schwab and Rao, 1983; Leder and Orlić, 2004; Medvedev et al., 2020). These oscillations have the potential to interact with other phenomena at similar frequencies, such as tides.

The Mediterranean Sea is a basin with net evaporation: more water evaporates from the surface than the sum of inputs from rivers and precipitation. This means that the net transport through the Gibraltar Strait is slightly positive, in order to maintain a constant volume of the basin (Soto-Navarro et al., 2010). The major rivers that flow into the Mediterranean Sea are indicated in Figure 1.1, and include the Rhône, Po, Ebro, and Nile.

In the following sections, the scope of this thesis is further defined through a discussion of the role of tides in the Mediterranean Sea. Furthermore, the Gibraltar Strait and its importance to the circulation and tides in the Mediterranean Sea is discussed in detail in Section 1.3.

1.2 Tides and the Mediterranean Sea

1.2.1 Barotropic and baroclinic tides

Tides are the periodic movement of the sea surface due to the gravitational forces between the Earth and the Sun and Moon, and have been an interest of scientists and philosophers for many centuries (Cartwright, 1999). These are generally referred to as surface tides or barotropic tides. Tides contribute 3.5 TW of energy to the ocean (Munk and Wunsch, 1998), the second-largest component after wind waves. Figure 1.4 shows a diagram of some of the main sources of energy in the global ocean with their associated magnitudes.

Internal tides, or baroclinic tides, are generated when barotropic tides interact with topography, including ridges and narrow straits, contributing 1.0 TW of energy to the ocean (Egbert and Ray, 2003). Internal tides can then dissipate close to the generation site, or propagate away, for up to thousands of kilometres in some parts of the global ocean, as demonstrated by e.g. Arbic et al. (2010) and Li et al. (2015). Generally, the lower modes

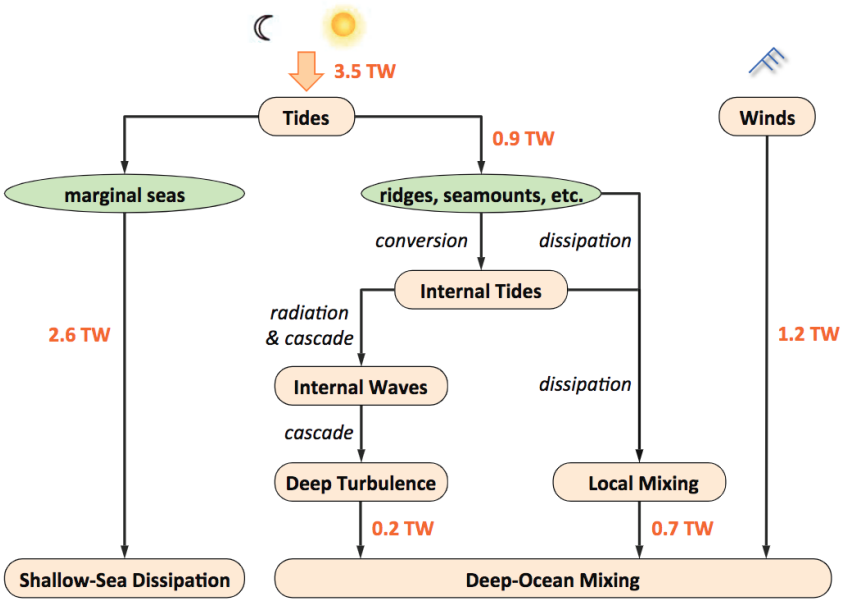

Figure 1.4: Global energy flux budget based on Munk and Wunsch (1998), from Kang (2012).

of internal tides are able to propagate away from their generation sites, while higher modes dissipate at the topography. The ability of internal tides to propagate over long distances also depends on latitude: the frequency of the tide must be higher than the inertial frequency. For semidiurnal internal tides, this condition is met up to 74.5°N/S, while diurnal internal tides can only propagate in the tropics, up to 30°N/S. Baroclinic tides are also important for deep ocean mixing (Munk and Wunsch, 1998).

1.2.2 Tides and vertical mixing

Vertical mixing maintains the global overturning circulation of the ocean (Gent, 2018), but many of the involved processes, such as internal tide energy dissipation, wave-wave interactions, and wave breaking are not well understood (Fox-Kemper et al., 2019). Coastal regions are particularly challenging for vertical mixing parameterizations (Durski et al., 2004), and the relationship between tides and vertical mixing in the Mediterranean Sea is not well-known.

In some regions of the global ocean, the relationship between tides and vertical dynamics has been investigated using numerical experiments, notably in the North Atlantic (Lee

et al., 2006; Müller et al., 2010) and the Indonesian Seas (Nagai and Hibiya, 2015). In the North Atlantic, the presence of tides was found to improve representation of the mixed layer depth and deep water formation in the Labrador Sea (Müller et al., 2010). Lee et al. (2006) found that in the same region, sea surface density was increased by the addition of tides to their model, and found that this could enhance ventilation and overturning in the region. Lee et al. (2006) also found that ventilated water is up to six years younger in the Labrador Sea in their tidal model compared to their model without tides. In the Indonesian seas, Nagai and Hibiya (2015) investigated parameterizations of vertical diffusivity, and stressed the importance of internal wave propagation in models in order to correctly represent vertical diffusivity in the far-field, meaning that the inclusion of tides in models is important in choosing a vertical diffusivity parameterization. Another region where the vertical effects induced by tides have been researched is the Bay of Biscay/English Channel, which are areas characterised by particularly high amplitude tides. Karagiorgos et al. (2020) found that the Brunt-Väisälä frequency is reduced in the English Channel in summer, and stratification is reduced to near-zero in spring, summer, and autumn in their tidal model compared to a simulation without tides.

1.2.3 Tides in the Mediterranean Sea

Tides in the Mediterranean Sea are typically of lower amplitude compared to many regions in the Atlantic and Pacific Oceans, and notably are much lower than the amplitudes of tides in the north-east Atlantic Ocean, geographically close to the Mediterranean Sea (Tsimplis et al., 1995). There are several reasons for this: tides entering from the Atlantic Ocean are modulated by the Strait of Gibraltar (Candela et al., 1990), the relatively small scale of the basin, and the existence of several amphidromic points of the major tidal components in the basin. Figure 1.5 shows tidal amplitude from the TPXO9 model (Egbert and Erofeeva, 2002) for the four largest tidal components in the Mediterranean Sea. Some exceptions to the low amplitudes are visible from this amplitude/phase map: the Gibraltar Strait/Alboran Sea, the North Adriatic Sea, and the Gulf of Gabes (labelled in Figure 1.1), where amplitudes are considerably higher. These regions have higher tidal amplitudes for a variety of reasons: in the Alboran Sea, the tidal signal propagates from the Atlantic Ocean

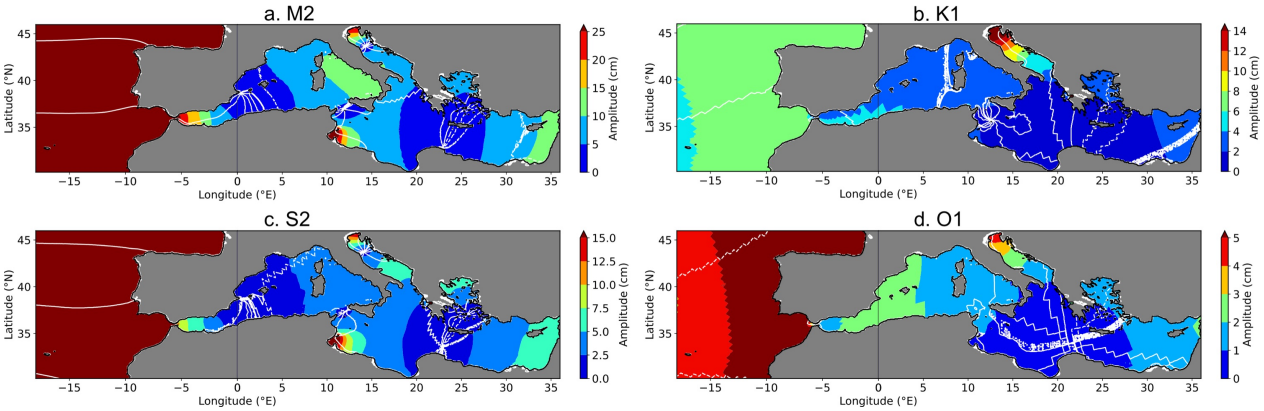

Figure 1.5: Tidal amplitude and phase of the principal four tidal components: a. M2, b. K1, c. S2, and d. O1, in the Mediterranean Sea and Atlantic Box, from TPXO9 data (Egbert and Erofeeva, 2002).

(Candela et al., 1990)), while in the North Adriatic Sea and Gulf of Gabes, it is generated by the interaction of tides with topography. In particular, in the North Adriatic Sea, both the diurnal K1 and semidiurnal M2 tides have higher amplitude, resulting in higher tides overall. In addition, tides interact with barotropic oscillations, which are present close to tidal frequencies in this region (Medvedev et al., 2020), leading to resonance between the tides and these modes. Similarly, barotropic mode frequencies are close to tidal frequencies in the Gulf of Gabes region (Lozano and Candela, 1995).

Tides in the Mediterranean Sea have impacts far beyond the regions of higher tidal amplitude. In the Gibraltar Strait, the importance of tidal forcing has been highlighted by many works including Armi and Farmer (1985), Candela et al. (1990), and Harzallah et al. (2014). Tides increase the baroclinic transport at the Gibraltar Strait, increase the incoming salinity and decrease the incoming temperature (Naranjo et al., 2014; Harzallah et al., 2014), and affect the outflowing waters into the Atlantic Ocean (Izquierdo and Mikolajewicz, 2019). Tides also increase the deep water mass formation in the Western Mediterranean (Naranjo et al., 2014).

Internal tides have been observed in the Mediterranean Sea, in limited regions, through observational studies from cruises and regional modelling studies. These regions include the Gibraltar Strait (Candela et al., 1990; Morozov et al., 2002) and the central Mediterranean Sea (Oddo et al., 2023). Internal tides have not been observed in many other regions of the Mediterranean Sea, and their propagation over long distances, as seen in the Pacific Ocean

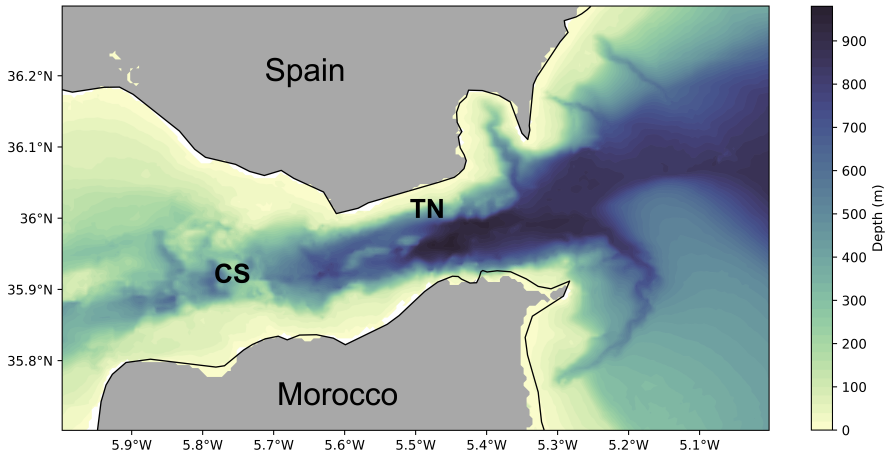

Figure 1.6: Bathymetry in the Gibraltar Strait region, from GEBCO Bathymetric Compilation Group 2014 (2014). Key topographic features of the Camarinal Sill (CS) and Tarifa Narrows (TN) are labelled.

(Zhao et al., 2010) and Atlantic Ocean (Lahaye et al., 2020), has not been observed, as no previous literature has analysed this phenomenon for most of the Mediterranean Sea.

1.3 The Gibraltar Strait

The Gibraltar Strait is a narrow strait connecting the Mediterranean Sea to the Atlantic Ocean, being around 14km wide at its narrowest point in the Tarifa Narrows, and 300m deep at its shallowest point in the Camarinal Sill. As it is the main connection with the rest of the global ocean, it is a particularly important region when modelling the Mediterranean Sea. The Gibraltar Strait, as mentioned in Section 1.1, modulates the Mediterranean overturning circulation, and is a source of fresh water into the Mediterranean Sea, as well as an exit point for salty Mediterranean Intermediate Water into the Atlantic Ocean (Pinardi et al., 2006; Sannino et al., 2009). The upper 150m of the Gibraltar Strait is typically dominated by the inflow of fresh Atlantic water, while the lower layer is made up of the cooler and saltier Mediterranean water. Figure 1.6 shows a map of the Gibraltar Strait region and its key topographic features.

Tidal velocity is particularly high in the Gibraltar Strait compared to the rest of the Mediterranean Sea, due to its proximity to the large tidal amplitude regions of the northeastern Atlantic Ocean. The importance of tides in the Gibraltar Strait has been discussed in Vázquez

et al. (2006), Sánchez-Román et al. (2012), García Lafuente et al. (2013), and Hilt et al. (2020). Tides are mainly semidiurnal in the region (Candela et al., 1990), and induce intense vertical mixing (Armi and Farmer, 1985; Gonzalez et al., 2023).

The vertical dynamics of the Gibraltar Strait are complex and depend on a series of tidally-driven hydraulic controls (Armi and Farmer, 1985; Farmer et al., 1988)); the tidal mixing is driven primarily by vertical shear and stratification (Gonzalez et al., 2023), and is further enhanced by internal tides that have amplitudes which can be as large as the entire depth of the Strait. Internal tides are generated at the Camarinal Sill, largely from the M2 component (Morozov et al., 2002).

Modelling the Gibraltar Strait is an ongoing challenge due to its complex bathymetry and dynamics, and a sub-kilometric horizontal resolution is generally required to capture the topography and dynamics well (Sannino et al., 2009). Nested models of $\frac{1}{24}^\circ$ (around 4km) have been used by Sannino et al. (2009), and this nested model improved representation compared to lower resolutions, but still leaves only four horizontal ocean grid points in the narrowest part of the Strait. Even higher horizontal resolutions of around 500m, such as the regional model used by Sánchez-Román et al. (2009), are needed to reproduce all characteristics of the Gibraltar Strait region. High resolution experiments on the whole Mediterranean Sea used by Soto-Navarro et al. (2015) found that a high resolution model of $\frac{1}{36}^\circ$ outperformed models with $\frac{1}{12}^\circ$ and $\frac{1}{8}^\circ$, and better represents the thermohaline circulation in the Mediterranean and the outflow through the Gibraltar Strait.

1.4 Scope of the work

Across the related areas described in the preceding sections, several questions arise. Firstly, although it is clear that tides have an impact on the Mediterranean Sea dynamics, the full extent of this needs to be further investigated, including the analysis of the processes and phenomena with which tides interact, and the temporal and spatial scales at which this occurs. Furthermore, the status of internal tides in the majority of the Mediterranean Sea is not known, and mapping the areas of their generation and propagation would improve our understanding of their distribution and how they may affect vertical motion and mixing

across the basin.

Based on this, this work addresses the following questions:

1. How do tides affect the wider Mediterranean Sea dynamics? (Harzallah et al., 2014; Naranjo et al., 2014; Sannino et al., 2014; Gonzalez et al., 2023; Oddo et al., 2023)
2. Are the effects of tides limited to certain temporal and spatial scales, or do they have an impact across many scales? (Müller et al., 2010; Pinardi et al., 2015, 2019; Arbic, 2022)
3. Do tides interact with other phenomena in the Mediterranean Sea, such as barotropic basin modes and internal waves? (Lozano and Candela, 1995; Medvedev et al., 2020; Palma et al., 2020)
4. Are internal tides ubiquitous in the Mediterranean Sea? If so, where are the generation and propagation sites? (Armi and Farmer, 1985; Morozov et al., 2002; Gasparini et al., 2004; Alford et al., 2012; Oddo et al., 2023)

To address these questions, a numerical modelling approach is used, based on a suite of experiments, all but one of which use the NEMO v3.6 general circulation model, following the implementation of the Mediterranean Sea forecasting system operational in the framework of the Copernicus Marine Service (Clementi et al., 2021; Coppini et al., 2023). The first experiments investigate the effects of tides compared to a twin experiment without tides. Following this, four experiments were run with bathymetry changes in the Gibraltar Strait, as well as several experiments with modified vertical mixing schemes. Finally, two month-long experiments with hourly outputs were run to investigate the effects of internal tides in the Mediterranean Sea: one of which uses NEMO with the best-performing vertical mixing scheme and bathymetry from the previous experiments, while the other uses a different numerical model, ICON-O, a high-resolution global hydrodynamic model of the ocean. A full list of these experiments and their differences is available in Chapter 2.

Analysis of the effects of tides on the wider dynamics of the Mediterranean Sea leads to a better understanding of the temporal and spatial scales at which tides are important, and

which processes and phenomena in the Mediterranean Sea are impacted by their interactions with tides. Following this, sensitivity tests towards a reconfiguration of the Gibraltar Strait bathymetry to improve the mass transport, and the use of a more sophisticated vertical mixing scheme are conducted. These model improvements mean that internal tides, a process that is found to be important in the initial study of tides in the Mediterranean Sea, are likely to be better represented in the model. The study of internal tides then maps, for the first time, the generation sites and propagation regions of internal tides in the Mediterranean Sea.

The rest of the thesis is organised as follows: Chapter 2 details the model configuration, the experiments carried out, and the analysis done, and then shows results of the sensitivity experiments on the Gibraltar Strait bathymetry and vertical mixing parameterizations. Both of these sensitivity tests lead to model changes implemented in the final experiments. Chapter 3 contains a manuscript, "The characteristics of tides and their effects on the general circulation of the Mediterranean Sea", which addresses the questions regarding the impacts of tides on the Mediterranean Sea dynamics (questions 1-3). The modified model set-up is used for the final experiments of Chapter 4, which analyses the presence of internal tides in the Mediterranean Sea (question 4), using both the improved model from Chapter 2, and a second global hydrodynamic model of the ocean. Finally, Chapter 5 summarises the results and returns to answer the scientific questions above.

Chapter 2: Model and methods

2.1 Description of experiments

Table 2.1 contains a list of all experiments that are performed within this work, with some top-level details about the key differences between each one, and the chapters in which their outputs are analysed. Some experiments are carried forward from one chapter to the next, to be compared with the next suite of experiments, and are therefore discussed in multiple chapters. Detailed information about each specific experiment configuration is in its respective chapter, while the next section contains an overview of the NEMO model and the features of note that are common to all experiments.

All the NEMO experiments detailed in Table 2.1 were performed specifically for this thesis, while the ICON dataset was provided by the Climate Energetics group at the Max Planck Institute for Meteorology, Hamburg, Germany. For this thesis, the global output of ICON was interpolated onto the same grid as the NEMO experiments. More information about ICON is available in Chapter 4.

2.2 NEMO model configuration

All experiments other than "Internal tides (ICON)" (final row of Table 2.1) use principally the same configuration of NEMO v3.6, which provides the ocean component of the operational Mediterranean Sea Forecasting System within the Copernicus Marine Service, MedFS Coppini et al. (2023); Clementi et al. (2021). No experiments are coupled to other Earth system components (all experiments are ocean-only), and data assimilation is not used in any experiments.

The implementation of NEMO used for all experiments is a model of the Mediterranean Sea with an additional Atlantic box, using lateral open boundary conditions in the Atlantic box and Dardanelles Strait, which come from a global NEMO model (Galloudec et al., 2022),

Name	Chapter(s)	Date range	Model	Bathymetry	Vertical mixing scheme
Model without tides	3, 2.3	2017-2021	NEMO	As in MedFS	Richardson number-based
Tidal model	3, 2.3	2017-2021	NEMO	As in MedFS	Richardson number-based
Bathymetry Test 1	2.3	2017-2019	NEMO	Modified (see Section 2.3)	Richardson number-based
Bathymetry Test 2	2.3	2017-2021	NEMO	Modified (see Section 2.3)	Richardson number-based
Bathymetry Test 3	2.3, 2.4	2017-2021	NEMO	Modified (see Section 2.3)	Richardson number-based
Bathymetry Test 4	2.3	2017-2019	NEMO	Modified (see Section 2.3)	Richardson number-based
TKE 1	2.4	2017-2019	NEMO	As in Bathymetry Test 3	TKE scheme (varied parameters)
TKE 2	2.4	2017-2019	NEMO	As in Bathymetry Test 3	TKE scheme (varied parameters)
TKE 3	2.4	2017-2019	NEMO	As in Bathymetry Test 3	TKE scheme (varied parameters)
TKE 4	2.4	2017	NEMO	As in Bathymetry Test 3	TKE scheme (varied parameters)
TKE 5	2.4	2017	NEMO	As in Bathymetry Test 3	TKE scheme (varied parameters)
TKE 6	2.4	2017	NEMO	As in Bathymetry Test 3	TKE scheme (varied parameters)
TKE 7	2.4	2017	NEMO	As in Bathymetry Test 3	TKE scheme (varied parameters)
TKE 8	2.4	2017	NEMO	As in Bathymetry Test 3	TKE scheme (varied parameters)
Internal tides (NEMO)	4	March 2022	NEMO	As in Bathymetry Test 3	As in TKE 3
Internal tides (ICON)	4	March 2022	ICON	ICON standard bathymetry	TKE scheme (ICON parameters)

Table 2.1: List of experiments for the entire thesis, detailing their names, chapters and sections where their results are analysed, date range of outputs, numerical model, and overviews of bathymetry and vertical mixing scheme. More details of the bathymetry variations and vertical mixing scheme parameters are found later in this chapter.

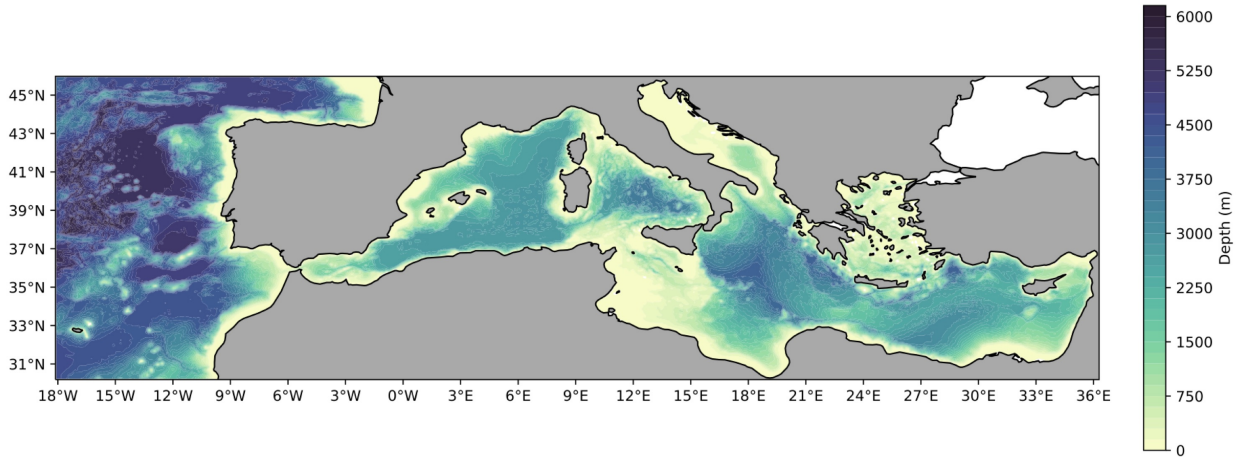

Figure 2.1: NEMO model domain of the Mediterranean Sea and Atlantic box, with model bathymetry in contours.

with an additional climatology from the Marmara Sea at the Dardanelles Strait boundary, used in conjunction with the global Copernicus analysis data. River forcing derived from monthly mean climatology of 39 rivers, selected on the basis of their large inflow, adds fresh water to the surface layer. Figure 2.1 shows a map of the model domain.

The model resolution is $\frac{1}{24}^{\circ}$, which is around 4km in the Mediterranean Sea, and 141 vertical z* levels, ranging from 2m close to the surface, to layers of 100m in the deepest ocean. The horizontal resolution is considered to be eddy-rich, as the Rossby radius of deformation is larger than the model resolution (around 3.8km) in many areas, but in some regions and seasons, the Rossby radius is much lower (Beuvier et al., 2012; Giordani et al., 2017), so the sub-mesoscale is not entirely resolved by the model.

Atmospheric forcing for NEMO comes from the European Centre for Medium Range Weather Forecasts (ECMWF) analysis at a six-hourly temporal resolution and $\frac{1}{8}^{\circ}$ (2015-2018) and $\frac{1}{10}^{\circ}$ (2019-2022) horizontal resolution, interpolated onto the model grid. Bulk formulae from Pettenuzzo et al. (2010) is used to transform the atmospheric data into momentum, water, and heat fluxes.

All NEMO experiments, except for the one without tides in Chapter 3, include the representation of eight tidal components (M2, S2, K1, O1, N2, Q1, K2, P1) achieved through

the representation of the tidal potential and the inclusion of tidal forcing from the lateral open boundary in the Atlantic Ocean derived by using TPXO9 data (Egbert and Erofeeva, 2002).

The model bathymetry is sourced from the GEBCO 30-second bathymetry, (GEBCO Bathymetric Compilation Group 2014, 2014), interpolated onto the model grid. Some modifications are made from this in some experiments: all tidal experiments have several modifications according to Agresti (2018), where grid points at the north-eastern boundary in the Bay of Biscay were closed (moved from sea to land) and points close to islands in the mid-Adriatic were modified for stability purposes. Further to this, in Section 2.3, the bathymetry in the Gibraltar Strait is modified at several grid points in order to reduce spurious vertical motion and to improve the representation of transport of mass through the strait. These experiments are detailed in Section 2.3, and the optimal modified bathymetry at the Gibraltar Strait is used again in Section 2.4 and Chapter 4.

Several vertical mixing parameterizations are available in NEMO v3.6, including a Richardson number-based parameterization from Pacanowski and Philander (1981), and a turbulent kinetic energy (TKE) scheme based on Gaspar et al. (1990) and Madec et al. (1998). The implementation of these schemes and their relevant parameterizations in NEMO is detailed further in Section 2.4. The parameterization from Pacanowski and Philander (1981) is used in all experiments in Chapter 3 and Section 2.3, and is tested against turbulent kinetic energy schemes with a variety of parameterization choices in Section 2.4. The best-performing TKE scheme is used again in Chapter 4.

The NEMO configuration in the experiments in this thesis uses a background vertical eddy viscosity of 1.2×10^{-6} m^{2}s^{-1}, a background vertical eddy diffusivity of 1.0×10^{-7} m^{2}s^{-1}, and a second-order centred time-stepping scheme with a timestep of 120 seconds for all experiments except for the "Model without tides" in Chapter 3, which uses a forward time-stepping scheme with a timestep of 240 seconds. Further details about the time-stepping schemes and the reasoning behind this choice is found in Chapter 3.

2.3 Gibraltar Strait bathymetry impacts on the Mediterranean Sea dynamics

2.3.1 Motivation

After analysing the vertical motion in a model configuration including tides (based on the MedFS operational system EAS6, Clementi et al. (2021)) described in Chapter 3 compared to the model configuration without tides (based on the MedFS operational system EAS5, Clementi et al. (2019)), it became clear that two grid points in the narrowest part of the Gibraltar Strait had extremely large values of vertical velocity in the tidal experiment when compared with the experiment without tides and the rest of the Mediterranean Sea. These values persist throughout the model run, and through the water column. Mean values of vertical velocity over the full analysis period (2017-2021), are larger here than anywhere else in the Mediterranean Sea, as can be seen in Figures 2.2 and 2.3. It was suggested that these large values could be due to internal tides over the steep and narrow topography in this region. However, the large values appear on only two adjacent grid points (one for upwelling and the other for downwelling), and the vertical mean vertical velocity is much larger here than anywhere else in the region: at the point in Figure 2.2, we can see mean values reaching 6×10^{-4} ms^{-1} at a single point, compared to a maximum of 1×10^{-4} ms^{-1} anywhere else in the region (Figure 2.2), over the entire 5-year period. Profiles of vertical velocities in these two grid points presented in Figure 2.3 clearly show large increased velocity between 200m and 700m when including tides. Therefore, we decided to reconfigure the model bathymetry in the region before the experiment of Chapter 4.

2.3.2 Bathymetry experiments

The model used to run these experiments is NEMO v3.6, based on the Copernicus Marine Service Mediterranean Forecasting system (MedFS) EAS6 (Clementi et al., 2021) implementation, a baroclinic forecasting model for the Mediterranean including tides. The experiments are also compared to a reference model configuration without tides based on

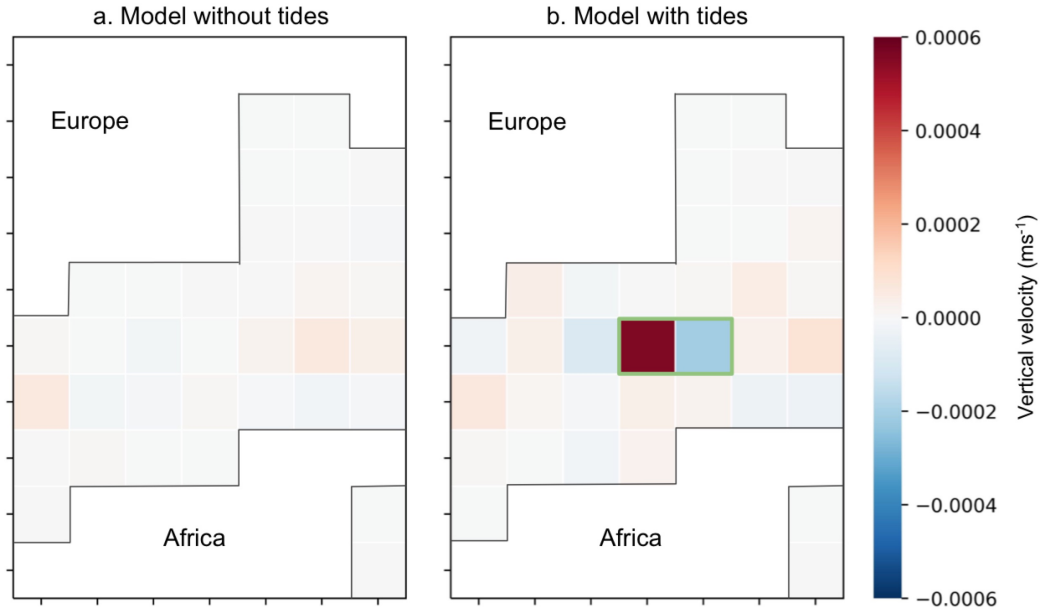

Figure 2.2: Vertically averaged vertical velocity in the Gibraltar Strait area (5.6-5.3°W) in winter (JFM) 2017-2021, for the model without tides (left) and with tides (right). Points encircled in green are the maximum and minimum values in the region.

a previous MedFS version, Clementi et al. (2019). Both of these configurations are the same as those used in Chapter 3 and are used as reference configurations in the following analysis.

The standard bathymetry in the model is the GEBCO 30-sec bathymetry (GEBCO Bathymetric Compilation Group 2014, 2014), bilinearly interpolated onto the model grid. For most of the Mediterranean basin and Atlantic box, this is the only step for bathymetry calculation. Some changes were made to the bathymetry in the initial tidal configuration (Chapter 3) to improve stability in the Bay of Biscay and on the Croatian coast, according to Agresti (2018). Bathymetry in the Gibraltar Strait region, both in the operational model and GEBCO, can be seen in Figure 2.4. This figure highlights the limited horizontal resolution in the model compared to what would be required to accurately represent the complex and steep topography in the Gibraltar Strait.

Therefore, we suggest that the high vertical velocity values in Figure 2.3 are caused by spurious internal mixing over a steep topography, so the experiments are configured with

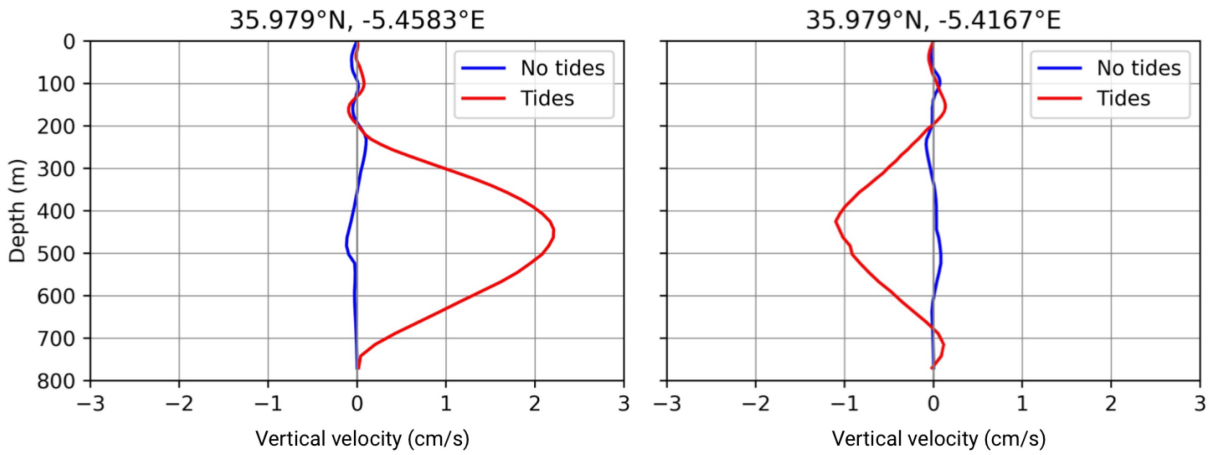

Figure 2.3: Vertical velocity profiles at points in the Gibraltar Strait: [35.979°N, 5.458°W] and [35.979°N, 5.417°W] (the two points encircled in green in Figure 2.2b), for the model with tides (red) and without tides (blue). Values are the mean of daily data for each gridpoint during the period 2017-2021.

the goal of creating a smoother slope in the region. The other major requirement was to ensure that no longitude in the Gibraltar Strait had fewer than four horizontal grid points representing the ocean. This involves artificially widening the strait at some longitudes, since the model has a horizontal resolution of 4km, and the Gibraltar Strait has a minimum width of 14km.

Four model runs are integrated for this work, each changing the bathymetry of the model with tides, and comparing the model outputs to the reference experiments with and without tides. The model can be run from 2015 up to the end of 2021. A two-year spin-up period is considered, so the initial run (results in Section 2.3.3) of Tests 1-4 for 2015-2017 are analysed for 2017 only. The longer run (Section 2.3.4) is from 2015-2021, meaning that results are analysed for the five-year period of 2017-2021. The first two tests attempt to create a realistic bathymetry configuration through manual edits to the model bathymetry, while Tests 3 and 4 move away from a realistic configuration and represent the Gibraltar Strait as a smoothed slope, with a minimum of two ocean grid points at the deepest level of each longitude, ensuring both zonal and meridional currents are non-zero at the bottom layer.

The changes were made at seven points in Test 1 and eight points in Test 2, with two points

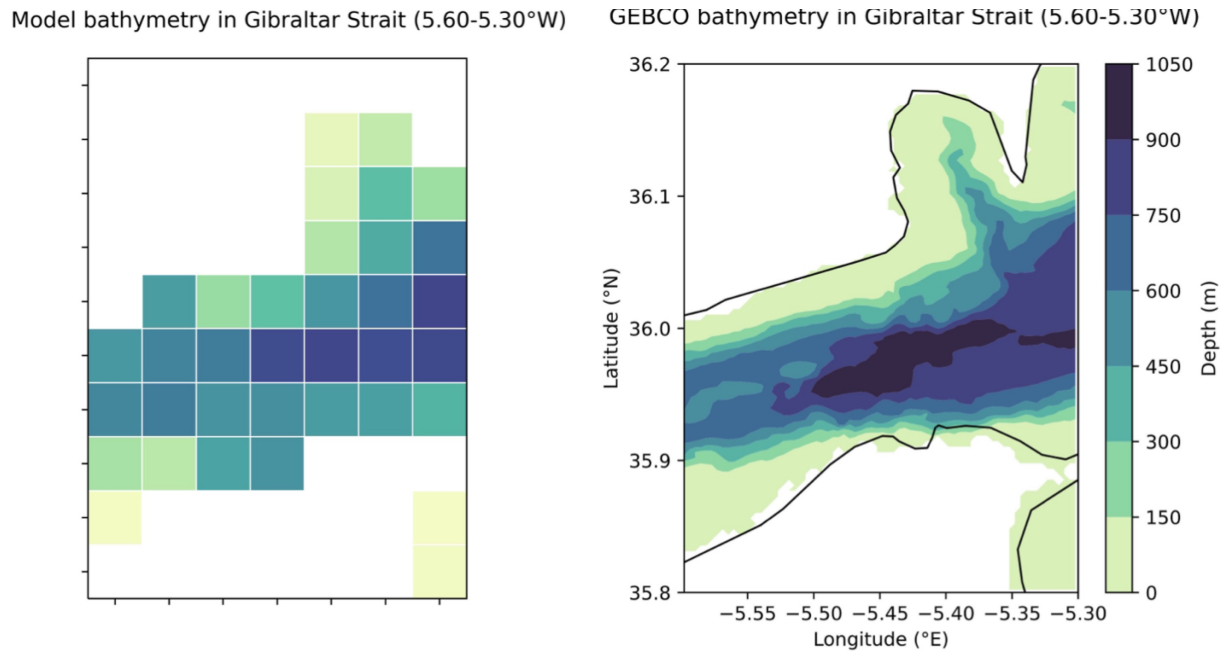

Figure 2.4: Operational model (left) and GEBCO (GEBCO Bathymetric Compilation Group 2014, 2014) bathymetry (right), in the Gibraltar Strait region (5.6-5.3°W).

changed between the two tests, as detailed in Table 2.2 and visualised in Figure 2.5. These edited points do not include the two points which have the largest values of vertical velocity ([35.979°N, 5.4583°W] and [35.979°N, 5.4167°W]) in the operational model, since these points appear to accurately represent the real depth at their locations, but instead, nearby points are modified to ensure that these points are no longer much deeper than the surrounding points in the model bathymetry. A different approach is used in Tests 3 and 4, where we prioritise a smoothed slope through the Gibraltar Strait, while maintaining accurate maximum depths at each longitude compared to GEBCO and EMODnet. This was prioritised over accuracy of the shape of the Strait in these tests, since two points in both the longitude and latitude directions are required to allow for both zonal and meridional flow at the bottom layer. Changes in these tests are also seen in Table 2.2 and Figure 2.5.

The effect of the vertical discretisation in NEMO due to z-coordinates and partial cells was checked, and changes between the bathymetry chosen in Table 2.2 and the eventual model bathymetry are on the order of a few centimetres in the deeper Mediterranean Sea, and less than 1cm in coastal and shallow regions.

Longitude (°W)	Latitude (°N)	Model (m)	Test 1 (m)	Test 2 (m)	Test 3 (m)	Test 4 (m)
5.5833	35.9375	555.654	-	-	550.000	550.000
5.5833	35.9792	487.053	-	-	550.000	550.000
5.5833	36.0208	0.000	-	-	100.000	100.000
5.5417	35.9375	596.182	-	-	600.000	600.000
5.5417	35.9792	567.769	-	-	600.000	600.000
5.5417	36.0208	461.584	200.000	200.000	200.000	200.000
5.5000	35.8958	439.899	250.000	250.000	250.000	250.000
5.5000	35.9375	506.708	750.000	650.000	700.000	700.000
5.5000	35.9792	597.337	-	-	700.000	700.000
5.4583	35.8958	500.637	350.000	350.000	350.000	350.000
5.4583	35.9375	524.761	800.000	800.000	800.000	800.000
5.4583	35.9792	778.806	-	-	800.000	800.000
5.4167	35.8958	0.000	100.000	100.000	100.000	100.000
5.4167	35.9375	470.443	700.000	700.000	800.000	700.000
5.4167	35.9792	800.452	-	-	800.000	900.000
5.4167	36.0208	492.579	-	625.000	800.000	900.000
5.3750	35.9792	772.999	-	-	800.000	900.000
5.3750	36.0208	637.744	-	-	800.000	900.000
5.3333	35.9792	790.669	-	-	800.000	900.000
5.3333	36.0208	806.997	-	-	800.000	900.000

Table 2.2: Bathymetry changes made in the four experiments. Dashes represent points which were unchanged from the model bathymetry.

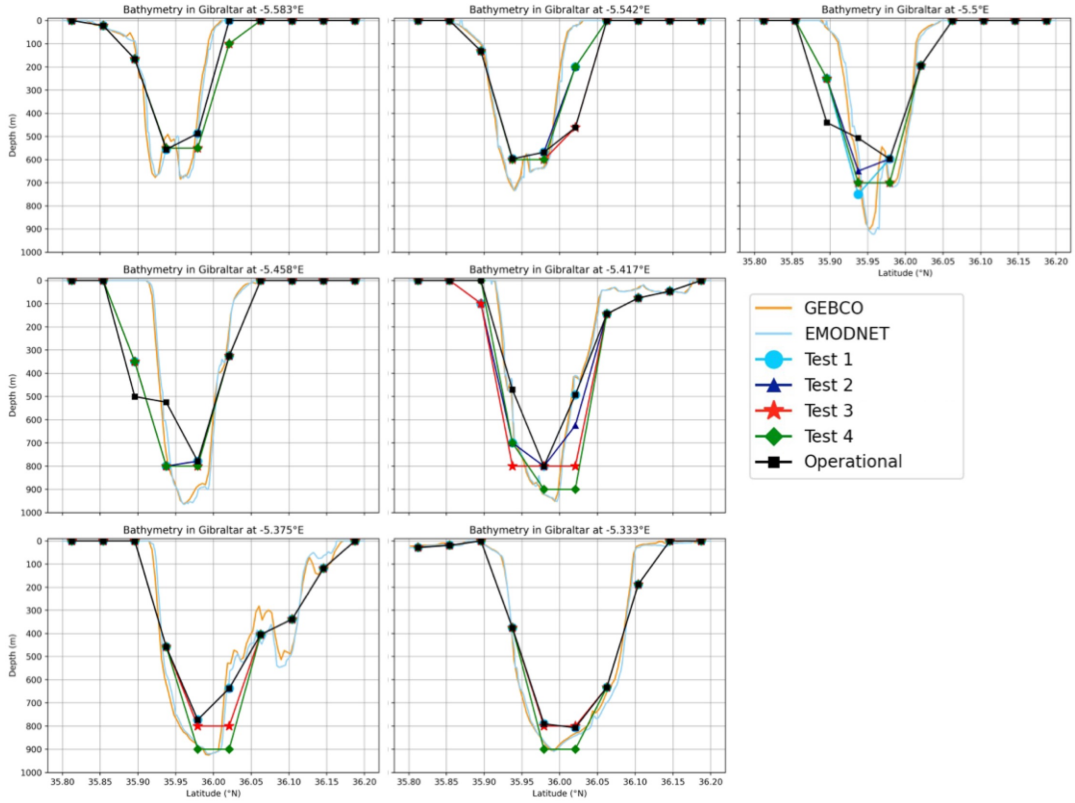

Figure 2.5: Bathymetry changes made in the four experiments at each model longitudes, and measured bathymetry: GEBCO in orange and EMODnet (EMODnet Bathymetry Consortium, 2020) in light blue, reference model (black squares), Test 1 (light blue circles), Test 2 (dark blue triangles), Test 3 (red stars), and Test 4 (green diamonds).

An initial three-year integration of the model (2015-2017) is run for all tests, and the tests are compared to the reference model with and without tides, paying particular attention to the region in the Gibraltar Strait where the large values of vertical velocity first occurred.

After this initial analysis, Tests 2 and 3 were carried forward, and were integrated up until the end of 2021. Analysis of this longer run focused more on the implications of the changes on the Gibraltar Strait mass transport.

2.3.3 Preliminary experiments (2015-2017)

The first tests to determine whether the bathymetry changes had improved the representation of vertical velocity in the Gibraltar Strait focused on checks in individual grid points

in the region between 3.6-3.3°W. Figure 2.6 shows the vertical velocity in the Gibraltar Strait region for the model without tides, the reference model, and the four experiments in winter (January-March) 2017. It was found that in Test 1, the maximum vertical velocity was only slightly reduced, and moved one point to the south-west of its original position. Tests 2 and 3 still have some large values for vertical velocity, but this time the effect is spread out over several points. Test 3's vertical velocity maximum value is at the coast, which is also more realistic than maximum upwelling occurring in the middle of the Strait. Test 4 performs less well than Test 3, with larger maximum and minimum values of vertical velocity.

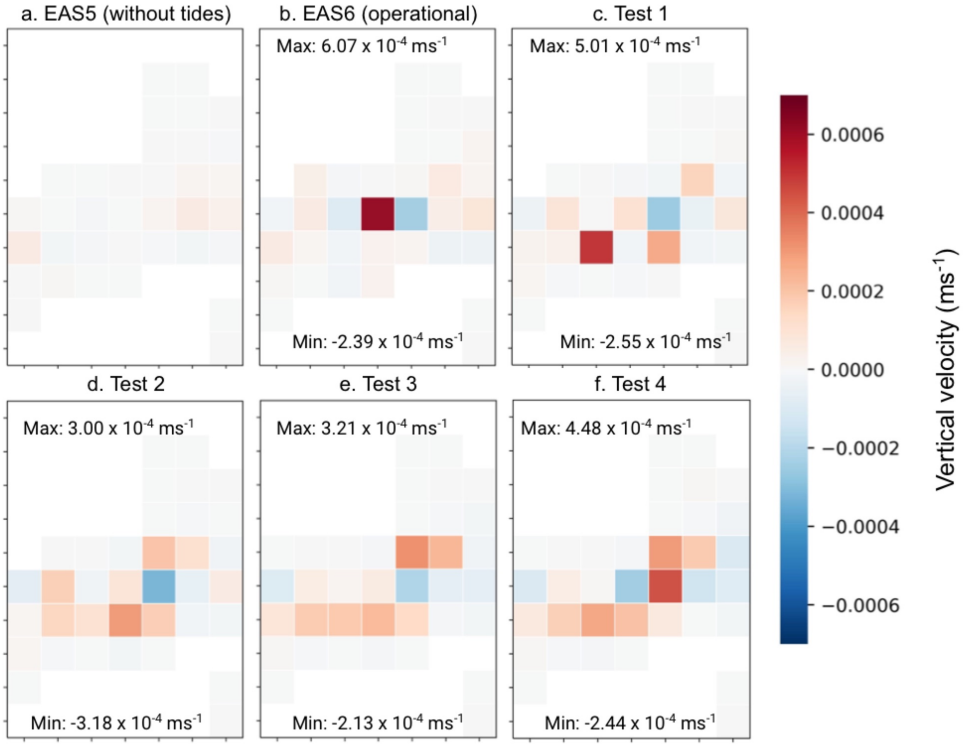

Figure 2.6: Vertical mean vertical velocity in the Gibraltar Strait in winter (January-March) 2017, for the reference model without tides (a), reference model with tides (b), and the four bathymetry tests (c-f)

In Figure 2.7, the profiles of vertical velocity evaluated at individual grid points in the centre of the Strait, including all points with large values in Figure 2.6 are shown, further detailing the region. As in the reference model with tides, the largest vertical velocity values of the tests occur over many vertical levels, not at any single point. The large

maximum points in Tests 1 and 4 are visible at [35.979°N, -5.4167°E] and [35.938°N, -5.5000°E] respectively, and it can be seen that the maximum velocities in Tests 2 and 3 are much less extreme.

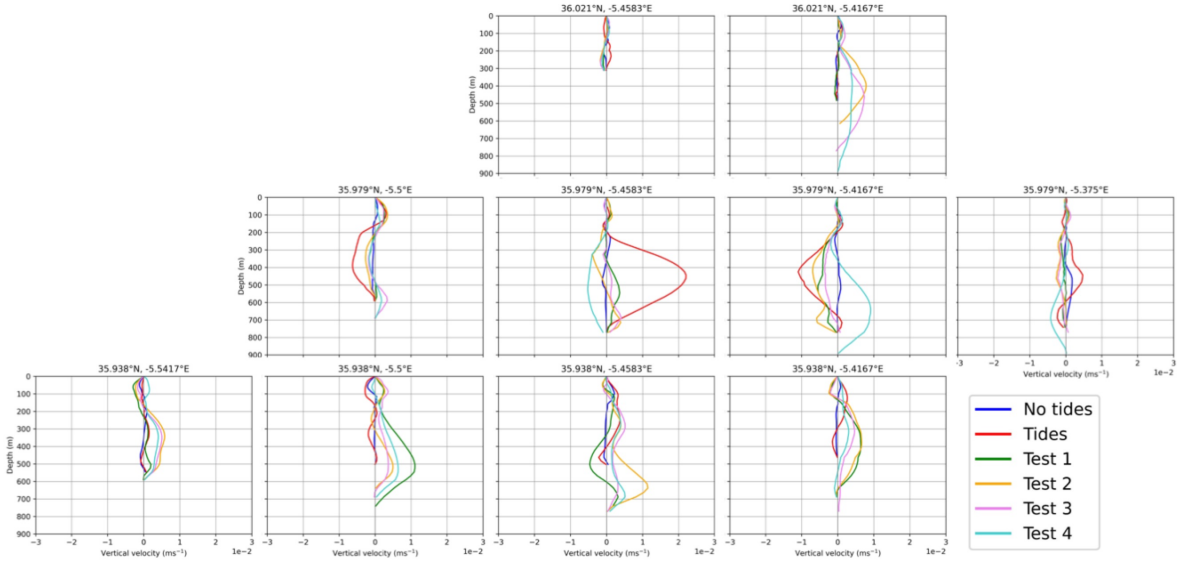

Figure 2.7: Profiles of vertical velocity for individual points in the centre of the Gibraltar Strait, 2017. Reference model without tides in blue, reference model with tides in red, Test 1 in green, Test 2 in orange, Test 3 in pink, and Test 4 in light blue.

Since Test 1 has maximum vertical velocity values of similar magnitude to the reference model with tides (Figure 2.7c), and Test 4's maximum is also large, it is concluded that these bathymetry configurations do not merit further analysis as they do not solve the initial problem, but rather relocate the same problem to a different point. Tests 2 and 3, however, appear more promising after this initial analysis of individual grid points in the Gibraltar Strait, and are therefore carried forward for a longer model run up to the end of 2021. This longer run allows for analysis of the water mass transport at Gibraltar.

2.3.4 Extended experiments (2015-2021)

Water mass transport at the Gibraltar Strait is numerically calculated from horizontal currents, and values are shown for the reference experiments with and without tides and Tests

Experiment	Inflow	Outflow	Net transport
Reference model without tides	**0.84778** Sv	**-0.80311** Sv	**0.044675** Sv
Reference model with tides	0.88221 Sv	-0.83875 Sv	**0.043451** Sv
Test 2	**0.85424** Sv	**-0.81071** Sv	**0.043524** Sv
Test 3	**0.83700** Sv	**-0.79383** Sv	**0.043164** Sv
Observations: Soto-Navarro et al. (2010)	0.81±0.06 Sv	-0.78±0.05 Sv	0.038±0.007 Sv

Table 2.3: Mean transport at Gibraltar at 5.48°W in Sverdrups ($10^6 m^3 s^{-1}$) from 2017-2021, for the model without tides, the reference model with tides, and bathymetry Tests 2 and 3, compared to observational results from Soto-Navarro et al. (2010) and model results from Sanchez-Roman et al. (2018) in the Tarifa Narrows (∼5.60°W). Values in **bold** are within the observational errors of Soto-Navarro et al. (2010).

2 and 3 in Table 2.3. The net transport is only slightly changed between the experiments, but transport in each direction is reduced with the changed bathymetry, particularly in Test 3, and is closer to the values for the model without tides and the observations (Soto-Navarro et al., 2010). All values of transport for Tests 2 and 3 are within the error range of the observations, whereas in the reference model with tides, only the net value is within this range. The method for calculating the mass transport is described in full in Appendix B.2.

2.3.5 Summary

The model bathymetry was modified in the Gibraltar Strait region (6.0°W-5.3°W), with the objective of improving the representation of the vertical motion and removing spurious extreme values on specific profiles. The transport of water through the Gibraltar Strait is affected by changing the bathymetry. Compared to the reference model with tides, transport in and out of the Mediterranean Sea is reduced by 0.05 Sv and 0.04 Sv respectively in Test 3, while the net transport is not significantly affected. These changes bring the model transport closer to the observations by Soto-Navarro et al. (2010).

Since the bathymetry changes implemented in Test 3 of this experiment were generally successful, both in reducing the magnitude of spurious vertical velocity values at single

gridpoints, and also in its representation of mass transport in the Gibraltar Strait, this configuration of the bathymetry will be used for the following sensitivity experiments on the vertical mixing parameterization (Section 2.4), and the internal tides experiments in Chapter 4. There is also the potential for future work to further refine the bathymetry in the Gibraltar Strait region, through experiments that use filters for bathymetry smoothing, such as through a Gaussian or a Shapiro filter (Shapiro, 1970). However, it was found in Misra et al. (2016), in the Gulf of Mexico and the Caribbean Sea, that smoothed and coarse bathymetry can lead to worsened results for sea surface temperature and currents. A more computationally expensive and complex, but potentially better-performing, solution would be to use a two-way nested grid refinement at a very high resolution to represent the Gibraltar Strait, as in Sannino et al. (2009). Alternatively, a non-uniform grid with gradually higher resolution in the Strait (and potentially other narrow or steep regions) as in Sannino et al. (2015) could also achieve improved results. Any higher resolution grid should be at sub-kilometre horizontal scale in the Gibraltar Strait in order to have good accuracy in the region.

2.4 Sensitivity experiments on vertical mixing schemes in a numerical model of the Mediterranean Sea

2.4.1 Motivation

Vertical mixing processes in the ocean occur at subgrid scales in most hydrodynamic ocean models, including the implementation of NEMO used in this thesis, and therefore are unresolved and must be parameterized in order to ensure that models mix the ocean accurately. These processes are necessary to maintain the overturning circulation of the global ocean (Gent, 2018), and combine effects of several phenomena. The sources of this mixing, such as tides, wind forcing, and the flow of waves over topography are better understood than the sinks, which include internal wave energy dissipation, wave breaking, and nonlinear wave-wave interactions (Fox-Kemper et al., 2019). One particular challenge is low-mode internal waves which propagate away from their generation sites, since these waves are

commonly unresolved by climate models, and their sites of dissipation and propagation are relatively unknown in many parts of the global ocean (Melet et al., 2013).

Using the Richardson number to estimate diapycnal diffusivity is one method of parameterizing this vertical mixing (Pacanowski and Philander, 1981), and another commonly chosen parameterization is the k-profile parameterization (KPP) (Large et al., 1994). Vertical mixing parameterizations with more sophisticated second-order physics have been developed and are frequently used in numerical models, such as turbulent kinetic energy (TKE) closure schemes, e.g. Gaspar et al. (1990), and generic length scale (GLS) closure schemes (Umlauf and Burchard, 2005). TKE schemes provide the opportunity to include further parameterizations of subgrid scale mixing processes, such as Langmuir cells (Gutjahr et al., 2021).

Some works have compared several vertical mixing parameterizations in a global ocean model, such as Gutjahr et al. (2021), which used four schemes including the Richardson number parameterization, KPP, and two versions of TKE. This work demonstrated the advantages of using TKE, which includes an ability to produce a more heterogeneous pattern of vertical diffusivity, leading to better outcomes for the general circulation. The potential need for regional refinement of vertical mixing schemes was also highlighted in this work, since some schemes are not able to account for regional phenomena in the ocean with a fixed set of parameters, and more customisation is necessary.

In another suite of experiments using a global model by Li et al. (2019), the addition of parameterizations of Langmuir cells to a TKE scheme caused changes in the mixed layer depth, depending on forcing as well as regional and seasonal variation, when the model was coupled with waves. Results are highly sensitive to model configuration and the model used, and this contributes to outcomes in which the improved model physics of second-order schemes doesn't always lead to improved accuracy of a model output. This is the case in Halpern et al. (1995) in the tropical Pacific Ocean, where the Richardson number parameterization from Pacanowski and Philander (1981) performed better than a TKE scheme by Mellor and Yamada (1982). However, Tirodkar et al. (2022) found that a second-order scheme improved results in the Bay of Bengal. It is clear that regional dynamics and variations between models affect the success of vertical mixing schemes, and

that no scheme that has been used in the past is universally better-performing than others.

The coastal nature of the Mediterranean Sea adds further complexities to the problem of vertical mixing parameterizations, as coastal regions are challenging for the comparison of these schemes (Durski et al., 2004). In Durski et al. (2004), an idealised model of a coast was used to compare KPP with a TKE closure scheme, it was found that despite the improved physics of the TKE scheme, neither experiment was found to be superior to the other. In the Mediterranean Sea, Fernández et al. (2006) compared KPP and a second-order closure model and found that the second-order model achieved similar results in temperature profiles when compared to observations from Argo floats, and that the model was more sensitive to factors such as atmospheric forcing.

In these sensitivity experiments, several variations of the TKE closure scheme (Gaspar et al., 1990) available in the NEMO hydrodynamic ocean model (Madec et al., 2019) were compared to the Richardson number-based parameterization (Pacanowski and Philander, 1981) in the Mediterranean Sea. Section 2.4.2 describes the schemes and parameterizations available for use in NEMO, sections 2.4.3, 2.4.4, and 2.4.5 provide the model configuration and list the experiments carried out, sections 2.4.6 and 2.4.7 contain the results, and conclusions are presented in section 2.4.8.

2.4.2 Vertical mixing parameterizations and schemes tested

A suite of sensitivity experiments using different parameter selections within the TKE scheme are carried out and compared to the control experiment, which uses the Richardson number-dependent formulation. The following subsection details these schemes and parameters.

Richardson number-dependent formulation The control experiment is the experiment with tides described in Chapter 3, which uses a Richardson number-based vertical mixing parameterization based on Pacanowski and Philander (1981) where the Richardson number, Ri, is:

$$Ri = \frac{N^2}{\frac{\partial \bar{v}}{\partial z}^2} \tag{2.1}$$

where N^2 is the Brunt-Väisälä frequency, and $\frac{\partial \bar{v}}{\partial z}^2$ is the horizontal component of the vertical shear. The scheme then calculates vertical viscosity and diffusivity according to the Richardson number:

$$A^{vT} = \frac{A^{vT}_{ric}}{(1 + aRi)^n} + A^{vT}_b \tag{2.2}$$

$$A^{vm} = \frac{A^{vT}}{(1 + aRi)} + A^{vm}_b \tag{2.3}$$

where A^{vT} and A^{vm} are the vertical eddy viscosity and diffusivity respectively, and A^{vT}_{ric}, a, and n are adjustable parameters. In this experiment, these parameters are set to 100×10^{-4} m^2s^{-1}, 5, and 2 respectively. The background vertical eddy viscosity is $A^{vT}_b = 10^{-7}$ m^2s^{-1} and the background vertical eddy diffusivity value is $A^{vm}_b = 1.2 \times 10^{-6}$ m^2s^{-1}.

Turbulent kinetic energy (TKE) closure scheme The scheme tested in the other experiments is based on a turbulent kinetic energy closure model from Gaspar et al. (1990), with further refinement by Madec et al. (1998). This parameterization sets the time evolution of turbulent kinetic energy $\bar{e}$, as:

$$\frac{\partial \bar{e}}{\partial t} = \frac{K_m}{e_3^2}\left[\left(\frac{\partial u}{\partial k}\right)^2 + \left(\frac{\partial v}{\partial k}\right)^2\right] - K_\rho N^2 + \frac{1}{e_3}\frac{\partial}{\partial k}\left[\frac{A_{vm}}{e_3}\frac{\partial \bar{e}}{\partial k}\right] - C_\epsilon \frac{\bar{e}^{\frac{3}{2}}}{l_\epsilon} \tag{2.4}$$

$$K_m = C_k l_k \sqrt{\bar{e}} \tag{2.5}$$

$$K_\rho = \frac{A_{vm}}{P_{rt}} \tag{2.6}$$

where N is the Brunt-Väisälä frequency, C_ϵ is the coefficient of the Kolmogoroff dissipation $\sqrt{2}/2 \approx 0.7$, l_ϵ is the dissipation length scale, C_k is the vertical eddy coefficient which is 0.1 in these experiments, l_k is the mixing length scale, and P_{rt} is the Prandtl number, which is set to 1 in these experiments. The experiments conducted in this work all use the first

order approximated form of the mixing length scales from Blanke and Delécluse (1993): $l_\epsilon = l_k = \sqrt{2\overline{e}}/N$.

Enhanced vertical diffusion An additional parameter commonly used alongside the Richardson number parameterization is that of enhanced vertical diffusion (EVD). This is implemented where layers are unstable ($N^2 \leq -1 \times 10^{-12}$ s^{-2}), and imposes a vertical diffusivity coefficient of 10 m^{2}s^{-1}. This value is much larger than more realistic diffusivity values which are rarely above 1 m^{2}s^{-1}, but inserts diffusivity where the Richardson number parameterization alone doesn't mix the upper layers enough, such as in the Gibraltar Strait and regions of deep water formation. The necessity of this parameter is tested in the experiments in this work, with the goal of finding a balance between avoiding excessive unphysical artificial mixing while maintaining sufficient mixing in the regions where it is needed. Excessive EVD could reduce the accuracy in regions of other important phenomena such as internal waves, which require high stratification in order to propagate, and eddy-rich fields, such as the south-west Mediterranean Sea.

Langmuir cell parameterization Another parameterization that is available in NEMO when using TKE is that of the Langmuir cells, which are a source of mixing close to the ocean surface. Langmuir cells are formed due to the interaction between surface winds and Stokes drift, and contribute to the establishment of the pycnocline and mixed layer. More detailed descriptions are available in e.g. Craik and Leibovich (1976) and Teixeira (2019).

The parameterization adopted in NEMO, P_{LC}, is added as an extra source term of TKE to Equation 2.4 following Axell (2002), and is defined as:

$$P_{LC}(z) = \frac{w_{LC}^3(z)}{H_{LC}} \tag{2.7}$$

where w_{LC} is the vertical velocity of the Langmuir cell and H_{LC} is the Langmuir cell depth. This term is used as an extra source term of TKE when the parameterization is used. Since there is no wave-current coupling in the experiments in this work, w_{LC} is calculated according to the depth and set to zero at the surface, as follows:

$$w_{LC} = \begin{cases} c_{LC} u_s \sin \frac{-\pi z}{H_{LC}} & \text{if } z \leq H_{LC} \\ 0 & \text{otherwise} \end{cases} \tag{2.8}$$

where $u_s = 0.377|\tau|^{1/2}$ is the Stokes drift, $|\tau|$ is the surface wind stress and c_{LC} is set to 0.15 in these experiments, according to the work of Delrosso (2020). H_{LC} is calculated as:

$$-\int_{-H_{LC}}^{0} N^2 z dz = \frac{1}{2} u_s^2 \tag{2.9}$$

This is the depth that a water parcel can reach by converting its kinetic energy from Stokes drift into potential energy.

The Langmuir cell parameterization was tested, as it can be a more physically realistic alternative to EVD, since its mixing is based on physical parameters rather than an arbitrary additional mixing. However, it is disadvantaged by the lack of wave-current coupling in this configuration, and this parameterization may not mix the upper layers sufficiently, at least in some regions, when compared to EVD, which adds large amounts of mixing to unstable regions.

Mixing below the mixed layer This parameterization from Rodgers et al. (2014) is used in one of the experiments in this work, and has the potential to rectify mixed layer depths that are too shallow in summer and in windy weather. The boundary condition is modified to:

$$S = f_r e_s e^{z/h_\tau} \tag{2.10}$$

where S is the extra TKE input into the ocean, f_r is the portion of the surface TKE which penetrates into the ocean, e_s is the surface boundary condition of TKE, z is the depth, and h_τ is the parameter that controls the length scale of the penetration, set to 10m.

Non-penetrative convection This parameterization, available in NEMO, mixes the statically unstable portion of the water column downwards instantaneously, until the density

matches that of the layer below. At each timestep, this continues iteratively through each layer until stability is established. This convection method has been shown to be useful in representing the Western Mediterranean deep water formation (Madec et al., 1991).

2.4.3 Model configuration

The model used for these experiments is NEMO v3.6, following the implementation of the Mediterranean Sea forecasting system operational in the framework of the Copernicus Marine Service (Coppini et al., 2023; Clementi et al., 2021). The configuration of NEMO for these experiments is similar to the tidal model described in Section 2.1 and used in Chapter 3, with one key difference: the bathymetry used in the Gibraltar Strait region is that of the most successful experiment (Test 3) described in Section 2.3. The other change from these experiments is the vertical mixing parameterizations used, which are described in the following sections.

2.4.4 TKE experiments

Eight experiments were performed with a variety of mixing parameters changed. These parameters and their values in each experiment are detailed in Table 2.4. The eight experiments were initially analysed over one year (2017), after a two-year spin-up period of 2015-2016. These experiments were compared to the Pacanowski and Philander (1981) parameterization used in Chapter 3, with the modified bathymetry from Section 2.3. The most successful of these experiments are then extended for a further two years to give a longer analysis period of 2017-2019.

Several parameters are tested, namely the enhanced vertical diffusion (EVD) value, the switching on and off of the Langmuir cell parameterization, and tests of non-penetrative convection and additional TKE below the mixed layer. EVD is selected because it was necessary to maintain mixing in the Richardson number scheme, but is not a physical value of diffusivity. Switching EVD off as well as reducing its maximum value are tested. The Langmuir cell parameterization is tested, since this mixes the upper ocean based on

Experiment	Enhanced vertical diffusion	Langmuir cell parameterization	Non-penetrative convection	Additional TKE below mixed layer
TKE1	10 ms^{-2}	True	False	0
TKE2	False	True	False	0
TKE3	10 ms^{-2}	False	False	0
TKE4	False	False	False	0
TKE5	0.1 ms^{-2}	True	False	0
TKE6	1.0 ms^{-2}	True	False	0
TKE7	False	True	True	0
TKE8	10 ms^{-2}	True	False	1

Table 2.4: Experiments carried out in this work and the TKE parameters changed for each experiment. All results are discussed in section 2.4.6, while experiments in **bold** were extended to 2019, and are discussed further in section 2.4.7.

more realistic physics than EVD. However, without a wave-current coupled model, the Langmuir cell parameterization estimates the vertical velocity of the Langmuir cell based on wind stress (see equations 2.7-2.9), which may limit its success compared to when the parameterization is used in an ocean model coupled with waves.

Some parameters described above are not selected for testing, due to their recent optimisation through similar experiments with previous versions of the modelling system used in this work. Delrosso (2020) tested some TKE parameters on a previous version of the Clementi et al. (2021) system: the input of TKE at the surface due to surface wave breaking, and the value of c_{LC} from equation 2.8. Their best-performing values, 3.75 and 0.15 respectively for the two parameters, were used for all experiments in this work.

2.4.5 Observations and analysis

A key assessment of the success of each experiment was through validation of results compared to in-situ observations. Data from Argo observational floats (Argo, 2022) were used to validate model outputs in this work, using model outputs which are co-located in space

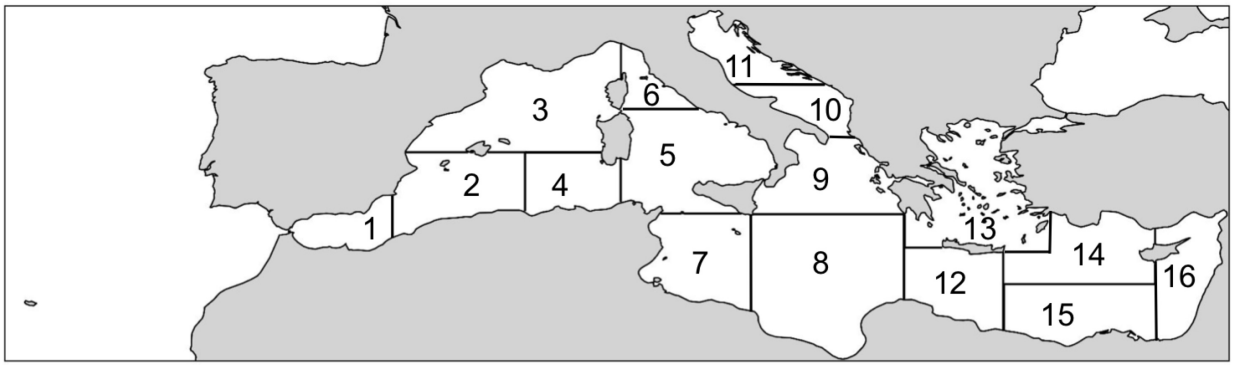

Figure 2.8: Map of sixteen analysis regions used in this work: 1. Alboran Sea, 2. South-west Mediterranean (western part), 3. North-west Mediterranean, 4. South-west Mediterranean (eastern part), 5. Tyrrhenian Sea (southern part), 6. Tyrrhenian Sea (northern part), 7. Ionian Sea (western part), 8. Ionian Sea (south-eastern part), 9. Ionian Sea (north-eastern part), 10. Adriatic Sea (southern part), 11. Adriatic Sea (northern part), 12. Levantine Sea (western part), 13. Aegean Sea, 14. Levantine Sea (central-northern part), 15. Levantine Sea (central-southern part), 16. Levantine Sea (eastern part).

and time with the observations. The number of observations used in each layer and region in this work can be found in Appendix A.

Argo floats typically measure temperature and salinity in the ocean from the surface down to mid-levels (2km), moving vertically by adjustments to the float's weight and horizontally with currents. Argo floats are widespread in the global ocean and are advantageous compared to satellite measurements alone due to their ability to measure below the surface. The accuracy of floats is 0.002°C for temperature and 0.01 PSU for salinity, according to Wong et al. (2020). The coverage of Argo floats is increasing year-by-year, but is not yet spatially complete, meaning that there are not observations available for all of the analysed regions during each analysed year or season. Validation is completed over the Mediterranean basin in its entirety and are also divided into sixteen regions to identify any regional biases, which are shown in Figure 2.8.

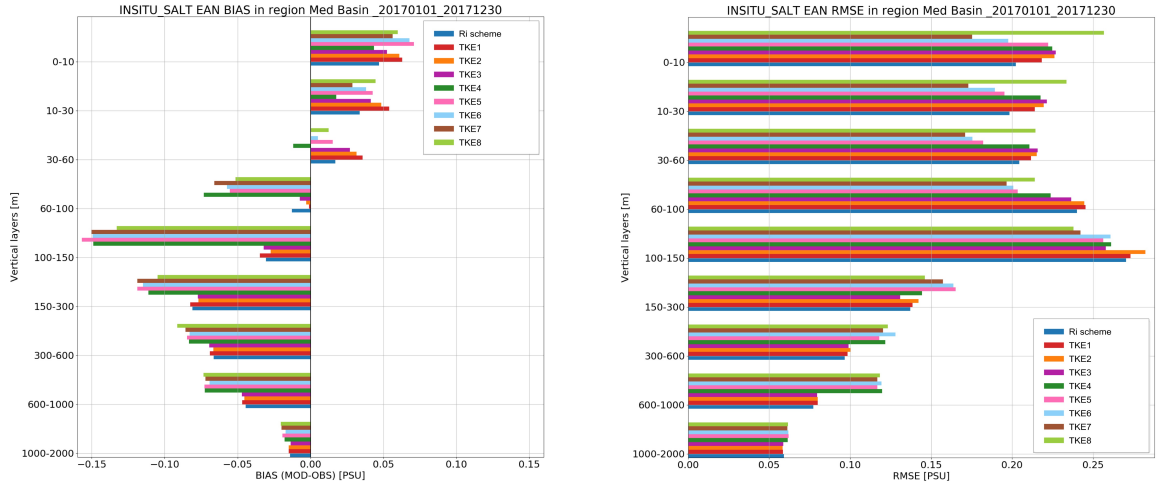

Figure 2.9: Salinity bias (left) and RMSE (right) for the Mediterranean Sea during 2017, for the suite of eight TKE experiments and the Richardson number reference run. Bias and RMSE are calculated against observations from Argo floats.

2.4.6 One-year experiments

Temperature and salinity RMSEs and biases over the entire Mediterranean Sea provide an overview of the success of each experiment. Figure 2.9 shows the bias and RMSE for salinity, where the model has its highest RMSEs in the subsurface between 60-150m for most experiments. Some experiments have much higher biases and RMSEs throughout the depths, while others have more mixed results. TKE8 performs particularly poorly in the upper layers in salinity RMSE, while TKE1, TKE2, and TKE3 have RMSEs closer to that of the Richardson number parameterization. The Richardson number-based parameterization generally performs well at all depths.

For temperature, Figure 2.10 shows that TKE4, TKE5, and TKE7 have considerably higher RMSEs than the other experiments in the upper and intermediate layers. The poor performance of these experiments demonstrates the importance of using enhanced vertical diffusion in a TKE scheme, since all of these experiments have either low or no EVD.

Subsurface depths of 60-150m are identified as the levels with the largest RMSEs in the Richardson number model, and therefore have the most room for improvement on the

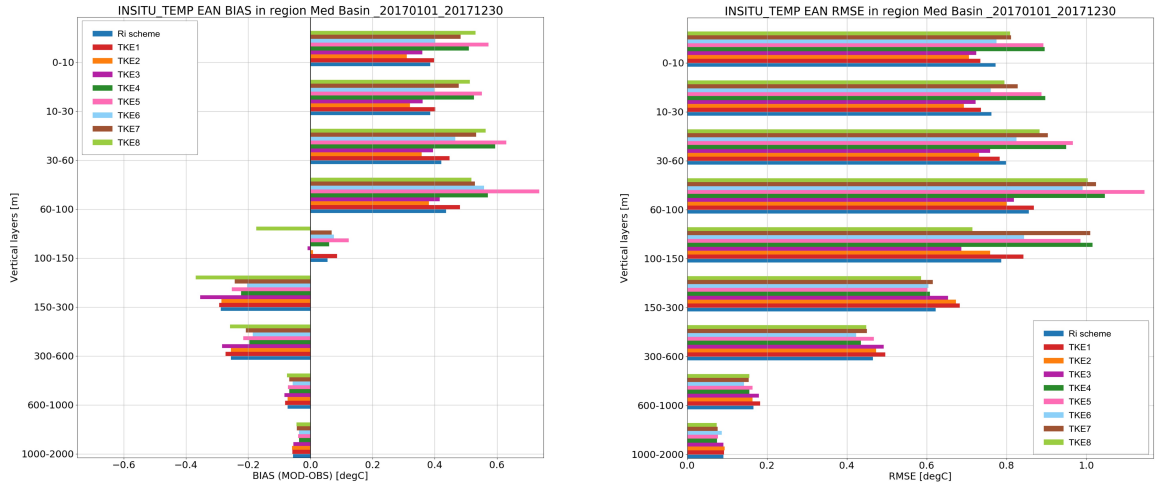

Figure 2.10: Temperature bias (left) and RMSE (right) for the Mediterranean Sea during 2017, for the suite of eight TKE experiments and the Richardson number reference run. Bias and RMSE are calculated against observations from Argo floats.

results. The RMSEs for these levels are analysed in the sixteen regions of the Mediterranean Sea from Figure 2.8, as shown in Figures 2.11 and 2.12. The RMSE of salinity is below 0.2 PSU in most regions and experiments in all three layers, with some notable exceptions. Region 4, the eastern part of the southwest Mediterranean, has the highest RMSE in the control experiment and TKE1-3. However, TKE5-7 have RMSEs above 0.2 PSU in many regions, especially in the western Mediterranean, demonstrating that these experiments are likely incorrectly mixing the incoming Atlantic water. Figure 2.13 shows the bias at each depth for each experiment in regions 2 and 4, the two regions of the south-west Mediterranean, where TKE1-3, as well as the Richardson number parameterization, have a positive salinity bias, while TKE5-7 have a negative salinity bias at 60-150m, meaning that the relatively fresh upper layer is not mixed enough with the more saline intermediate layers in TKE5-7. The large positive bias in TKE1-3 is limited to Region 4, whereas the negative bias of TKE5-7 occurs across both regions.

For temperature, shown in Figures 2.14 and 2.15, unlike in salinity, we see larger RMSEs across many regions and experiments, particularly at 60-100m where many experiments have RMSEs of more than 1°C in several regions, while TKE4-8 all have at least one region

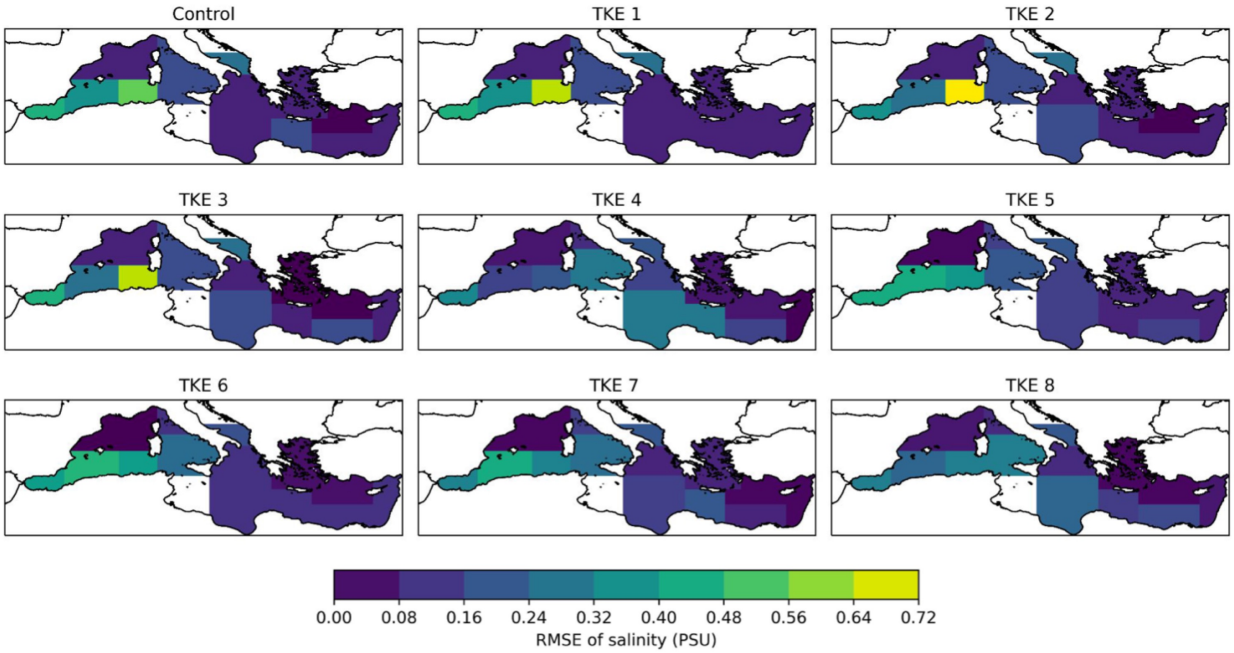

Figure 2.11: RMSEs of salinity by region (see Figure 2.8) at 60-100m in 2017, for the eight TKE experiments and the Richardson number scheme (Control).

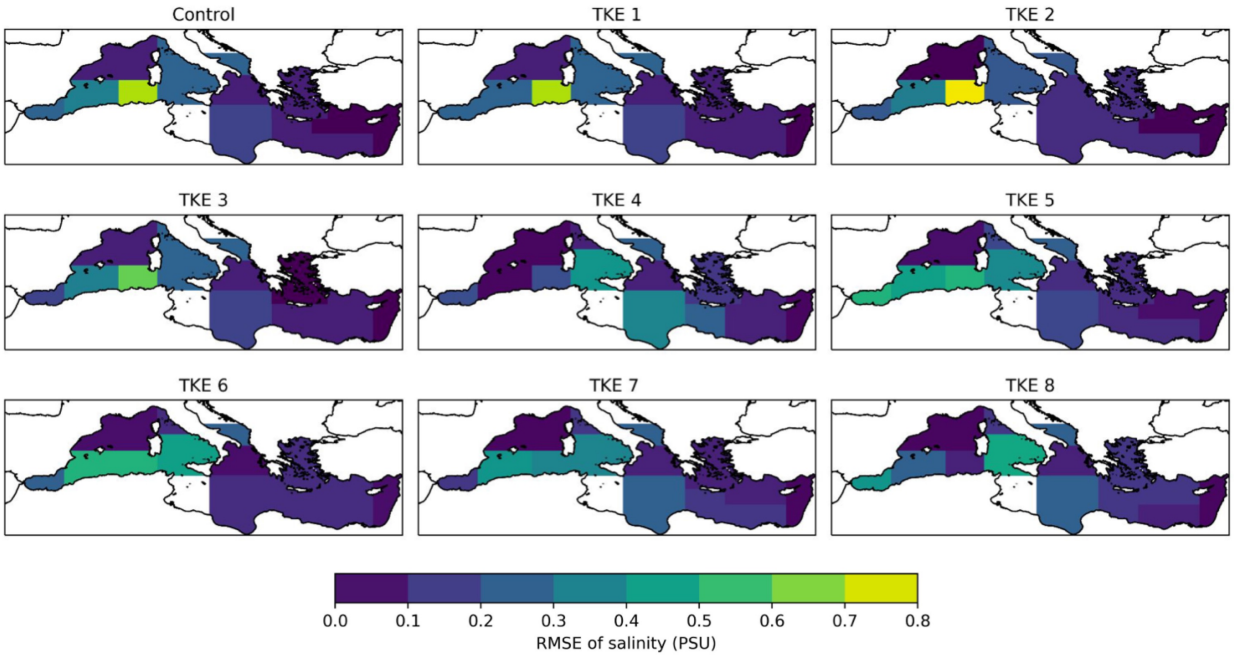

Figure 2.12: RMSEs of salinity by region (see Figure 2.8) at 100-150m in 2017, for the eight TKE experiments and the Richardson number reference run (Control).

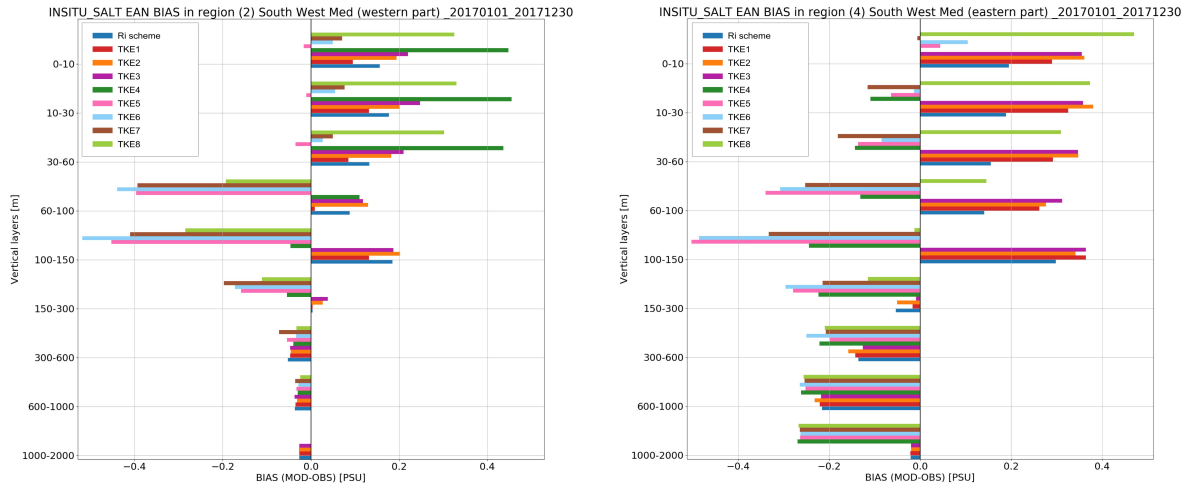

Figure 2.13: Salinity bias for Region 2 (left) and Region 4 (right) for the Mediterranean Sea during 2017, for the suite of eight TKE experiments and the Richardson number reference run.

where the RMSE is above 1.4°C at this depth. The largest RMSEs for temperature do not clearly originate directly from the incoming Atlantic water, but are spread across several regions, most notably the Tyrrhenian Sea at 60-100m and the southern Ionian and Levantine seas at 100-150m. We can see from Figure 2.10 that at 60-100m there is a warm bias in all experiments, but the warm bias is greater in TKE4-8 than in TKE1-3. This, as with the salinity bias, shows that the experiments with a larger warm bias may be underestimating the mixing between the warmer upper layers and cooler intermediate layers.

Considering both temperature and salinity, their relative biases and RMSEs across all depths and regions, particularly the key depths where the RMSE is highest, it appears that TKE1-3 have the most potential for obtaining results that are competitive with the Richardson number parameterization. These experiments were therefore extended to 2019, and again compared to the Richardson number parameterization, and observations from Argo floats.

2.4.7 Three-year experiments

Section 2.4.6 identified TKE1, TKE2, and TKE3 as the most successful of the suite of eight experiments, in terms of their success in representing temperature and salinity in the sub-

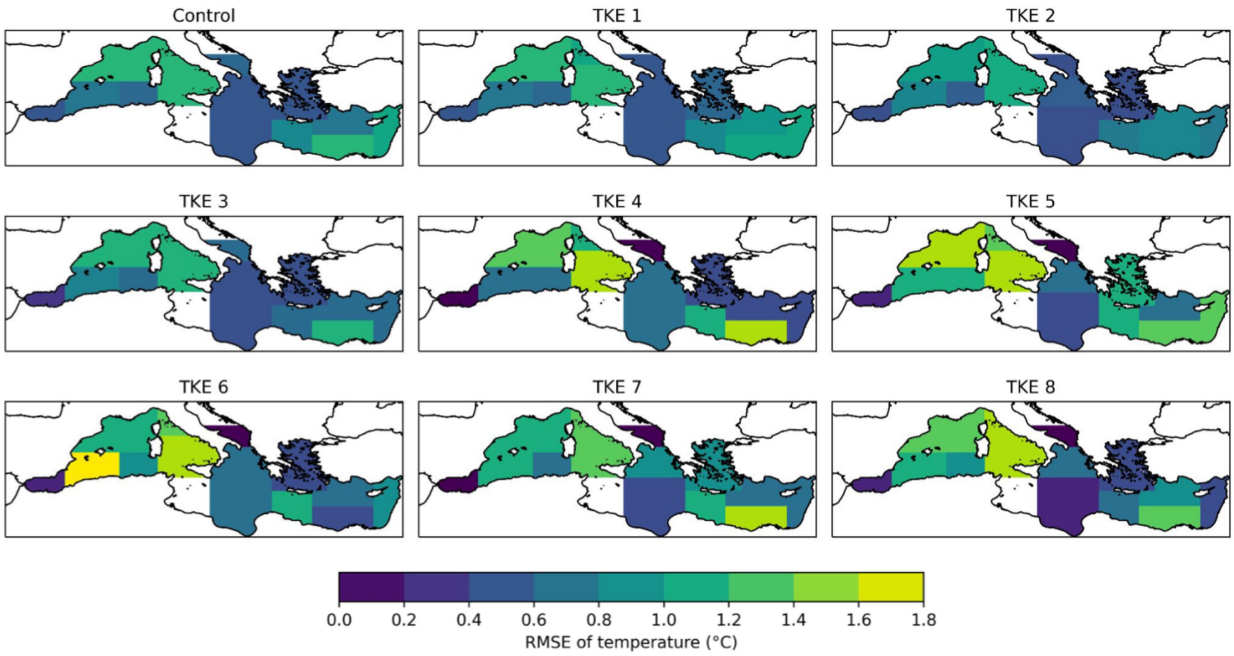

Figure 2.14: RMSEs of temperature by region (see Figure 2.8) at 60-100m in 2017, for the eight TKE experiments and the Richardson number reference run (Control).

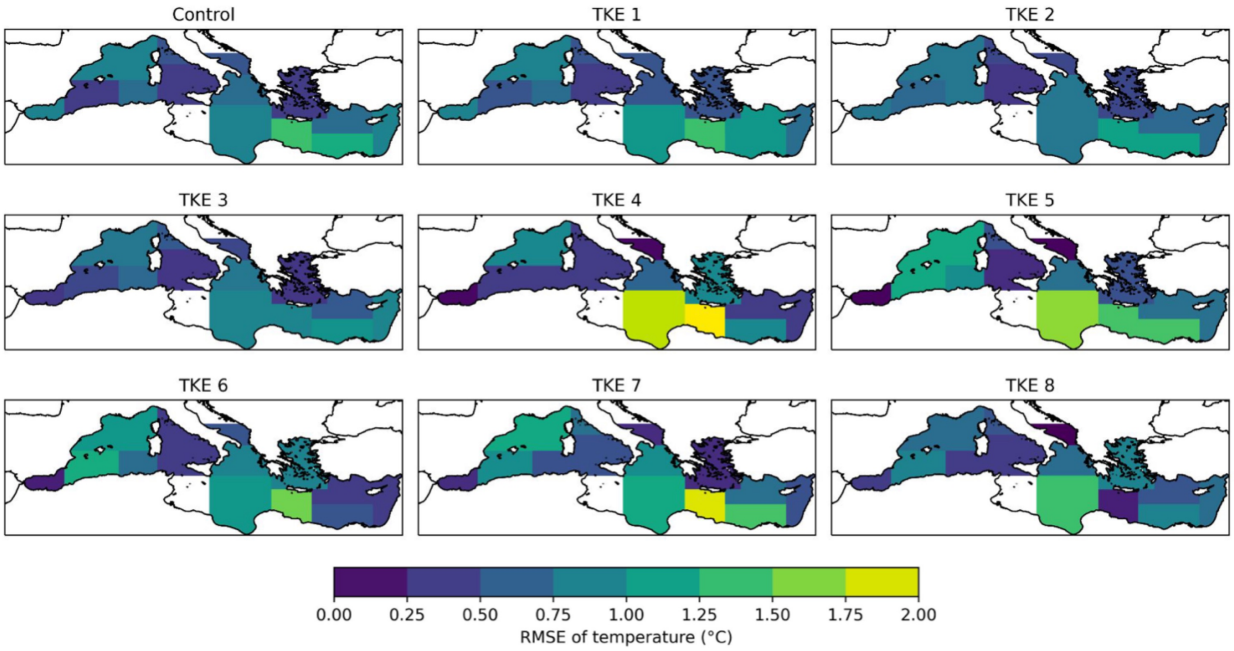

Figure 2.15: RMSEs of temperature by region (see Figure 2.8) at 100-150m in 2017, for the eight TKE experiments and the Richardson number reference run (Control).

surface. These experiments were extended to 2019, to validate them against a larger set of observations and to select the best experiment considering this.

One way to compare the experiments that was not done in Section 2.4.6 is seasonally. Figures 2.16 and 2.17 contain profiles by month of the year of salinity and temperature in the upper 150m. There is clear seasonality in the RMSEs of both salinity and temperature, with autumn values being higher than in other seasons. This RMSE maximum occurs at the bottom of the thermocline, which deepens from 25m in August to 75m in December. In these months, the peak temperature RMSE is high in all experiments, including the Richardson number parameterization, although TKE generally performs worse in all of its configurations. However, in other seasons, TKE3 begins to emerge as the most successful of the TKE experiments: between the months of February-August, as well as November-December, the average RMSE in the upper 150m is no more than 0.03°C higher than it is in the Pacanowski and Philander (1981) parameterization. TKE3 is also consistently better than the Richardson number parameterization in terms of salinity, with lower or equal RMSE in the upper 150m in ten months of the year. TKE1 is the best-performing experiment in salinity alone, but is consistently further from temperature observations, with large RMSEs in some months compared to the other TKE schemes.

2.4.8 Summary

Eight experiments were carried out using different parameter choices within the TKE scheme available in the NEMO model. Initially, one year (2017) of data was analysed, then the best-performing three experiments were carried forward for a three-year extension (2017-2019). Model outputs for the Mediterranean Sea were analysed, and model validation compared to observations were carried out in order to assess the best-performing experiments.

It is notable that although some TKE experiments (TKE1 and TKE3) perform as well as the Richardson number parameterization in many regions, especially regarding salinity, there is no TKE experiment which is markedly better than the control. The best-performing TKE experiment in terms of the RMSE of temperature profiles in the subsurface is TKE3,

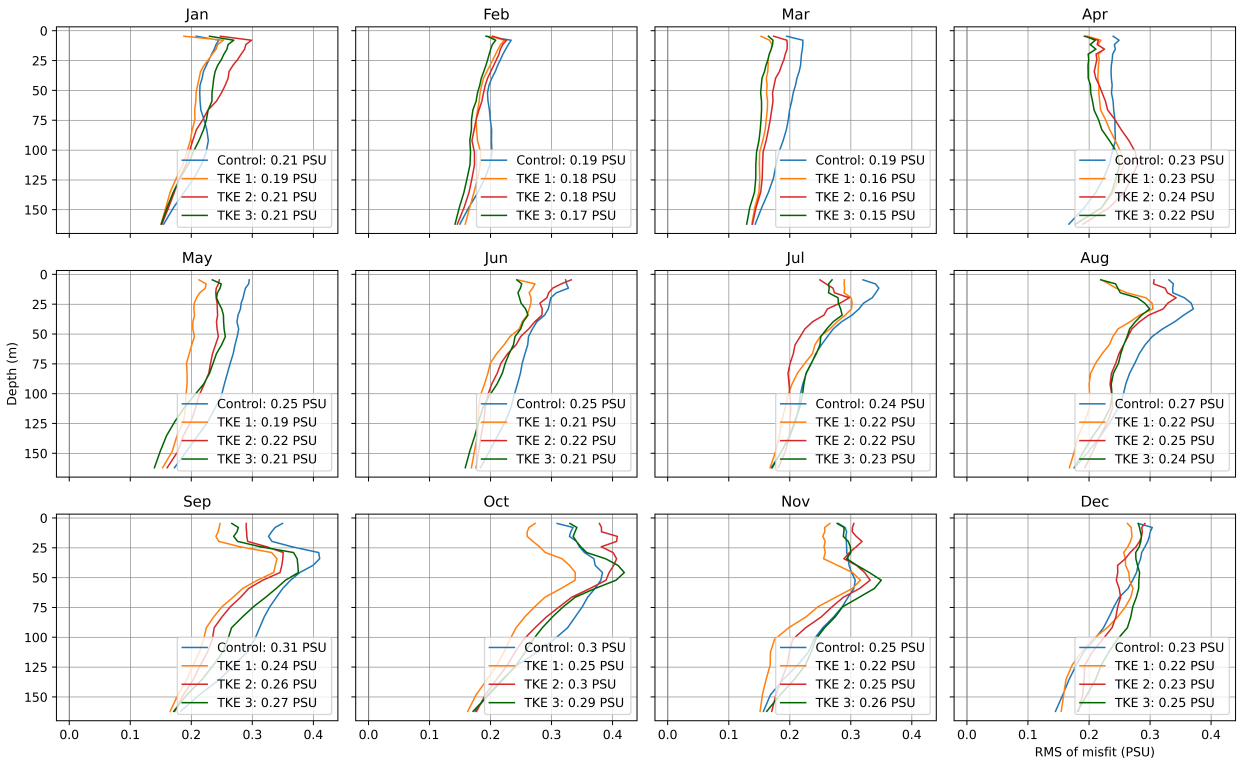

Figure 2.16: Profiles of the RMSE of salinity by month in three extended TKE experiments: TKE1 (orange), TKE2 (red), TKE3 (green), and the Richardson number reference run (Control, blue), for the Mediterranean Sea in 2017-2019.

which has EVD set to 10 ms^{-2} but the Langmuir cell parameterization switched off. This demonstrates that some enhanced mixing is required to boost the mixing of the TKE scheme itself. The Langmuir cell parameterization alone doesn't provide enough additional mixing to give accurate results for temperature in the subsurface layers in these experiments.

Some other approaches could lead to improved TKE results in future work: one of these would be to carry out TKE experiments using a wave-current coupled model. This would allow for full utilisation of the Langmuir circulation parameterization, rather than a formula based on wind stress. Another limitation of this work is the limited number of parameter combinations tested. An approach that utilises machine learning to tune parameters could be more successful for selecting parameters for a scheme that performs best for this implementation of NEMO, since it is not feasible to manually run the hundreds of experiments that would be required to fully tune all TKE parameters. Further to this, optimal mixing parameterization choices depend on model resolution, since different phenomena are

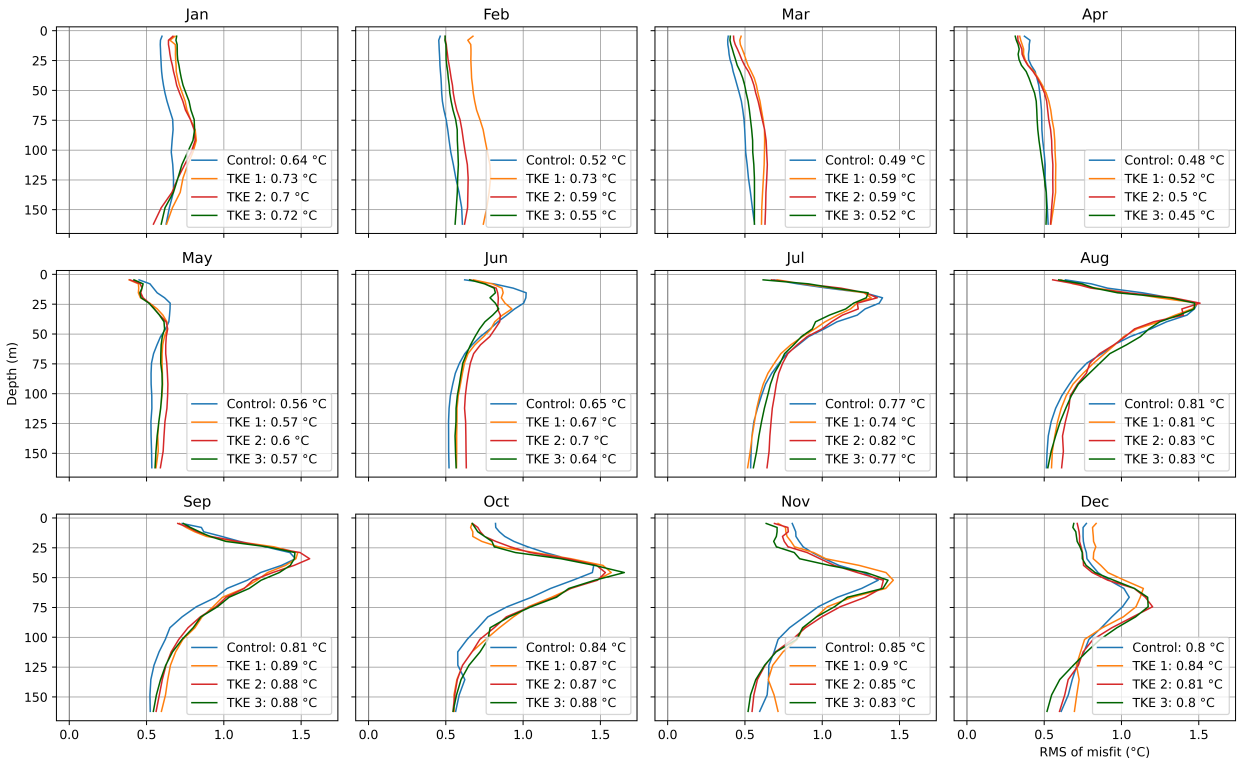

Figure 2.17: Profiles of the RMSE of temperature by month in three extended TKE experiments: TKE1 (orange), TKE2 (red), TKE3 (green), and the Richardson number reference run (Control, blue), for the Mediterranean Sea in 2017-2019.

resolved at any given resolution. Increasing resolution could particularly aid the regional differences between experiments, because more regional phenomena could be represented.

The regional differences in results also demonstrate that a phenomena-based approach could achieve more accurate mixing across the Mediterranean Sea, rather than the current approach of choosing the scheme which compromises some of this for the lowest RMSE across the whole basin. It is clear that narrow straits such as the Gibraltar Strait require one approach, while eddy-rich regions such as the south-west Mediterranean Sea require a different approach, and regions with large amounts of surface gravity waves or internal waves likely require a separate treatment. Additionally, it is notable that EVD is required to sufficiently mix the ocean, but this applies to some regions more than others. Regions of open-ocean deep water formation need this enhanced mixing in order to de-stratify in winter, and the Gibraltar Strait also requires more artificial mixing than in most of the more stratified regions of the Mediterranean Sea. Adjusting the EVD values by region

could be a useful next step for these experiments. However, caution should be taken to avoid overtuning the model when adjusting on a granular level, and parameters could instead be chosen based on which phenomena are most important to represent well in a specific application.

2.5 Analysis methods

In this thesis, spectra are used on many occasions to analyse the frequencies and wavelengths at which tides, both barotropic and baroclinic, have an impact on the ocean dynamics at a variety of temporal and spatial scales. In the following sections, each type of spectrum that is used in Chapters 3 and 4 is briefly defined.

2.5.1 Spectrum calculation

For all spectra, a periodogram is used as an estimate of the spectrum. The main advantages of using the periodogram over other estimators of a spectrum is that a periodogram is asymptotically unbiased, and estimates at adjacent frequencies are almost uncorrelated. The periodogram is calculated as follows:

For a timeseries $x_1, ..., x_T$, where $x_t, t = 1, ..., T$ is periodic and can be expanded in terms of sine and cosine functions, x_t is;

$$x_t = a_0 + \sum_{j=1}^{q} (a_j \cos(2\pi\omega_j t) + b_j \sin(2\pi\omega_j t)), \omega_j = \frac{j}{T}, j = 1, ..., q, q = \frac{T^*}{2} \tag{2.11}$$

where T^* is the largest integer within $T/2$, and

$$a_0 = \frac{1}{T} \sum_{t=1}^{T} x_t \tag{2.12}$$

$$a_j = \frac{2}{T} \sum_{t=1}^{T} x_t \cos(2\pi\omega_j t) \tag{2.13}$$

$$b_j = \frac{2}{T}\sum_{t=1}^{T} x_t \sin(2\pi\omega_j t) \tag{2.14}$$

The periodogram at the frequency ω_j is then:

$$I_{T_j} = \frac{T}{4}(a_j^2 + b_j^2), j = \frac{T^* - 1}{2}, ..., \frac{T^*}{2}. \tag{2.15}$$

This periodogram is used to estimate power spectra from timeseries at a single point throughout Chapters 3 and 4.

Where a spectrum is required over an area, for example the sea surface height spectra in Chapter 3, the periodogram is calculated for each point in the region, and then an area-weighted mean of the periodograms for each point is taken. Area averages are not used for kinetic energy, since the vertical structure of currents can change from one point to the next due to topography, and taking a mean over many points could remove the signature of any internal waves present.

2.5.2 Rotary spectrum

To estimate the spectrum of kinetic energy, using both zonal and meridional currents, a rotary spectrum is used to decompose this vector timeseries into clockwise and counter-clockwise components. For two components of velocity, u and v, which can be expanded into sine and cosine components as:

$$u(t) = A\cos(\omega t) + B\sin(\omega t) \tag{2.16}$$

$$v(t) = C\cos(\omega t) + D\sin(\omega t) \tag{2.17}$$

They can also be written in complex form as:

$$R = u + iv \tag{2.18}$$

$$R = A\cos(\omega t) + B\sin(\omega t) + i[C\cos(\omega t) + D\sin(\omega t)] \tag{2.19}$$

$$R = (A + iC)\cos(\omega t) + (B + iD)\sin(\omega t) \tag{2.20}$$

R can also be written as a sum of clockwise (R^+) and counterclockwise (R^-) components:

$$R = R^+ e^{i\omega t} + R^- e^{-i\omega t} \tag{2.21}$$

$$R = R^+(\cos(\omega t) + i\sin(\omega t)) + R^-(\cos(\omega t) - i\sin(\omega t)) \tag{2.22}$$

$$R = (R^+ + R^-)\cos(\omega t) + (R^+ - R^-)\sin(\omega t) \tag{2.23}$$

Equating the coefficients of R^+ and R^-:

$$R^+ = \frac{1}{2}[A + D + i(C - B)] \tag{2.24}$$

$$R^- = \frac{1}{2}[A - D + i(C + B)] \tag{2.25}$$

Finally, to estimate the spectrum of kinetic energy, the sum of the squares of the clockwise and anticlockwise components of the spectrum is calculated. The rotary spectrum can also be plotted as separate clockwise and counterclockwise components in order to separate phenomena which only appear in one direction, such as near-inertial waves which only appear in the clockwise component.

2.5.3 Wavenumber spectrum

In addition to spectra in frequency space, in Chapter 4, wavenumber spectra are calculated to find the wavelengths of the internal tides. These spectra are calculated in wavenumber space, along a length of physical space at a specific time, rather than in frequency space using a time series of data. The periodogram is also used for this calculation, replacing the frequency ω_j with the wavenumber k_j and the time period T with wavelength λ. In Chapter 4, a harmonic analysis of currents for each tidal component is used to calculate the periodogram, to analyse the wavelengths at tidal frequencies.

Chapter 3: The characteristics of tides and their effects on the general circulation of the Mediterranean Sea

The following chapter was re-submitted, after revisions, to the journal *Ocean Science* on 18th March 2024. The manuscript, along with supplementary material is available online (McDonagh et al., 2023) at the time of submission of this thesis. The supplementary material is available at the same reference, and in Appendix B of this thesis.

I acknowledge the co-authors Emanuela Clementi, Anna Chiara Goglio, and Nadia Pinardi, who contributed to this chapter, and the two anonymous reviewers who generously gave their time to give me feedback on this work. The contributions are as follows: BM ran the numerical models, analysed the results, and wrote the manuscript. EC and AG provided support in the set-up and running of the numerical models and analysis. NP planned the study and supported the analysis of model results. All authors reviewed and edited the manuscript.

The characteristics of tides and their effects on the general circulation of the Mediterranean Sea

Bethany McDonagh[1,2], Emanuela Clementi[1], Anna Chiara Goglio[1], and Nadia Pinardi[2]

[1]CMCC Foundation - Euro-Mediterranean Center on Climate Change, Italy
[2]Department of Physics and Astronomy, University of Bologna, Italy

Correspondence: Bethany McDonagh (bethany.mcdonagh@cmcc.it), Emanuela Clementi (emanuela.clementi@cmcc.it)

Abstract. The effects of tides on the Mediterranean Sea's general circulation, with a particular focus on the horizontal and vertical currents, are investigated using twin simulations with and without tides. Amplitudes of tides in the region are typically low, but an analysis of the potential and kinetic energy demonstrates that tides have effects across many spatial and temporal scales in the basin, including nonlinear effects at short periods (less than one day) with high kinetic energy peaks at near-inertial, basin modes and tidal frequencies. Internal tidal waves are also revealed below 100m. Tides are found to amplify several basin modes of the Mediterranean Sea, broaden several tidal frequency energy spectra bands, as well as interact energetically with near-inertial waves. Tides increase the mixed layer depth in the Mediterranean Sea, particularly in the deep and intermediate water formation areas of the Western and Eastern basins, and the addition of tides also enhances Western Mediterranean Deep Water formation.

1 Introduction

Tidal forcing is a rather recent addition to large-scale circulation models of the ocean, since horizontal and vertical resolutions have recently become fine enough to allow for an explicit and more accurate representation of tides. This has given rise to novel opportunities to analyse tides and their impacts on the ocean circulation. For an overall review of the topic, see Arbic (2022). Tides are now considered to be essential components of the large scale circulation (St. Laurent et al., 2002; Müller et al., 2010; Melet et al., 2016), their global average input energy is 3.5 TW (Simmons et al., 2004), the second largest after winds (Ferrari and Wunsch, 2010), and they generate internal tides that then drive internal mixing (de Lavergne et al., 2020). Tides are also an important phenomenon in coupled numerical models, which represents a new opportunity in high-resolution modelling of the ocean and atmosphere (Arbic, 2022), and long-term simulations.

Internal tides are characterised by relatively large vertical velocities with respect to the Ekman suction and pumping, while their horizontal wavelength is similar to the general circulation scales (Oddo et al., 2023). Recently, observational and modelling studies have begun to advance our understanding of internal tides in several regions of the Mediterranean Sea. The presence of internal tides generated in the Gibraltar Strait is discussed in Morozov et al. (2002) and Vlasenko et al. (2009). Diurnal internal tide oscillations are generated around the Adriatic Sea islands in observational studies (Mihanović et al.,

2009), leading to baroclinic trapped waves. In a recent paper, Oddo et al. (2023) found observational and modelling evidence of internal tides at the Sicily-Malta escarpment due to the diurnal tidal components, connected to the bathymetric gradients.

For the Mediterranean Sea, several authors have depicted the importance of tidal motion in the Gibraltar Strait (Armi and Farmer, 1985; Candela et al., 1990; Harzallah et al., 2014). Armi and Farmer (1985) and Farmer et al. (1988) first observed the hydraulic control points that are induced by tides, and the importance of tidal dynamics and their variability in the region have been more recently discussed by Vázquez et al. (2006), Sánchez-Román et al. (2012), García-Lafuente et al. (2013), and Hilt et al. (2020). Naranjo et al. (2014) and Harzallah et al. (2014) found that tides at the Strait of Gibraltar: (1) intensify the high frequency dynamics in the Gibraltar Strait, and (2) increase the salinity and, to a lesser extent, decrease the temperature of Atlantic inflowing waters through the enhancement of mixing, affecting the water mass formation processes further downstream from the Strait. Tides also change the Mediterranean water outflow, as demonstrated by Izquierdo and Mikolajewicz (2019), where outflowing water is modified with tides, demonstrating the role of tides in the spreading of outflowing water. Moreover, Ambar and Howe (1979) found that tides increase the variability of outflowing salinity.

Other features of the Mediterranean Sea that bear importance when discussing tides are the free barotropic oscillations induced by atmospheric pressure and wind forcing. The Mediterranean Sea's first barotropic basin mode is at 38.5 hours (Schwab and Rao, 1983), beyond that of diurnal tides, but higher modes also exist at 11.4, 8.4, and 7.4 hours (Schwab and Rao, 1983), and 8 hours (Lamy et al., 1981; Lozano and Candela, 1995). Many of these free oscillations could be affected or enhanced by tides, especially considering their proximity to tidal frequencies. The Adriatic Sea is characterised by seiches or free barotropic oscillations close to tidal frequencies: at 10.7 hours and 21.9 hours (Medvedev et al., 2020; Leder and Orlić, 2004; Schwab and Rao, 1983), and at 12.0 hours (Lozano and Candela, 1995). Medvedev et al. (2020) used tide gauge data to explicitly find that tides resonate with the Adriatic Sea modes, while Lozano and Candela (1995) discussed the interaction of the M2 tide with modes in the Gulf of Gabes, Adriatic Sea, Aegean Sea, and the Mediterranean Sea. Palma et al. (2020) found additionally that spectra of kinetic energy in the Sicily Channel are enhanced at 8 hours and 6 hours due to the nonlinear effects of tides. These works demonstrate the potential importance of interactions between tides and higher frequency features of the Mediterranean Sea, but the interaction between tides and barotropic oscillations in the Mediterranean Sea have not been investigated using a state-of-the-art numerical model.

In the North Atlantic, the addition of tides was found to improve the representation of the mixed layer depth and deep water formation in the Labrador Sea (Müller et al., 2010). Lee et al. (2006) found that in the same region, sea surface density was increased by the addition of tides to their model and found that this could enhance ventilation and overturning. Internal wave frequencies around 8 hours were also found by van Haren et al. (2014) in the northwestern Mediterranean Sea. These relationships have, to our knowledge, not been investigated in detail in the Mediterranean Sea.

In this work, we further characterise the tidal large scale circulation effects in the overall Mediterranean Sea. Analysis of the effects of tides on circulation has been carried out in the Western Mediterranean basin by Naranjo et al. (2014), in the Gibraltar Strait by Sannino et al. (2014) and Gonzalez (2023), in the Sicily Strait by Oddo et al. (2023) and Gasparini et al. (2004) and in the whole Mediterranean basin, the general circulation without tides was analysed by Pinardi et al. (2019). To our knowledge, the effects of tides on the circulation of the entire Mediterranean Sea has not been extensively investigated.

To do this, we analyse the differences between a general circulation ocean model with and without tides, focusing on changes in the spectra, in the horizontal and vertical dynamics both across the basin on average and in several water mass formation regions. Furthermore, we show the impact of tides in the Eastern Mediterranean Sea and the amplification of different basin modes by a tidal resonant mechanism.

In the Mediterranean Sea there are four key regions of deep and intermediate water formation (see Figure 1): the Gulf of Lion (Western Mediterranean Deep Water, WMDW) and South Adriatic (Eastern Mediterranean Deep Water, EMDW) for deep water formation, and the Cretan Sea (Cretan Deep Water, CDW, and Cretan Intermediate Water, CIW) and Rhodes Gyre (Levantine Deep Water, LDW, and Levantine Intermediate Water, LIW) for intermediate water formation (Pinardi et al., 2015). In these regions the vertical velocities are enhanced, and this paper will analyse the differences of water mass formation rates with and without tides in detail.

Section 2 describes the model and observational data used and the analysis methods, while Sections 3-7 contain the model results and conclusions as follows:

- Section 3: Sea level energy spectra
- Section 4: Kinetic energy spectra
- Section 5: Mixed layer depth and water mass formation
- Section 6: Temperature and salinity
- Section 7: Conclusions

2 Data and methods

The general circulation model used is NEMO v3.6, following the implementation of the Mediterranean Sea forecasting system operational in the framework of the Copernicus Marine Service (Coppini et al., 2023; Clementi et al., 2021). The area covered by the model is shown in Fig. 1. The model without tidal forcing is validated in Coppini et al. (2023) and as part of the model information in Clementi et al. (2019), while the experiment with tides is validated in the Quality Information Document in Clementi et al. (2021).

The model has $\frac{1}{24}^\circ$ uniform horizontal resolution with 141 uneven vertical levels, using z* vertical coordinates and partial steps. This model is eddy-resolving, since the Rossby radius of deformation is of the order of 10km in the Mediterranean Sea and the horizontal resolution of the model is approximately 4km. Atmospheric forcing fields are given by the six-hour European Centre for Medium-Range Weather Forecasts (ECMWF) analyses, at a horizontal resolution of $\frac{1}{8}^\circ$ (2015-2018) and $\frac{1}{10}^\circ$ (2019-2021) and they are used to compute momentum, water and heat fluxes using specifically designed bulk formulae (Pettenuzzo et al., 2010). Lateral open boundary conditions are used in the Atlantic Ocean and Dardanelles Strait, which are provided by the Copernicus Marine global analysis and forecast system (Galloudec et al., 2022) for the Atlantic Ocean, and a

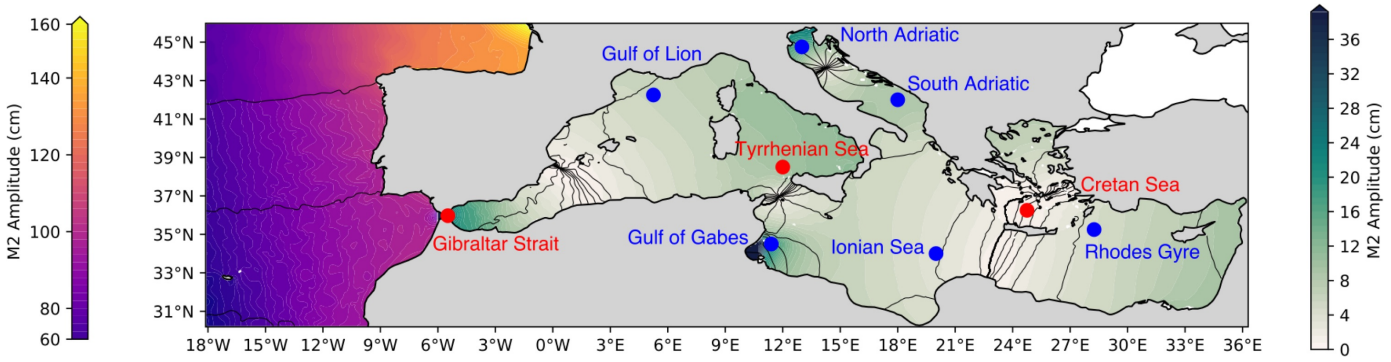

Figure 1. Map of the M2 tidal component amplitude in the Atlantic Ocean (contours, colourbar on the left) and Mediterranean Sea (contours, colourbar on the right) and M2 phase in black contour lines, with highlighted points in regions of open ocean dense water formation (Gulf of Lion, South Adriatic, Cretan Sea, and Rhodes Gyre) and regions of high tidal amplitude (Gibraltar Strait, Gulf of Gabes, North Adriatic Sea). Additional points that are studied further in Section 4 are also shown (Tyrrhenian Sea, Ionian Sea).

mixture of the aforementioned global model and daily climatology derived from a Marmara Sea box model (Maderich et al., 2015) at the Dardanelles Strait boundary. Further details of the boundary conditions are in Clementi et al. (2021).

Additionally, monthly mean climatological freshwater inputs from 39 rivers are added to the surface layer. Several datasets are used for this: the Global Runoff Data Centre dataset (Fakete et al., 1999) for the Po, Ebro, Nile, and Rhône rivers, the dataset from Raicich (1996) for the Vjosë and Seman rivers, the UNEP-MAP dataset (Demiraj et al., 1996) for the Buna and Bojana rivers, and the PERSEUS dataset (Deliverable of Perseus, 2012) for the remaining 32 Mediterranean rivers which have a mean run-off larger than 50 $\mathrm{m^3 s^{-1}}$. The bathymetry used is the GEBCO 30-sec bathymetry (GEBCO Bathymetric Compilation Group 2014, 2014), interpolated onto the model grid.

In the chosen configuration, vertical diffusivity depends on the Richardson number, calculated according to Pacanowski and Philander (1981). The Richardson number is a ratio of buoyancy to horizontal shear:

$$Ri = \frac{N^2}{\frac{\partial \bar{v}}{\partial z}^2} \tag{1}$$

where N^2 is the Brunt-Väisälä frequency, and $\frac{\partial \bar{v}}{\partial z}^2$ is the vertical shear of horizontal flow. Enhanced vertical viscosity and diffusivity are used where layers are unstable ($N^2 \leq -1 \times 10^{-12}\ \mathrm{s^{-2}}$) imposing a vertical diffusivity coefficient of 10 $\mathrm{m^2 s^{-1}}$. Vertical viscosity and diffusivity are then calculated according to:

$$A^{vT} = \frac{A^{vT}_{ric}}{(1 + aRi)^n} + A^{vT}_b \tag{2}$$

$$A^{vm} = \frac{A^{vT}}{(1 + aRi)} + A^{vm}_b \tag{3}$$

Tidal component	Period (hours)	Description
M2	12.421	Principal lunar semidiurnal tidal constituent
S2	12.000	Principal solar semidiurnal tidal constituent
K1	23.934	Lunisolar diurnal tidal constituent
O1	25.819	Lunar diurnal tidal constituent
N2	12.658	Larger lunar elliptic semidiurnal tidal constituent
P1	24.066	Solar diurnal tidal constituent
Q1	26.868	Larger lunar elliptic diurnal tidal constituent
K2	11.967	Lunisolar semidiurnal tidal constituent

Table 1. Tidal constituent components used in the model for this work, with their respective periods and astronomical descriptions.

where A^{vT} and A^{vm} are the vertical eddy viscosity and diffusivity respectively, and A_{ric}^{vT} (the maximum viscosity value, $100\times10^{-4}\ \mathrm{m^2s^{-1}}$), a, and n are adjustable parameters. In the model runs used, a and n are 5 and 2 respectively. Background vertical eddy viscosity and vertical eddy diffusivity values are $A_b^{vT} = 10^{-7}\ \mathrm{m^2s^{-1}}$ and $A_b^{vm} = 1.2\times10^{-6}\ \mathrm{m^2s^{-1}}$ respectively, which are typical values in the case of constant viscosity and diffusivity, representing diapycnal mixing from the breaking of internal waves. The constant values used here follow the NEMO implementation by Tonani et al. (2008).

Twin experiments are presented in this work with and without the representation of tides. In the experiment including tides, the 8 major tidal components for the Mediterranean Sea (M2, S2, K1, O1, N2, Q1, K2, P1) are represented, which are detailed further in Table 1. The M2 amplitude is displayed in Fig. 1 showing the well-known high amplitude areas at the Gibraltar Strait, the Gulf of Gabes and the Northern Adriatic Sea. Moreover, the Atlantic Ocean lateral open boundary fields include tidal forcing from TPXO9 (Egbert and Erofeeva, 2002).

Other than the addition of the tidal forcing itself, there are some further differences between the tidal and non-tidal modelling set-ups (see Table 2), with the primary difference being the time integration method. Both experiments use a split-explicit free surface formulation proposed in Shchepetkin and McWilliams (2005), solving the free surface equation and the associated barotropic velocity equations with a smaller timestep than the one used for the three-dimensional prognostic variables. The non-tidal experiment uses forward time integration, in which the external mode (barotropic timestep) is integrated between the current and the subsequent baroclinic time steps. This was not stable in the experiment including tides, so this instead uses a centred integration scheme, as recommended by the NEMO manual (Madec et al., 2019), where the baroclinic to barotropic forcing term given at the actual time step becomes centred in the middle of the integration window. The tidal experiment uses a shorter baroclinic timestep, 120s, rather than 240s in the experiment without tides, which was changed for stability purposes. The effects of these changes are negligible compared to the effects of adding tidal forcing to the model (see supplementary materials). The bathymetry was adjusted at several points in the tidal experiment for stability reasons: in the Bay of Biscay, at the northernmost part of the model domain, and several points were modified along the Croatian coastline to avoid generation of spurious tidal signals due to islands and complex bathymetry. All of the above changes in the tidal experiment compared to the experiment without tides are implemented as in Agresti (2018).

	Experiment without tides	Experiment with tides
Baroclinic timestep	240s	120s
Time integration scheme	Forward	Centred
Tides	No tidal forcing	8 tidal components: M2, S2, K1, O1, N2, P1, Q1, K2
Boundary conditions	No tidal signal at the boundary	Additional tidal signal at the Atlantic boundary: horizontal currents and sea surface height
Bathymetry	GEBCO 2014 interpolated onto model grid	Topography changed in 3 grid points at the boundary in the Bay of Biscay and 4 grid points in the Adriatic Sea

Table 2. Summary of the key differences between the tidal experiment and the experiment without tides.

The model was integrated for seven years (2015-2021), starting from climatological temperature and salinity initial conditions derived from the winter climatology (2005-2012) of the World Ocean Atlas (Boyer et al., 2013). The first two years are removed from the following analysis as they are considered as a spin-up period.

3 Sea level energy spectra

Figure 2 shows a spectrum of hourly sea surface height (SSH) in the Mediterranean Sea for five years, for both tidal and non-tidal experiments. The diurnal and semidiurnal tidal components represent the major differences between the two solutions, as expected. Further differences between the two models away from these tidal frequencies are also visible. Tides appear to modulate the spectrum at the mesoscales: energy is reduced in the tidal model at frequencies with a period longer than two days.

Peaks at both 24 hours and 12 hours are apparent, both with and without tides. In the case without tides, the energy peaks can be attributed to basin modes excited by atmospheric pressure forcing, as found by Oddo et al. (2014) using a similar NEMO configuration. In the semidiurnal range, the tidal model introduces a broad peak around 12 hours, as well as peaks at the individual tidal component frequencies. This is due to the amplification by tides of the basin modes near and at these frequencies. We argue that the broad 12h energy peak in Figure 2 in the tidal run is composed of the amplified 11.4h Mediterranean Sea basin mode energy (Schwab and Rao, 1983), the first Adriatic mode at 10.7h, known to be enhanced by tides (Medvedev et al., 2020; Schwab and Rao, 1983), and the 12h Adriatic/Aegean seas mode (Lozano and Candela, 1995). Peaks are also seen at 8h and 6h, which correspond to the kinetic energy frequencies in the Sicily Strait, noted by Palma et al. (2020), and in their work, these peaks were considered to come from non-linear effects of tides. The peak at 8h also aligns with the Western Mediterranean basin mode of 8.4h discussed in Schwab and Rao (1983), and the Gulf of Gabes mode at 8.2h (Lozano and Candela, 1995). Schwab and Rao (1983) also noted a fourth Mediterranean mode at 7.4h and the third Adriatic mode at 6.7h.

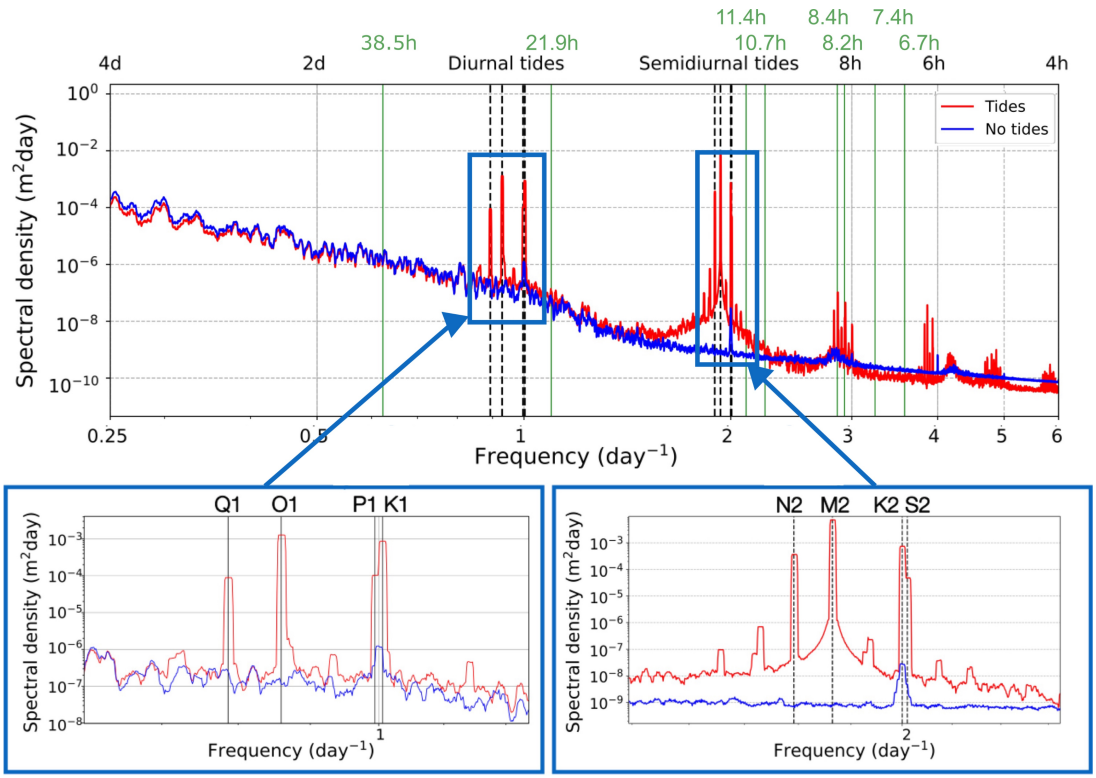

Figure 2. Energy density spectrum of hourly mean sea surface height in the Mediterranean Sea for the period 2017-2021, for the experiment without tides (blue) and with tides (red). Boxes below the figure show the key diurnal and semidiurnal ranges to highlight the representation of each individual tidal component. Green lines on the figure indicate frequencies of known barotropic oscillations in the Mediterranean Sea.

Considering the amplification of basin modes, Fig. 3 shows sea level spectra in the Adriatic Sea and Gulf of Gabes, to understand whether the peaks in Fig. 2 correspond to modes in these regions. In the Adriatic Sea (Fig. 3a), the sea level energy peaks at the frequencies of the barotropic modes of the Adriatic Sea at 11.4 hours, 6.7 hours (Schwab and Rao, 1983) and 12 hours (Lozano and Candela, 1995) are all enhanced by tides. The peaks are also visible in the model without tides, but with lower energy, thus confirming that these peaks are due to amplification of existing modes forced by winds and atmospheric pressure. In the Gulf of Gabes (Fig. 3b), tides also enhance the mode at 8.2 hours (Lozano and Candela, 1995).

Maps of the sea surface height power spectrum at 8.2h and 6h are shown for both experiments in Fig. 4. These frequencies are presented here as they show the largest differences between the two experiments, other than the tidal frequencies directly. Most of the Mediterranean Sea has enhanced power at 8.2h in the tidal experiment (Fig. 4a, c), with particularly large changes in the central Mediterranean: the Tyrrhenian Sea, the Gulf of Gabes, and the Adriatic Sea. The barotropic oscillation at 8.2h is in the Gulf of Gabes, according to Lozano and Candela (1995), but the third mode of the Mediterranean Sea (Schwab and Rao, 1983), and the nonlinear effects of tides in the central Mediterranean Sea according to Palma et al. (2020) are at frequencies close to this (8.4h and 8.0h respectively), and may also have an impact on Figure 4c. Since many of the calculations of

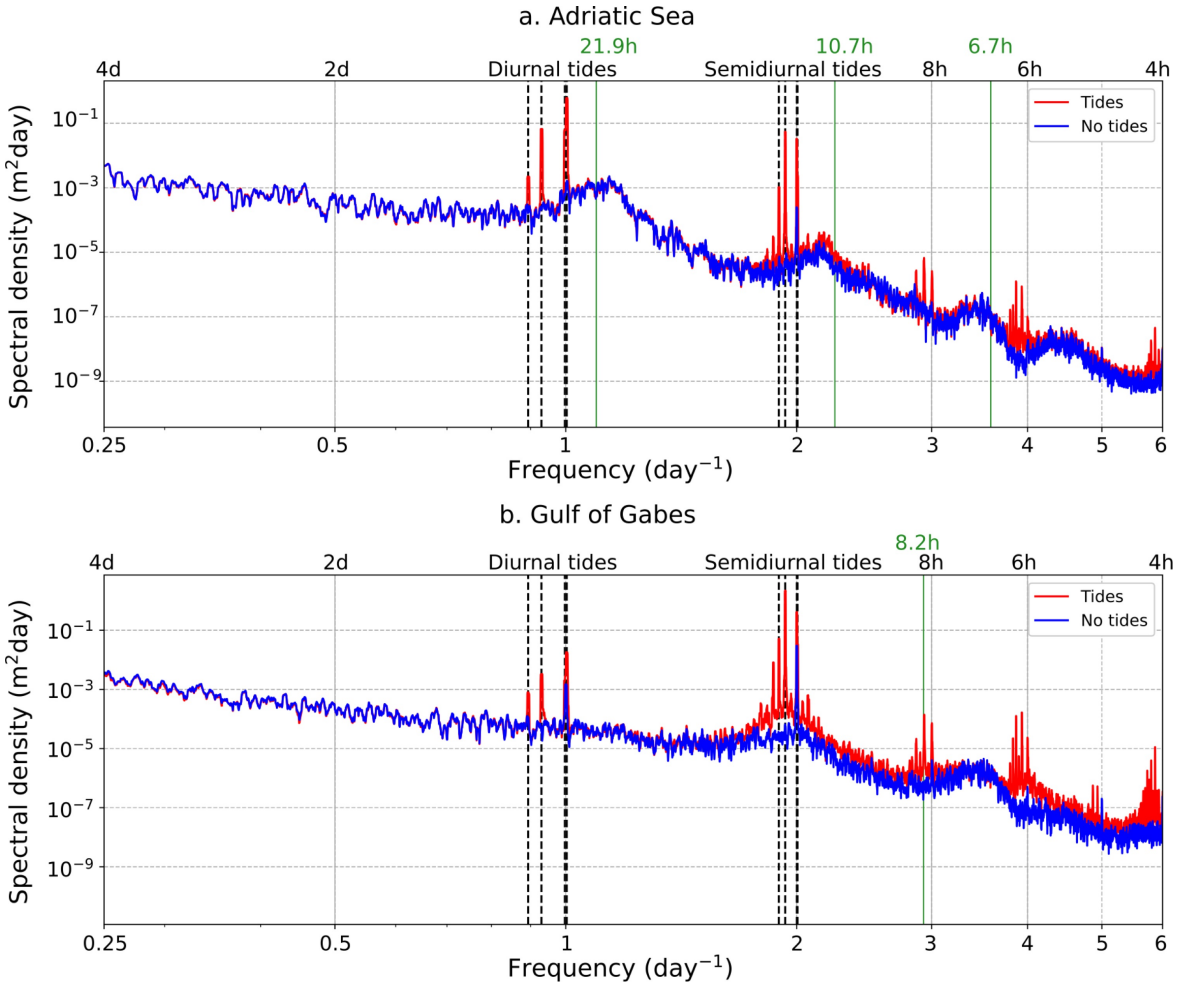

Figure 3. Energy density spectra of hourly mean sea surface height in the Mediterranean Sea for the period 2017-2021, for the model without tides (blue) and with tides (red), in a. Adriatic Sea (40.5°N-northern boundary), and b. Gulf of Gabes (32.5-35.5°N, 9.8-13.0°E). An area-weighted mean was taken for each of the sub-basins. Green lines on the figure indicate frequencies of known barotropic oscillations in each region.

barotropic oscillations in the Mediterranean Sea were made several decades ago, there is a need for an updated confirmation of the frequencies of barotropic oscillations using state-of-the-art methods. In Fig. 4b and 4d, we see that the Sicily escarpment region of Palma et al. (2020) again has particularly enhanced power in the experiment with tides, but other regions such as the Alboran Sea, and the western Mediterranean Sea see an interaction between tides and potential energy at the 6h frequency.

To summarise the analysis of sea surface height, we find that (1) tides affect the sea surface height on spatial and temporal scales away from those of the tides directly, (2) existing Mediterranean basin and regional barotropic oscillations at frequencies with a shorter time period than 12h are excited by tides, particularly at 6h and at several frequencies close to 8h, and (3) maps of the energy density at these frequencies reveal the distribution of these interactions in the Mediterranean Sea.

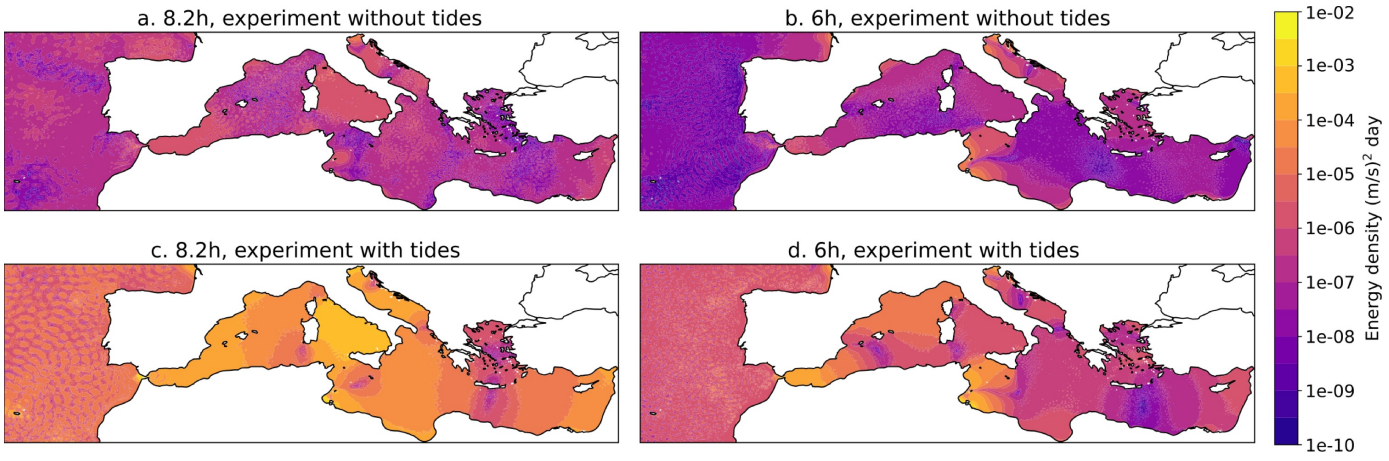

Figure 4. Maps of energy density of sea surface height at a. 8.2h without tides, b. 6h without tides, c. 8.2h with tides, and d. 6h with tides, for the Mediterranean Sea in 2017-2021.

4 Kinetic energy spectra

For this analysis, several points are selected across the Mediterranean Sea, to understand the effects of tides on local phenomena such as the generation of internal tides and interactions with near-inertial waves. The map in Fig. 1 shows these points. From this, three contrasting points were selected to be shown in this work: the Gibraltar Strait, the Tyrrhenian Sea, and the Cretan Sea. Results for the other points are available in the supplementary material.

We first calculate the rotary spectra for depth-averaged (barotropic) horizontal velocities (Fig. 5), for both clockwise and counter-clockwise components and then combine these to create the rotary kinetic energy density spectra. These rotary spectra visualise the time scales at which there is high kinetic energy at each selected point, over the entire water column. In the Gibraltar Strait (Fig. 5a), tides enhance kinetic energy at all frequencies, particularly at frequencies close to and higher than 12 hours. The basin mode frequency of 8.4 hours is enhanced by tides, and a peak at around 6h is also visible, which is due to nonlinear tidal effects (Palma et al., 2020). The Tyrrhenian Sea and Cretan Sea, unlike Gibraltar, have broad peaks at the near-inertial frequencies. Peaks at diurnal tidal frequencies are more apparent in the Tyrrhenian Sea than in the Cretan Sea.

We also analysed the kinetic energy spectra split into vertical levels, to consider baroclinic currents and internal wave modes, as shown in Fig. 6. We note that upper layer currents (0-150m) are characterised by the entering Atlantic Water layer dynamics, while the intermediate layer (150-500m) currents are on average in the opposite direction to the surface, characterising the Intermediate Water circulation in the basin. We now analyse the effects of tides on this anti-estuarine zonally oriented conveyor belt described in Pinardi et al. (2019). Figure 6 shows spectra for the three selected points throughout the water column.

In the Gibraltar Strait, it is clear that the entire structure of the kinetic energy is dominated by tides: tides enhance kinetic energy at almost all frequencies and depths (Fig. 6c). There are also internal tides visible in this region: Figure 6b shows peaks in kinetic energy at around 100m at the M2 and K1 tidal frequencies, implying the existence of internal tides in the Gibraltar Strait, as shown by Morozov et al. (2002), and more recently discussed in Gonzalez et al. (2023). Some diurnal internal tidal

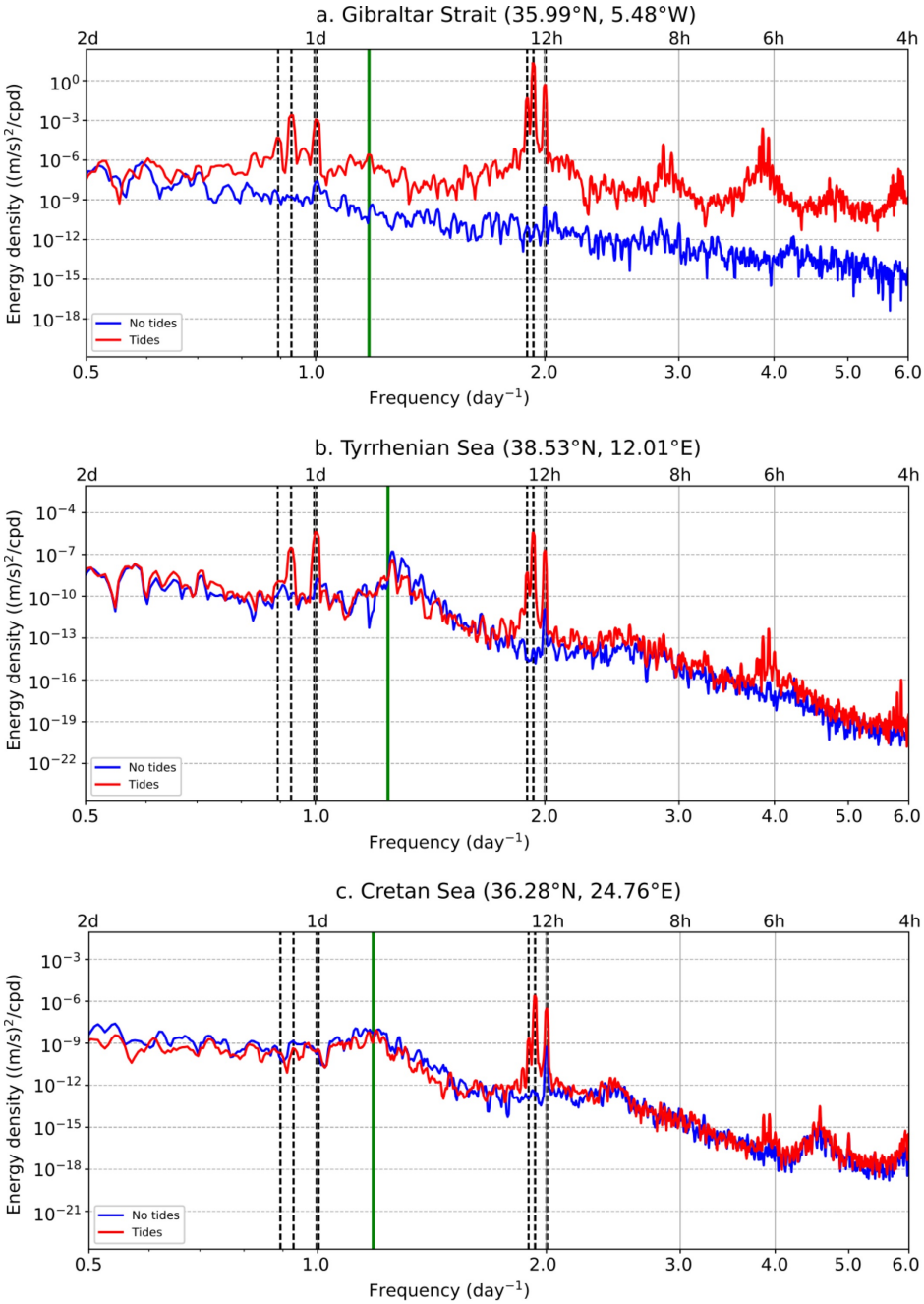

Figure 5. Barotropic (depth-mean) rotary kinetic energy density spectra for points in a. Gibraltar Strait (35.99°N, 5.48°W), b. Tyrrhenian Sea (38.53°N, 12.01°E), and c. Cretan Sea (36.28°N, 24.76°E), with the tidal experiment in red and the experiment without tides in blue, using hourly outputs over six months, January-June 2019. Dashed lines represent the eight tidal components used in the model, and the green line is the inertial frequency. The locations of these points are shown in Figure 1.

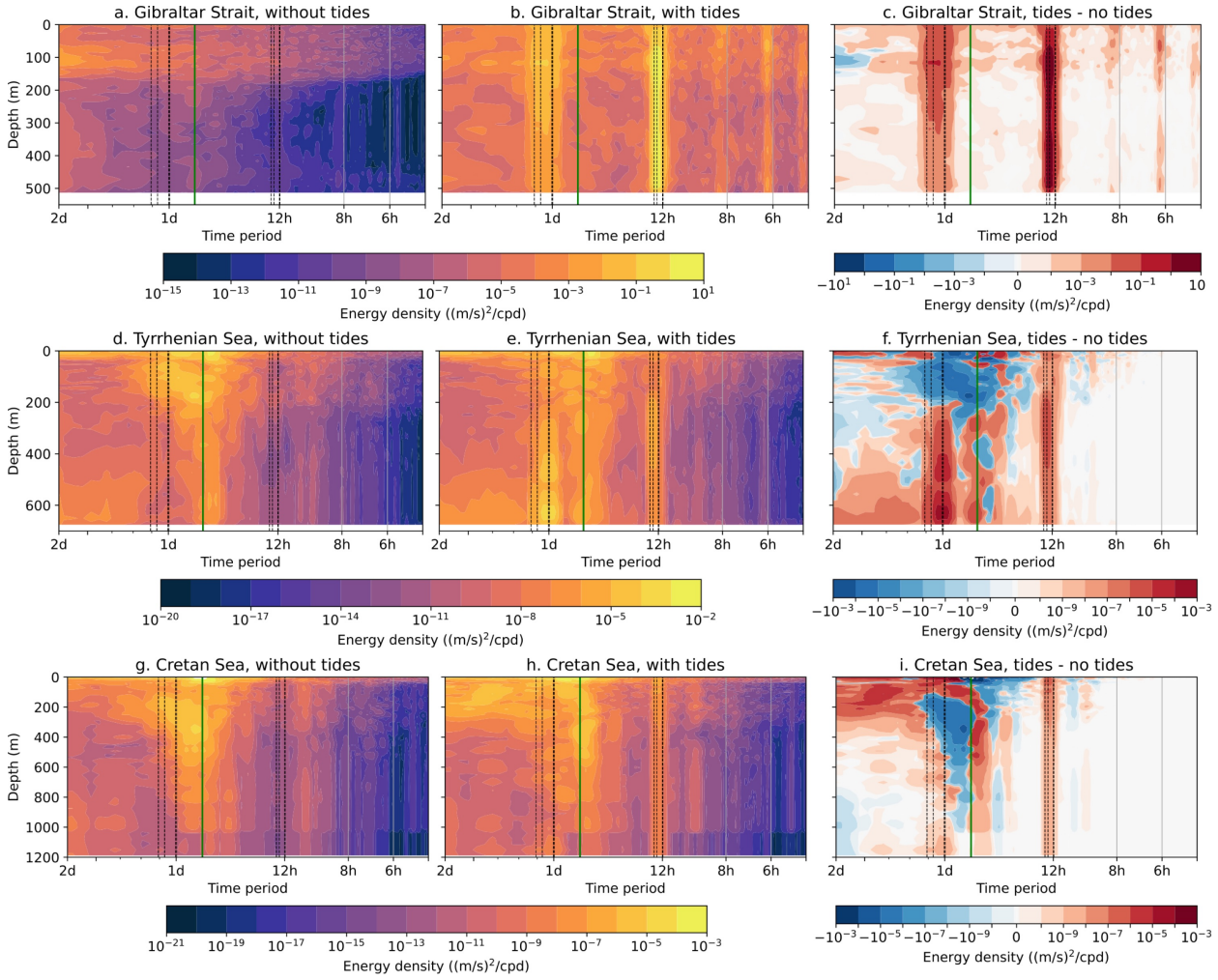

Figure 6. Rotary spectra of kinetic energy density over the full water column without tides at a. Gibraltar Strait (35.99°N, 5.48°W), d. Tyrrhenian Sea (38.53°N, 12.01°E), and g. Cretan Sea (36.28°N, 24.76°E), with tides at b. Gibraltar Strait, e. Tyrrhenian Sea, and h. Cretan Sea, and the difference between the two spectra at c. Gibraltar Strait (35.99°N, 5.48°W), f. Tyrrhenian Sea (38.53°N, 12.01°E), and i. Cretan Sea (36.28°N, 24.76°E). All data are for May 2019. The locations of these points are shown in Figure 1.

energy is visible in the Tyrrhenian Sea (Fig. 6e), as well as a shift in the near-inertial peak when compared to the experiment without tides (Fig. 6d). The interaction of tides with near-inertial waves is clearer in the Cretan Sea (Fig. 6i), as the peak is shifted to a higher frequency compared to Fig. 6e.

195 Internal tides are known to have large ageostrophic vertical velocities (Niwa and Hibiya, 2001; Li and von Storch, 2020) and thus an analysis of the vertical motion is mandatory. To visualise the internal tidal motion in the basin, we use Hovmoller diagrams for one month (May 2019) of hourly zonal currents for each of the three selected points from Fig. 6. In Fig. 7 the Gibraltar Strait location has a dominant vertical velocity oscillation at 12h. Contrastingly, inertial waves have greater

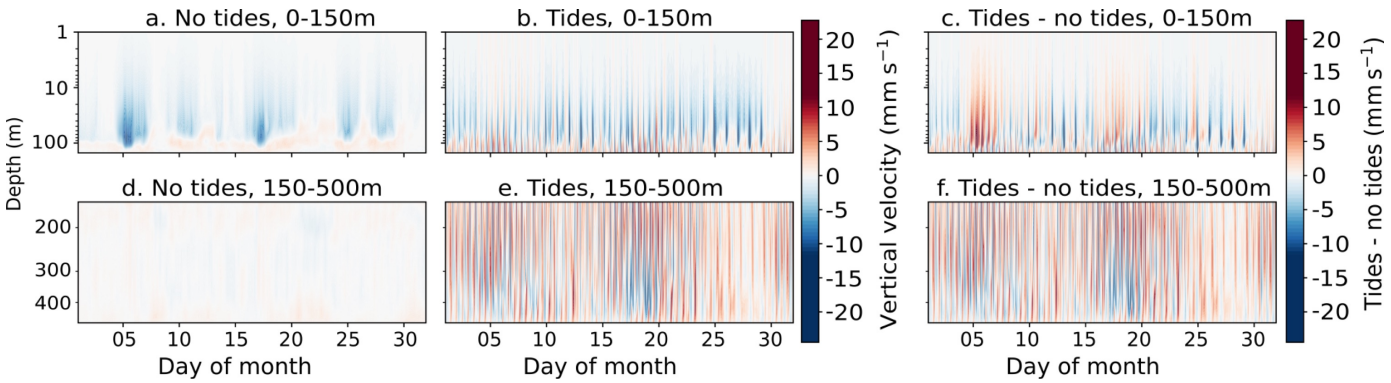

Figure 7. Hovmoller plots of depth against time of hourly mean vertical velocity at a point in the Gibraltar Strait (35.99°N, 5.48°W, see Figure 1) in May 2019, for a. Model without tides, 0-150m, b. Tidal model, 0-150m, c. Tidal model – model without tides, 0-150m, d. Model without tides, 150-500m, e. Tidal model, 150-500m, f. Tidal model – model without tides. Note that the depth scale is logarithmic.

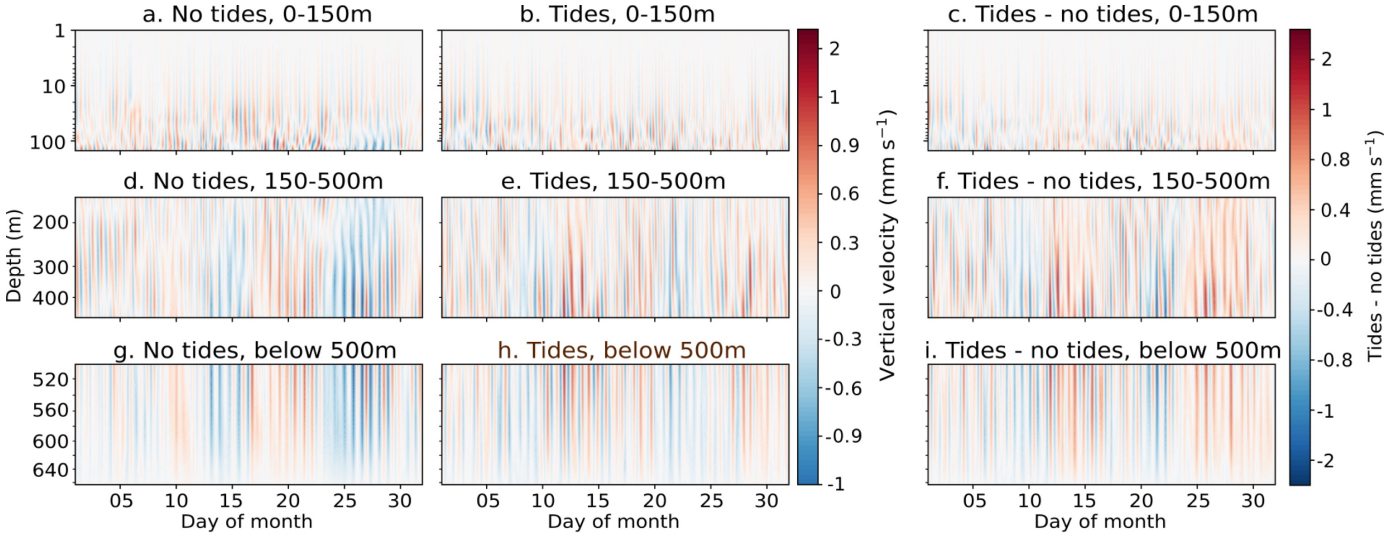

Figure 8. Hovmoller plots of depth against time of hourly mean vertical velocity at a point in the Tyrrhenian Sea (38.53°N, 12.01°E, see Figure 1) in May 2019, for a. Model without tides, 0-150m, b. Tidal model, 0-150m, c. Tidal model – model without tides, 0-150m, d. Model without tides, 150-500m, e. Tidal model, 150-500m, f. Tidal model – model without tides, g. Model without tides, below 500m, h. Tidal model, below 500m, i. Tidal model – model without tides, below 500m. Note that the depth scale is logarithmic.

importance in the Cretan Sea (Fig. 9) and they propagate downwards through the water column, notably around day 10-15 of
200 the month and at 150-500m (Fig. 9d). The effect of tides on this is shown in Fig. 9e, where interactions between the internal tidal and near-inertial waves create wave-wave patterns during the same period. The Tyrrhenian Sea (Fig. 8) also has both near-inertial waves and internal tides at these depths, but the interaction here is weaker.

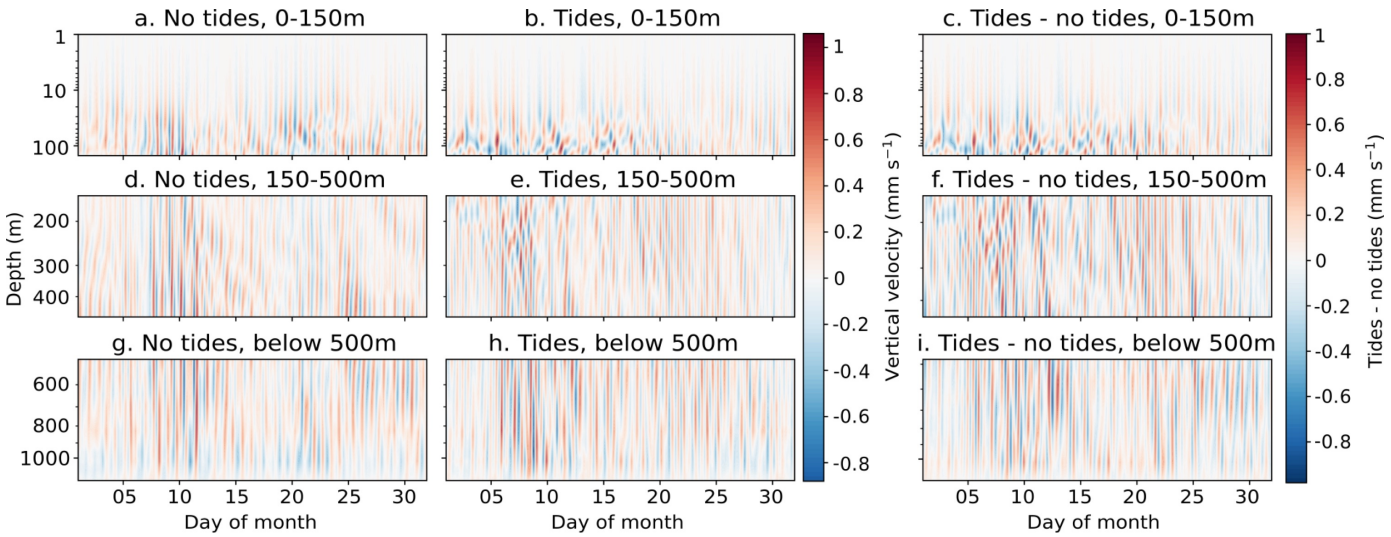

Figure 9. Hovmoller plots of depth against time of hourly mean vertical velocity at a point in the Cretan Sea (36.28°N, 24.76°E, see Figure 1) in May 2019, for a. Model without tides, 0-150m, b. Tidal model, 0-150m, c. Tidal model – model without tides, 0-150m, d. Model without tides, 150-500m, e. Tidal model, 150-500m, f. Tidal model – model without tides, g. Model without tides, below 500m, h. Tidal model, below 500m, i. Tidal model – model without tides, below 500m. Note that the depth scale is logarithmic.

An interesting feature of Figs. 7-9, is the baroclinic structure of the vertical velocity in the experiment with and without tides. Two zero crossings appear, one approximately at 150m, the lower limit of the inflowing branch of the zonal conveyor belt already described above (Pinardi et al., 2019), and the second at 300m. This is particularly apparent in the Gibraltar Strait (Fig. 7), where internal tide generation leads to increased tidal velocity in both directions. The continuation of this zero-crossing at 150m in other regions (Figs. 8-9) demonstrates the importance of internal tide generation at the Gibraltar Strait and how it affects the entire Mediterranean Sea general circulation, including in remote regions.

The three contrasting regions of the Mediterranean basin highlight the varying importance of tides, internal tides, and their interactions with near-inertial internal waves in different regions. While the Gibraltar Strait (Fig. 7) is dominated by semidiurnal tides, the other two regions (Figs. 8-9) show propagating near-inertial waves, as in (Cozzani, 2023), interacting with internal tides, particularly in the Cretan Sea.

5 Mixed layer depth and water mass formation

Assessing the impact of tides on the mixed layer depth is indirect evidence of the importance of internal tides on the vertical mixing and vertical velocities. The mixed layer depth is calculated via a density criterion based on a density change of 0.01 kgm^{-3} (de Boyer Montégut et al., 2004). Figure 10 shows the change in winter (December-March) mixed layer depth in the two experiments, and timeseries of the Mediterranean Sea mean mixed layer depth for the entire five-year period. There is an increase in winter mixed layer depth with tides throughout most of the basin, with notable exceptions in the Gibraltar

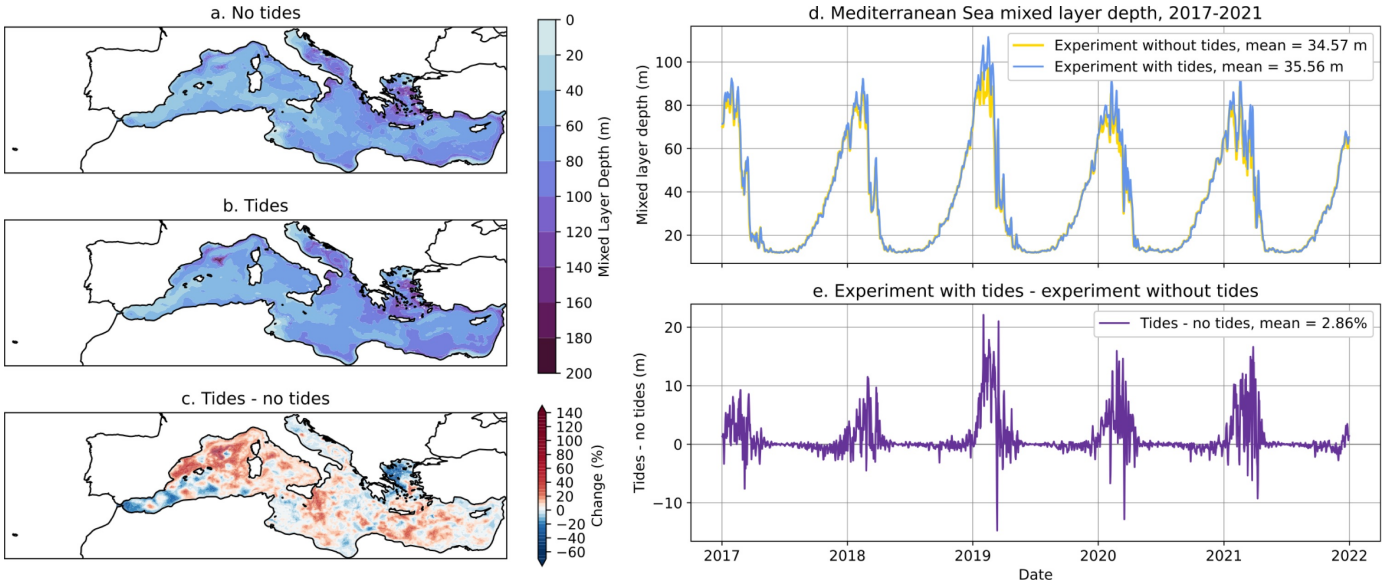

Figure 10. Winter (December-March) mean mixed layer depth in the Mediterranean Sea, for a. experiment without tides, b. experiment with tides, and c. the percentage difference between the tidal and non-tidal experiments. Timeseries of daily Mediterranean Sea mean mixed layer depth for 2017-2021 (d), and difference between tidal and non-tidal experiment timeseries (e).

Strait/Alboran Sea region, and in parts of the Aegean Sea. In the Gibraltar Strait, this is explained by a thicker interface layer (García-Lafuente et al., 2013), which shrinks the upper layer compared to the experiment without tides, reducing the depth at which the threshold density change for the mixed layer is reached. These effects extend into the upper-layer Alboran Sea water which originates in the Gibraltar Strait. In the Aegean Sea, despite having low amplitude barotropic tides, internal tides are present (Alford et al., 2012), and affect mixing at the bottom (Gregg et al., 2012), which likely in turn affects the water column structure in this shallow region.

However, the biggest change occurs in the Gulf of Lion region, a key area for the formation of deep water (Western Mediterranean Deep Water, WMDW, Fig. 1). Regarding the seasonality of mixed layer depth, both the absolute and percentage change due to tides is positive throughout the year, but is greatest in winter. We also note that the largest increase in the mean mixed layer depth in the tidal experiment is evident during winter 2019, which is also the year characterised by the largest WMDW formation (see Fig. 11). The deepening of the mixed layer can be a precursor for increased dense water formation, but a direct analysis of this would be needed to confirm whether tides are enhancing water mass formation as well as mixed layer depth, and we note that the analysis in this work does not directly establish a connection between the two processes. Other important processes such as weak stratification and localised currents are key precursors to deep water formation in the Western Mediterranean.

Pinardi et al. (2015) defined that intermediate water has densities of 29.1-29.2 kgm^{-3} and deep water has densities greater than 29.2 kgm^{-3}. Figure 11 shows the water mass formation rate in the deep and intermediate formation areas of Fig. 1 for each winter of the analysed period, with and without tides. The most notable change is in WMDW, particularly during the event

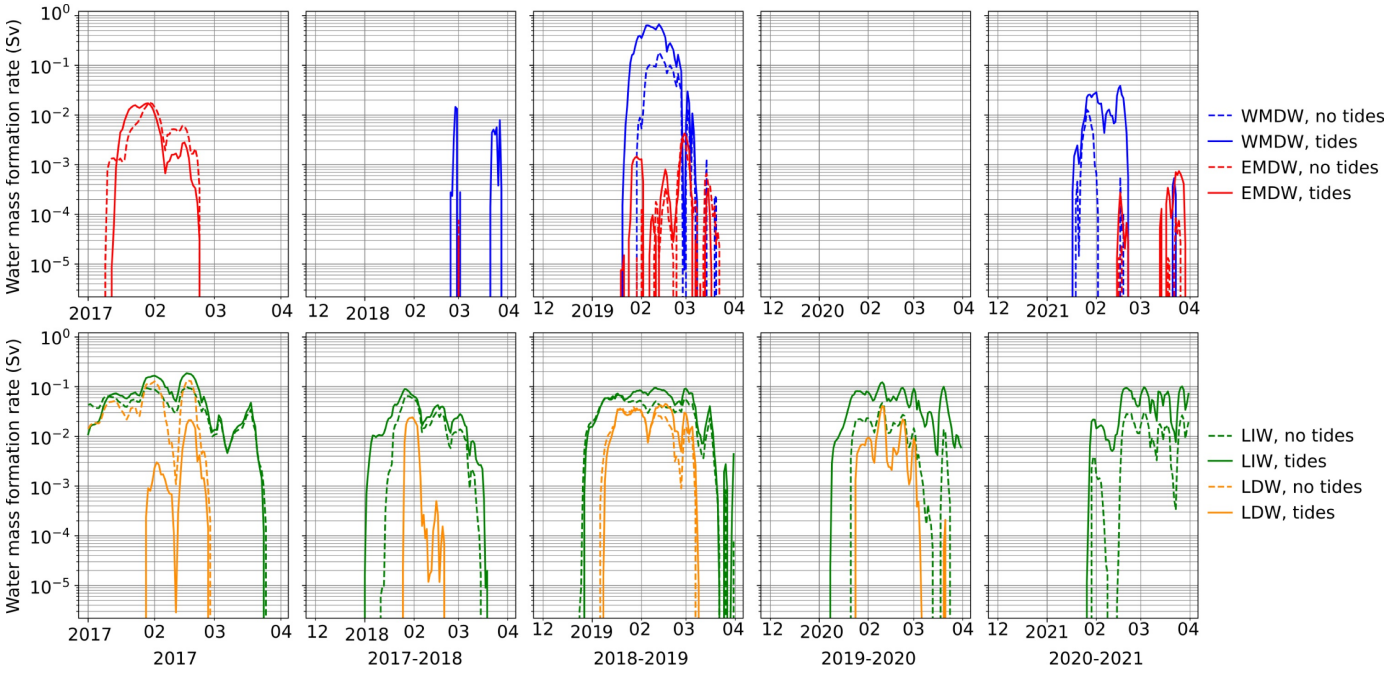

Figure 11. Daily water mass formation rate in winter 2017-2021, for the tidal experiment (solid lines) and the non-tidal experiment (dashed lines). Four types of water mass are included: Western Mediterranean Deep Water (blue), Eastern Mediterranean Deep Water (red), Levantine Intermediate Water (green), and Levantine Deep Water (orange).

of 2019, where the tidal experiment forms several times more deep water at its peak compared to the experiment without tides. This is in agreement with Naranjo et al. (2014) showing that enhanced WMDW formation occurred with tides in four out of the five years analysed. Modest increases are also seen in LIW formation. EMDW and LDW have increased water mass formation rate when including tides in some years, and decreased in other years. We argue that this irregular behaviour is connected to the impact of tides on the strength of the pre-conditioning factors and the air-sea interaction heat fluxes that are affected by tides (Oddo et al., 2023).

6 Temperature and salinity

The salinity and temperature of the Mediterranean Sea are affected by tides, primarily in the upper layer above 150m, as can be seen in Figure 12. This is the layer affected by the entering low salinity Atlantic water. As indicated in work by Naranjo et al. (2014), Harzallah et al. (2014), Sanchez-Roman et al. (2018), and Gonzalez et al. (2023), inflowing salinity at Gibraltar increases when tides are introduced and upper layer temperature decreases, albeit by a smaller amount. This salinity increase has an upward trend that in time does not stabilise in the few years of our experiment. This was also found by Harzallah et al. (2014), where the salinity difference between the experiments with and without tides increased for several decades before

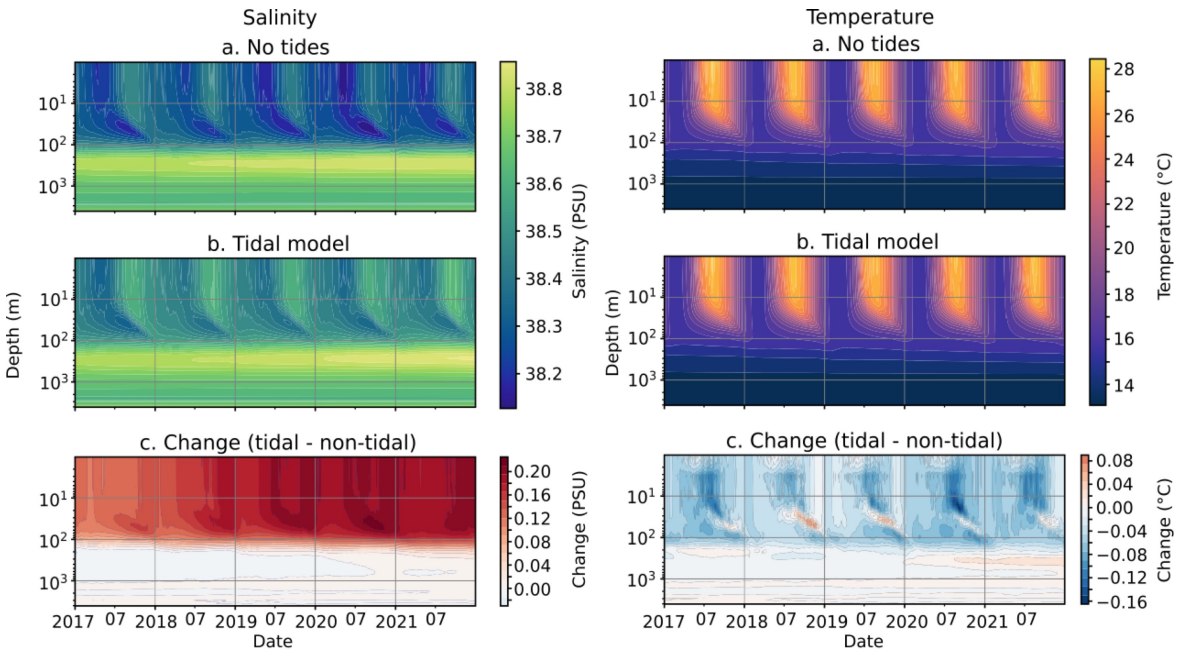

Figure 12. Hovmoller plot of depth against time of daily salinity (left) and temperature (right) in the Mediterranean Sea in 2017-2021, for the model without tides (a), with tides (b), and change (c): tidal model – model without tides. Note that the depth scale is logarithmic.

stabilising, since this stabilisation depends on the overturning time scales of the basin that could require several decades to spin up in full.

The additional increased salinity in the Mediterranean Sea due to tides and its trend over time can be compared to observations from profiling floats to understand whether the salinity increase follows the observational trend or it is overestimated. This was calculated for the Mediterranean Sea and integrated along vertical layers for each year in the experiment. Figure 13 shows the mean salinity Root Mean Square Error (RMSE) of the experiments with respect to observations averaged in the whole basin and provided along nine vertical layers. For the tidal experiment, the RMSE does not present a clear linear trend, instead varying by individual year. The lack of linear trend is also apparent in the non-tidal experiment, but there the salinity bias is positive throughout the upper layer. Overall the RMSE of the two experiments is similar in some years, but in 2019 and 2020, the tidal experiment has a much lower salinity RMSE in the upper layers. Figure 13 demonstrates that in both experiments the model error is larger at the surface up to 150m and is reduced to less than 0.15 PSU below this layer, where it also shows a lower temporal variability. Lower layers remain stable with small errors, whereas the surface varies more and produces larger errors when compared to observations.

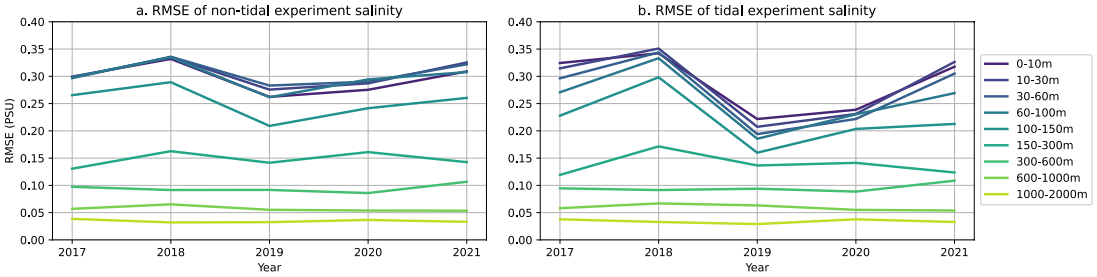

Figure 13. Salinity difference between the experiments and data from profiling floats for each analysed year (2017-2021), across nine layers for the Mediterranean Sea, presented as a. non-tidal experiment root mean square error, and b. tidal experiment root mean square error.

7 Conclusions

The effects of tides on the Mediterranean Sea circulation were studied through a twin numerical experiment approach based on a high-resolution (around 4km) model of the region, with and without the explicit representation of tides. Spectra of sea surface height and kinetic energy in the basin, as well as in key regions characterised by basin modes, revealed that the effects of tides on the energetics of the Mediterranean Sea extend far beyond the spatial and temporal scales of the tides themselves.

Tides enhance the power at 8h and 6h frequencies due to their nonlinear effects across the Mediterranean basin, amplifying the basin modes, as shown in the Sicily Strait by Palma et al. (2020). Tides also interact and amplify the other basin modes at 11.4h, 8.4h, and 7.4h, as well as the Adriatic modes at 10.7h and 6.7h, and the mode in the Gulf of Gabes at 8.2h. The Adriatic modes at 12h and 21.9h are visible in both the tidal and non-tidal experiments, but the 12h frequency is enhanced by tides. Results such as these demonstrate the complexity and non-linearity of tidal effects in the Mediterranean Sea.

The study then discussed the rotary spectra of the barotropic and full kinetic energy in several selected points in the Mediterranean Sea. This analysis showed the ubiquitous field of internal waves below around 150 meters, both at diurnal and semi-diurnal time frequencies. The Hovmoller diagrams of vertical velocity components revealed the internal tide field structure in the basin, as well as the interaction of internal tides with near-inertial waves in some regions, such as the Cretan Sea. In addition to near-inertial waves, both the semidiurnal and diurnal internal tides have high energy, potentially at an overall Mediterranean scale not previously highlighted.

Tides affect the mixed layer depth of the basin, with different signs in different regions. The Mediterranean deep and intermediate water formation is enhanced by tides in the WMDW region, and in the Levantine Sea where intermediate water masses are formed. This aligns with increases in the winter mixed layer depth across most of the Mediterranean Sea.

It is important to note that the resolution of this model configuration, although higher than many global ocean models and regional ocean models from past studies, has limitations in its representation of waves with shorter wavelengths, including internal tides. According to Li et al. (2015, 2017), the first two modes of the M2 internal tide and first three modes of the K1 internal tide all have wavelengths greater than 45 km, but higher modes are likely unresolved at the $\frac{1}{24}^{\circ}$ resolution. Furthermore, high vertical resolution is important for simulating internal tides. Our model lacks high vertical resolution at deeper levels, and this could contribute to a lack of internal tides in the deeper ocean.

Further work in this area should include process-oriented studies of some features in the Mediterranean Sea that were discovered by this work, but that are subregional structures. The current literature lacks an up-to-date study calculating the barotropic oscillations of the Mediterranean Sea using a state-of-the-art numerical model. A more detailed study focusing on the regions of formation and propagation of internal tides throughout the entire Mediterranean is lacking. In addition, a deeper focus on the impacts of tides, both barotropic and baroclinic, on vertical motion in the most vertically dynamic regions of the Mediterranean Sea would further help in understanding the overturning circulation in the basin. This could include considering the impact of tides on vertical mixing in deep and intermediate water formation regions, and how parameterization choices in numerical models may affect this. However, a longer simulation of several decades would be required to directly reveal the impact of tides on the overturning circulation of the Mediterranean Sea.

Author contributions. BM ran the numerical models, analysed the results, and wrote the manuscript. EC and AG provided support in the set-up and running of the numerical models and analysis. NP planned the study and supported the analysis of model results. All authors reviewed and edited the manuscript.

Competing interests. The authors declare that they have no conflicts of interest.

Acknowledgements. This study has been conducted including support from the University of Bologna Ph.D. programme in Future Earth, Climate Change, and Societal Challenge, and the EU Copernicus Marine Service for the Mediterranean Monitoring and Forecasting Center.

References

Agresti, V.: Effects of tidal motion on the Mediterranean Sea General Circulation, Ph.D. thesis, Alma Mater Studiorum University of Bologna, https://doi.org/10.6092/unibo/amsdottorato/8516, 2018.

Alford, M. H., Gregg, M. C., Zervakis, V., and Kontoyiannis, H.: Internal wave measurements on the Cycladic Plateau of the Aegean Sea, J. Geophys. Res., 117, https://doi.org/10.1029/2011JC007488, 2012.

Ambar, I. and Howe, M.: Observations of the Mediterranean outflow - I mixing in the Mediterranean outflow, Deep Sea Res., Part I, 26, 535–554, https://doi.org/10.1016/0198-0149(79)90095-5, 1979.

Arbic, B. K.: Incorporating tides and internal gravity waves within global ocean general circulation models: A review, Progr. Oceanogr., 206, https://doi.org/10.1016/j.pocean.2022.102824, 2022.

Armi, L. and Farmer, D.: The internal hydraulics of the Strait of Gibraltar and associated sills and narrows, Oceanol. Acta, 8, 37–46, 1985.

Boyer, T., Antonov, J. I., Baranova, O. K., Coleman, C., Garcia, H. E., Grodsky, A., Johnson, D. R., Locarnini, R. A., Mishonov, A. V., O'Brien, T., Paver, C., Reagan, J., Seidov, D., Smolyar, I. V., , and Zweng, M. M.: World Ocean Database 2013, NOAA Atlas NESDIS 72, Silver Spring, MD, https://doi.org/10.7289/V5NZ85MT, 2013.

Candela, J., Winant, C., and Ruiz, A.: Tides in the Strait of Gibraltar, J. Geophys. Res. Oceans, 95, 7313–7335, https://doi.org/10.1029/JC095iC05p07313, 1990.

Clementi, E., Pistoia, J., Escudier, R., Delrosso, D., Drudi, M., Grandi, A., Lecci, R., Cretí, S., Ciliberti, S., Coppini, G., Masina, S., and Pinardi, N.: Mediterranean Sea Analysis and Forecast (CMEMS MED-Currents, EAS5 system) (Version 1) [Data set], Copernicus Monitoring Environment Marine Service (CMEMS), https://doi.org/10.25423/CMCC/MEDSEA_ANALYSIS_FORECAST_PHY_006_013_EAS5, 2019.

Clementi, E., Aydogdu, A., Goglio, A. C., Pistoia, J., Escudier, R., Drudi, M., Grandi, A., Mariani, A., Lyubartsev, V., Lecci, R., Cretí, S., Coppini, G., Masina, S., and Pinardi, N.: Mediterranean Sea Physical Analysis and Forecast (CMEMS MED-Currents, EAS6 system), Copernicus Monitoring Environment Marine Service (CMEMS), https://doi.org/10.25423/CMCC/MEDSEA_ANALYSISFORECAST_PHY_006_013_EAS6, 2021.

Coppini, G., Clementi, E., Cossarini, G., Salon, S., Korres, G., Ravdas, M., Lecci, R., Pistoia, J., Goglio, A. C., Drudi, M., Grandi, A., Aydogdu, A., Escudier, R., Cipollone, A., Lyubartsev, V., Mariani, A., Cretì, S., Palermo, F., Scuro, M., Masina, S., Pinardi, N., Navarra, A., Delrosso, D., Teruzzi, A., Di Biagio, V., Bolzon, G., Feudale, L., Coidessa, G., Amadio, C., Brosich, A., Miró, A., Alvarez, E., Lazzari, P., Solidoro, C., Oikonomou, C., and Zacharioudaki, A.: The Mediterranean Forecasting System – Part 1: Evolution and performance, Ocean Sci., 19, 1483–1516, https://doi.org/10.5194/os-19-1483-2023, 2023.

Cozzani, E.: Oceanic near-inertial internal waves generation, propagation, and interaction with mesoscale eddies, Ph.D. thesis, Alma Mater Studiorum University of Bologna, 2023.

de Boyer Montégut, C., Madec, G., Fischer, A. S., Lazar, A., and Iudicone, D.: Mixed layer depth over the global ocean: An examination of profile data and a profile-based climatology, J. Geophys. Res., 109, https://doi.org/10.1029/2004JC002378, 2004.

de Lavergne, C., Vic, C., Madec, G., Roquet, F., Waterhouse, A. F., Whalen, C. B., Cuypers, Y., Bouruet-Aubertot, P., Ferron, B., and Hibiya, T.: A Parameterization of Local and Remote Tidal Mixing, J. Adv. Modell. Earth Sys., 12, e2020MS002 065, https://doi.org/10.1029/2020MS002065, 2020.

Deliverable of Perseus: Deliverable D4.6, SES land-based runoff and nutrient load data (1980–2000), edited by: Bouwman, L. and van Apeldoorn, D., 2012 PERSEUS H2020 grant agreement n. 287600, European Commission, http://www.perseus-net.eu/assets/media/PDF/deliverables/33216_Final.pdf, 2012.

Demiraj, E., Bicja, M., Gjika, E., Gjiknuri, L., Muçaj, L. G., Hoxha, F., Hoxha, P., Karadumi, S., Kongoli, S., Mullaj, A., Mustaqi, V., Palluqi, A., Ruli, E., Selfo, M., Shehi, A., and Sino, Q.: Implications of climate change for the Albanian Coast, Mediterranean Action Plan, MAP Technical Reports Series, 98, UNEP, 1996.

Egbert, G. D. and Erofeeva, S. Y.: Efficient inverse modeling of barotropic ocean tides, J. Atmosph. Oceanic Tech., 19.2, 183–204, 2002.

Fakete, B., Vörösmarty, C., and Grabs, W.: Global composite runoff fields based on observed river discharge and simulated water balances, Technical Report 22, Global Runoff Data Centre, Koblenz, Germany, 1999.

Farmer, D. M., Armi, L., Armi, L., and Farmer, D. M.: The flow of Atlantic water through the Strait of Gibraltar, Progr. Oceanogr., 21, 1–103, https://doi.org/https://doi.org/10.1016/0079-6611(88)90055-9, 1988.

Ferrari, R. and Wunsch, C.: The distribution of eddy kinetic and potential energies in the global ocean, Tellus, 62A, 92–108, https://doi.org/10.1111/j.1600-0870.2009.00432.x, 2010.

Galloudec, O. L., Chune, S. L., Nouel, L., Fernandez, E., Derval, C., Tressol, M., Dussurget, R., Biardeau, A., and Tonani, M.: Global Ocean Physical Analysis and Forecasting Product, Copernicus Monitoring Environment Marine Service (CMEMS), https://doi.org/10.48670/moi-00016, 2022.

García-Lafuente, J., Bruque Pozas, E., Sánchez Garrido, J. C., Sannino, G., and Sammartino, S.: The interface mixing layer and the tidal dynamics at the eastern part of the Strait of Gibraltar, J. Mar. Syst., 117-118, 31–42, https://doi.org/10.1016/j.jmarsys.2013.02.014, 2013.

Gasparini, G. P., Smeed, D. A., Alderson, S., Sparnocchia, S., Vetrano, A., and Mazzola, S.: Tidal and subtidal currents in the Strait of Sicily, J. Geophys. Res. Oceans, 109, https://doi.org/10.1029/2003JC002011, 2004.

GEBCO Bathymetric Compilation Group 2014: The GEBCO_2014 Grid, version 20150318, NERC EDS British Oceanographic Data Centre NOC, www.gebco.net, 2014.

Gonzalez, N. M.: Modélisation multi-échelle du détroit de Gibraltar et de son rôle de régulateur du climat méditerranéen, Ph.D. thesis, Sciences de l'Univers, de l'Environnement et de l'Espace, University of Toulouse, 2023.

Gonzalez, N. M., Waldman, R., Sannino, G., Giordani, H., and Somot, S.: Understanding tidal mixing at the Strait of Gibraltar: A high-resolution model approach, Progr. Oceanogr., 212, 102 980, https://doi.org/10.1016/j.pocean.2023.102980, 2023.

Gregg, M., Alford, M., Kontoyiannis, H., Zervakis, V., and Winkel, D.: Mixing over the steep side of the Cycladic Plateau in the Aegean Sea, J. Marine Sys., 89, 30–47, https://doi.org/10.1016/j.jmarsys.2011.07.009, 2012.

Harzallah, A., Alioua, M., and Li, L.: Mass exchange at the Strait of Gibraltar in response to tidal and lower frequency forcing as simulated by a Mediterranean Sea model, Tellus A: Dyn. Meteorol. Oceanogr., 66, 23 871, https://doi.org/10.3402/tellusa.v66.23871, 2014.

Hilt, M., Auclair, F., Benshila, R., Bordois, L., Capet, X., Debreu, L., Dumas, F., Jullien, S., Lemarié, F., Marchesiello, P., Nguyen, C., and Roblou, L.: Numerical modelling of hydraulic control, solitary waves and primary instabilities in the Strait of Gibraltar, Ocean Modell., 151, 101 642, https://doi.org/10.1016/j.ocemod.2020.101642, 2020.

Izquierdo, A. and Mikolajewicz, U.: The role of tides in the spreading of Mediterranean Outflow waters along the southwestern Iberian margin, Ocean Modell., 133, 27–43, https://doi.org/10.1016/j.ocemod.2018.08.003, 2019.

Lamy, A., Millot, C., and Molines, J. M.: Bottom Pressure and Sea Level Measurements in the Gulf of Lions, J. Phys. Oceanogr., 11, 394–409, https://doi.org/10.1175/1520-0485(1981)011<0394:BPASLM>2.0.CO;2, 1981.

Leder, N. and Orlić, M.: Fundamental Adriatic seiche recorded by current meters, Annales Geophysicae, 22, 1449–1464, 2004.

Lee, H.-C., Rosatib, A., and Spelman, M. J.: Barotropic tidal mixing effects in a coupled climate model: Oceanic conditions in the Northern Atlantic, Ocean Modell., 11, 464–477, https://doi.org/10.1016/j.ocemod.2005.03.003, 2006.

Li, Z. and von Storch, J.-S.: M2 internal-tide generation in STORMTIDE2, J. Geophys. Res. Oceans, 125, https://doi.org/10.1029/2019JC015453, 2020.

Li, Z., von Storch, J.-S., and Müller, M.: The M2 Internal Tide Simulated by a 1/10° OGCM, J. Phys. Oceanogr., 45, 3119 – 3135, https://doi.org/10.1175/JPO-D-14-0228.1, 2015.

Li, Z., von Storch, J.-S., and Müller, M.: The K1 internal tide simulated by a 1/10° OGCM, Ocean Modell., 113, 145–156, https://doi.org/10.1016/j.ocemod.2017.04.002, 2017.

Lozano, C. J. and Candela, J.: The M2 tide in the Mediterranean Sea: Dynamic analysis and data assimilation, Oceanol. Acta, 18, 419–441, 1995.

Madec, G., Bourdallé-Badie, R., Bell, M., Chanut, J., Clementi, E., Coward, A., Drudi, M., Éthé, C., Iovino, D., Lea, D., Lévy, C., Martin, N., Masson, S., Mathiot, P., Mocavero, S., Müller, S., Nurser, G., Samson, G., and Storkey, D.: NEMO ocean engine, https://doi.org/10.5281/zenodo.1464816, 2019.

Maderich, V., Ilyin, Y., and Lemeshko, E.: Seasonal and interannual variability of the water exchange in the Turkish Straits System estimated by modelling, Mediterr. Mar. Sci., 16, 444–459, https://doi.org/10.12681/mms.1103, 2015.

Medvedev, I. P., Vilibić, I., and Rabinovich, A. B.: Tidal Resonance in the Adriatic Sea: Observational Evidence, J. Geophys. Res. Oceans, 125, e2020JC016 168, https://doi.org/10.1029/2020JC016168, 2020.

Melet, A., Legg, S., and Hallberg, R.: Climatic Impacts of Parameterized Local and Remote Tidal Mixing, J. Clim., 29, 3473 – 3500, https://doi.org/10.1175/JCLI-D-15-0153.1, 2016.

Mihanović, H., Orlić, M., and Pasarić, Z.: Diurnal thermocline oscillations driven by tidal flow around an island in the Middle Adriatic, J. Marine Sys., 78, S157–S168, https://doi.org/10.1016/j.jmarsys.2009.01.021, 2009.

Morozov, E. G., Trulsen, K., Velarde, M. G., and Vlasenko, V. I.: Internal Tides in the Strait of Gibraltar, J. Phys. Oceanogr., 32, 3193 – 3206, https://doi.org/10.1175/1520-0485(2002)032<3193:ITITSO>2.0.CO;2, 2002.

Müller, M., Haak, H., Jungclaus, J., Sündermann, J., and Thomas, M.: The effect of ocean tides on a climate model simulation, Ocean Modell., 35, 304–313, https://doi.org/10.1016/j.ocemod.2010.09.001, 2010.

Naranjo, C., Lafuente, J., Sannino, G., and Sanchez-Garrido, J.: How much do tides affect the circulation of the Mediterranean Sea? From local processes in the Strait of Gibraltar to basin-scale effects, Progress Oceanogr., 127, 108–116, https://doi.org/j.pocean.2014.06.005, 2014.

Niwa, Y. and Hibiya, T.: Numerical study of the spatial distribution of the M2 internal tide in the Pacific Ocean, J. Geophys. Res. Oceans, 106, 22 441–22 449, https://doi.org/10.1029/2000JC000770, 2001.

Oddo, P., Bonaduce, A., Pinardi, N., and Guarnieri, A.: Sensitivity of the Mediterranean Sea level to atmospheric pressure and free surface elevation numerical formulation in NEMO, Geosci. Model Dev., 7, 3001–3015, https://doi.org/10.5194/gmd-7-3001-2014, 2014.

Oddo, P., Poulain, P., Falchetti, S., Storto, A., and Zappa, G.: Internal tides in the central Mediterranean Sea: observational evidence and numerical studies, Ocean Dyn., 73, 145–163, https://doi.org/10.1007/s10236-023-01545-z, 2023.

Pacanowski, R. C. and Philander, S. G. H.: Parameterization of Vertical Mixing in Numerical Models of Tropical Oceans, J. Phys. Oceanogr., 11, 1443–1451, https://doi.org/10.1175/1520-0485(1981)011<1443:POVMIN>2.0.CO;2, 1981.

Palma, M., Iacono, R., Sannino, G., Bargagli, A., Carillo, A., Fekete, B. M., Lombardi, E., Napolitano, E., Pisacane, G., and Struglia, M. V.: Short-term, linear, and non-linear local effects of the tides on the surface dynamics in a new, high-resolution model of the Mediterranean Sea circulation, Ocean Dyn., 70, 935–963, https://doi.org/10.1007/s10236-020-01364-6, 2020.

Pettenuzzo, D., Large, W., and Pinardi, N.: On the corrections of ERA-40 surface flux products consistent with the Mediterranean heat and water budgets and the connection between basin surface total heat flux and NAO, J. Geophys. Res., 115, https://doi.org/10.1029/2009JC005631, 2010.

Pinardi, N., Zavatarelli, M., Adani, M., Coppini, G., Fratianni, C., Oddo, P., Simoncelli, S., Tonani, M., Lyubartsev, V., Dobricic, S., and Bonaduce, A.: Mediterranean Sea large-scale low-frequency ocean variability and water mass formation rates from 1987 to 2007: A retrospective analysis, Prog. Oceanogr., 132, 318–332, https://doi.org/10.1016/j.pocean.2013.11.003, 2015.

Pinardi, N., Cessi, P., Borile, F., and Wolfe, C. L.: The Mediterranean sea overturning circulation, J. Phys. Oceanogr., 49, 1699–1721, https://doi.org/10.1175/JPO-D-18-0254.1, 2019.

Raicich, F.: On the fresh balance of the Adriatic Sea, J. Mar. Sys., 9, 305–319, https://doi.org/10.1016/S0924-7963(96)00042-5, 1996.

Sanchez-Roman, A., Jorda, G., Sannino, G., and Gomis, D.: Modelling study of transformations of the exchange flows along the Strait of Gibraltar, Ocean Sci., 14, 1547–1566, https://doi.org/10.5194/os-14-1547-2018, 2018.

Sannino, G., Sánchez Garrido, J. C., Liberti, L., and Pratt, L.: Exchange Flow through the Strait of Gibraltar as Simulated by a σ-Coordinate Hydrostatic Model and a z-Coordinate Nonhydrostatic Model, chap. 3, pp. 25–50, American Geophysical Union (AGU), https://doi.org/10.1002/9781118847572.ch3, 2014.

Schwab, D. J. and Rao, D. B.: Barotropic oscillations of the Mediterranean and Adriatic Seas, Tellus A, 35A, 417–427, https://doi.org/10.1111/j.1600-0870.1983.tb00216.x, 1983.

Shchepetkin, A. F. and McWilliams, J. C.: The regional oceanic modeling system (ROMS): a split-explicit, free-surface, topography-following-coordinate oceanic model, Ocean Modell., 9, 347–404, https://doi.org/10.1016/j.ocemod.2004.08.002, 2005.

Simmons, H. L., Jayne, S. R., St. Laurent, L. C., and Weaver, A. J.: Tidally driven mixing in a numerical model of the ocean general circulation, Ocean Modell., 6, 245–263, https://doi.org/10.1016/S1463-5003(03)00011-8, 2004.

St. Laurent, L. C., Simmons, H. L., and Jayne, S. R.: Estimating tidally driven mixing in the deep ocean, Geophys. Res. Lett., 29, 21–1–21–4, https://doi.org/10.1029/2002GL015633, 2002.

Sánchez-Román, A., García-Lafuente, J., Delgado, J., Sánchez-Garrido, J., and Naranjo, C.: Spatial and temporal variability of tidal flow in the Strait of Gibraltar, J. Mar. Syst., 98-99, 9–17, https://doi.org/10.1016/j.jmarsys.2012.02.011, 2012.

Tonani, M., Pinardi, N., Dobricic, S., Pujol, I., and Fratianni, C.: A high-resolution free-surface model of the Mediterranean Sea, Ocean Sci., 4, 1–14, https://doi.org/10.5194/os-4-1-2008, 2008.

van Haren, H., and The ANTARES Collaboration: High-frequency internal wave motions at the ANTARES site in the deep Western Mediterranean, Ocean Dyn,, 64, https://doi.org/10.1007/s10236-014-0702-0, 2014.

Vlasenko, V., Garrido, J. C. S., Stashchuk, N., Garcia-Lafuente, J., and Losada, M.: Three-Dimensional Evolution of Large-Amplitude Internal Waves in the Strait of Gibraltar, J. Phys. Oceanogr., 39, 2230 – 2246, https://doi.org/10.1175/2009JPO4007.1, 2009.

Vázquez, A., Stashchuk, N., Vlasenko, V., Bruno, M., Izquierdo, A., and Gallacher, P. C.: Evidence of multimodal structure of the baroclinic tide in the Strait of Gibraltar, Geophys. Res. Lett., 33, https://doi.org/10.1029/2006GL026806, 2006.

Chapter 4: Internal tides in the Mediterranean Sea

Abstract

A comprehensive high-resolution numerical study is carried out in order to understand where internal tides are generated, propagated, and dissipated within the Mediterranean Sea. Two ocean general circulation models were used for this: NEMO v3.6, and ICON-O, both hydrostatic ocean models based on primitive equations with Boussinesq approximation, where NEMO is a regional Mediterranean Sea model with an Atlantic box, and ICON a global model. It was found that internal tides are widespread in the Mediterranean Sea. Mapping the tidal barotropic to baroclinic energy conversion rate for the Mediterranean Sea reveals that the primary generation sites for internal tides are the Gibraltar Strait, the Sicily Strait/Malta Bank, and the Hellenic Arc. Semidiurnal internal tides can propagate for hundreds of kilometres from these generation sites into the Algerian Sea, Tyrrhenian Sea, and Ionian Sea respectively. Diurnal internal tides remain trapped along the bathymetry, and are generated in the central Mediterranean Sea and southeastern coasts of the basin. Two modes of the M2 semidiurnal internal tide and three modes of the K1 diurnal internal tide are resolved by the models. The models are also intercompared to investigate the differences between them in their representation of internal tides.

4.1 Introduction

Internal, or baroclinic, tides are internal waves at tidal frequencies, which are generated when barotropic tides interact with topography in the ocean, often at shelf breaks (Kelly and Lermusiaux, 2016), ocean ridges (Merrifield et al., 2001; Niwa and Hibiya, 2001), and in narrow straits (Morozov et al., 2002; Buijsman et al., 2014). These waves can dissipate close to their generation sites in the case of high mode internal tides, or propagate away for up to thousands of kilometres, in the case of low-mode, superinertial waves. Internal tides are responsible for around 1.0 TW of energy dissipation in the global ocean (Egbert and Ray, 2003), meaning that understanding their sites of generation, propagation, and energy dissipation is of great importance when detailing the energy budget of the global ocean. Internal tides also contribute to deep ocean mixing (Munk and Wunsch, 1998), so need to be correctly represented in numerical ocean general circulation models.

In many modern ocean general circulation models, the dissipation of energy from internal tides is represented with a parameterization of tidal mixing, commonly that of St. Laurent et al. (2002). However, these parameterizations only represent a fraction of the total internal tidal energy, that of high-mode internal tides which dissipate at their generation sites. The remaining energy, which relates to the low modes of superinertial internal tides, is propagated away and is not included in the energy budget of many numerical models. In the Mediterranean Sea, due to its latitude range of 30°N-46°N, diurnal internal tides have frequencies lower than the inertial frequency and remain trapped along the bathymetry, while semidiurnal internal tides are superinertial and are able to freely propagate away from their generation sites, so both the dissipation of internal tidal kinetic energy close to the generation site and wave propagation over long distances need to be considered in the model's mixing parameterizations.

In most of the Mediterranean Sea, the amplitude of barotropic tides is lower than in many other regions of the global ocean, except the Gibraltar Strait, Gulf of Gabes, and the North Adriatic Sea (Tsimplis et al., 1995; McDonagh et al., 2023). However, regional studies within the Mediterranean Sea such as Morozov et al. (2002), Oddo et al. (2023), and Alford et al. (2012) have indicated that internal tides are generated in several regions of

the Mediterranean Sea. These works suggest that a basin-wide study was needed.

The Gibraltar Strait is a region in which internal tides have been studied in more detail, through both observational and modelling methods. Morozov et al. (2002) found that semidiurnal vertical oscillations due to internal tide generation at the Camarinal Sill have amplitudes exceeding 200m, and that this energy causes turbulent mixing in the Gibraltar Strait. Internal tides in the Gibraltar Strait contribute to the bottom pressure (Candela et al., 1990), and propagate in both directions from the Camarinal Sill (Lafuente et al., 2000).

Studies such as Gasparini et al. (2004) and Oddo et al. (2023) investigated internal tides in the central Mediterranean Sea, finding that internal tides are generated over the complex topography in both the Sicily Strait (Gasparini et al., 2004), and Malta Bank (Oddo et al., 2023), affecting the dynamics in both regions. Other observational studies have been carried out in the Aegean Sea (Alford et al., 2012), where Doppler current profiles were used to identify propagating semidiurnal internal tides, and in the Mid-Adriatic (Mihanović et al., 2009), where potential trapped diurnal internal waves around islands were found. These studies have shown that internal tides are generated at several sites in the Mediterranean Sea, but research has often been limited by spatial and temporal availability of observational data, which comes mostly from cruises, and limited-area models. The propagation of internal tides in the whole Mediterranean Sea has not previously been investigated. A summary of the previously studied regions of internal tides within the Mediterranean is shown in Figure 4.1.

In other regions of the ocean, and for the global ocean in its entirety, numerical studies have proven to be valuable in understanding internal tides. Studies by Li et al. (2015, 2017) demonstrate the value of using a high-resolution general circulation ocean model to investigate internal tides in the global ocean. This is done through analysis of kinetic energy and stratification to find internal tide generation sites and propagation regions. Additionally, analysis of internal tide wavelengths and vertical structure modes are used to understand the limitations of the numerical models. Basin-wide studies of oceans and seas such as Niwa and Hibiya (2001) in the Pacific Ocean, and Kelly and Lermusiaux (2016) in the Atlantic Ocean show the importance of local topography in the generation of internal

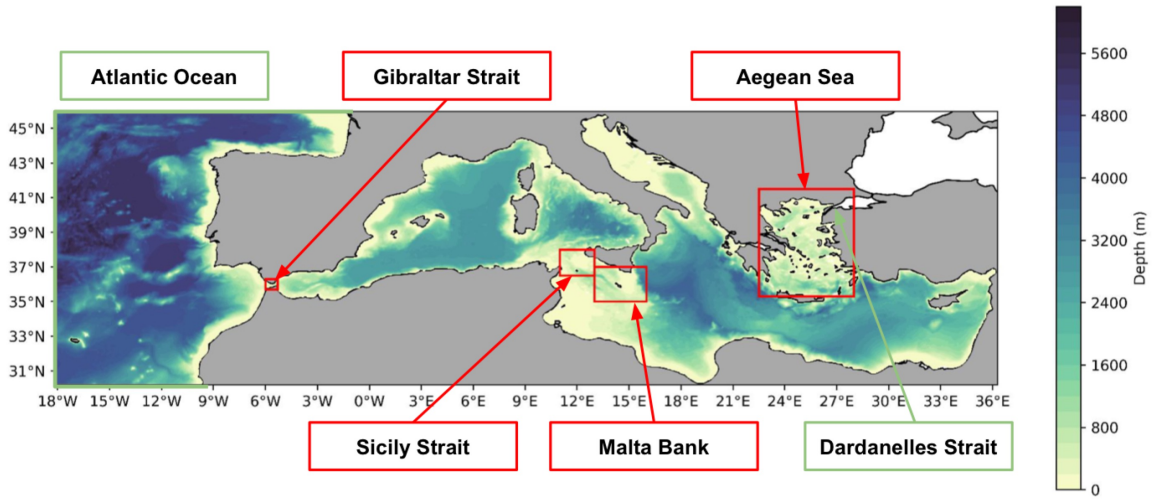

Figure 4.1: Map of NEMO model domain with model bathymetry in coloured contours. Lateral open boundary conditions of the NEMO configuration are in green. Key regions from previous literature for internal tides studies are highlighted in red boxes.

tides, and how this fits into the broader picture of internal tidal energy at a larger scale, such as interactions with the Gulf Stream. Internal tides also interact with mesoscale eddies, as discussed in Dunphy and Lamb (2014) and Guo et al. (2023), where eddies change the phase speeds and cause refraction of internal tides.

In this study, we carry out an analysis of numerical simulations to understand the dynamics of internal tides in the basin, with particular emphasis on finding generation sites, regions of semidiurnal internal tidal propagation, and the vertical modes of internal tides. Two ocean general circulation models are used, each with hourly outputs over a one-month period. Section 4.2 details the modelling framework, Section 4.3 contains results from the model outputs, Section 4.4 discusses the key differences between the two models, and Section 4.5 provides a conclusion. An intercomparison of barotropic tides in the models is available in Appendix C, and results for additional regions are shown in Appendix D.

4.2 Numerical models

4.2.1 NEMO

The implementation of version 3.6 of the general circulation ocean model NEMO (Madec et al., 1998) in the Mediterranean Sea is used (Clementi et al., 2021; Coppini et al., 2023). The model is described in detail in Chapters 2 and 3, and the implementation of the model follows that of those chapters, with the additional changes to the bathymetry and vertical mixing scheme from Chapter 4. The bathymetry used is that of Test 3 from Chapter 4.1, and the vertical mixing scheme follows that of the TKE3 experiment described in Chapter 4.2. These changes were the best-performing from their respective sets of sensitivity experiments.

The atmospheric forcing for the one-month period in 2022 analysed in this chapter starts from the $\frac{1}{10}^{\circ}$ and six-hour temporal resolution European Centre for Medium-Range Weather Forecasts (ECMWF) analyses for surface atmospheric variables. The model implementation is an extension of the TKE3 experiment from Chapter 4.2, and therefore has a significant spin-up period of more than seven years.

4.2.2 ICON-O

To provide a robust numerical analysis of internal tides in the Mediterranean Sea, a second dataset, derived from a global scale implementation of the ICON-O (Korn et al., 2022) primitive equations general circulation model, is used.

ICON-O uses an icosahedral grid, which splits the Earth's surface initially into twenty equilateral triangles, and then bisects these triangles further for higher resolution simulations, resulting in so-called R2Bn resolutions, where n is the number of times that the original icosahedron is bisected (Giorgetta et al., 2018). The simulation of ICON-O used in this work has a resolution of R2B9, meaning that the initial grid is divided nine further times, which is approximately equivalent to a horizontal resolution of 5km when interpolated onto a regular latitude-longitude grid. This resolution is slightly lower than, but compa-

rable to, NEMO's $\frac{1}{24}^{\circ}$ horizontal resolution in the Mediterranean Sea. ICON-O has 128 z* vertical levels without partial cells at the bottom, and uses the SRTM30 bathymetry (Becker et al., 2009) interpolated onto the model grid. Narrow straits (Gibraltar, Dardanelles, and Bosphorus in the Mediterranean/Black Sea region) are manually checked to ensure that they are open, but no further modifications are made. The Black Sea is included in the ICON model, so no boundary condition is required here. However, the Black Sea is not analysed in this work, since it is not included in the NEMO configuration used.

The world's fifty largest rivers are included in the configuration (Gates et al., 1993), including four that flow into the Mediterranean Sea: the Ebro, Nile, Po, and Rhône. These use flux values from the daily climatology by Röske (2006). Atmospheric forcing is from ERA5 (Hersbach et al., 2023) with a temporal frequency of one hour, at a resolution of 30km interpolated onto the model grid.

Tides are included in ICON-O via a lunisolar term in the momentum equation, which is the horizontal component of the difference between the gravitational forces of the Sun and Moon and the centrifugal force due to the rotation of the Earth (Logemann et al., 2021). This term provides the full tidal potential and means that explicit tidal forcing, as used in NEMO, is not necessary, and ICON-O includes all tidal components. The accuracy of tides in ICON at lower resolutions (R2B6 to R2B8) was assessed in von Storch et al. (2023).

Vertical mixing in ICON uses a TKE scheme also based on Gaspar et al. (1990), and has a similar configuration to NEMO for this parameterization. The model uses further parameterizations of secondary tidal processes: topographic wave drag, and self-attraction and loading, which are not included in the NEMO configuration. Some of the key differences between the two experiments are summarised in Table 4.1.

One month (March 2022) of data is analysed for each model, with hourly outputs of three-dimensional currents, temperature, salinity, Brunt-Väisälä frequency, and two-dimensional sea surface height.

Model component	NEMO	ICON
Region	Mediterranean Sea with Atlantic Box	Global
Grid	Rectangular latitude-longitude	Icosahedral
Horizontal resolution	$\frac{1}{24}^\circ$ (3.8km)	R2B9 (around 5km)
Vertical resolution	141 z* levels with partial cells	128 z* levels without partial cells
Tides	8 tidal components (M2, S2, K1, O1, N2, Q1, K2, P1) forced at the boundary	Full lunisolar tidal potential
Secondary tidal processes	None	Topographic wave drag and self attraction and loading
Rivers	39 rivers from climatology	4 Mediterranean rivers from climatology
Bathymetry	GEBCO (30")	SRTM30 (30")

Table 4.1: Comparison of some key features of the NEMO and ICON implementations used in this work.

4.3 Results

4.3.1 Kinetic energy

A harmonic analysis of the three-dimensional horizontal currents is first carried out in order to isolate tidal kinetic energy for each component. From this, a vertical mean is removed to calculate the baroclinic component of this as the internal tide kinetic energy for a single layer. Maps of vertical mean baroclinic kinetic energy of the M2 and K1 tidal components in the NEMO and ICON experiments are shown in Figure 4.2. These maps highlight potential generation sites for internal tides in a variety of regions in the Mediterranean Sea.

The vertical mean baroclinic kinetic energy of the M2 component is similar in the two model implementations. The regions with the highest baroclinic kinetic energy through the water column are similar to those identified in previous work, e.g. Morozov et al. (2002); Gasparini et al. (2004); Alford et al. (2012): the Gibraltar Strait, Sicily Channel, and Aegean Sea. Moreover, this analysis highlights sites of internal tide generation or

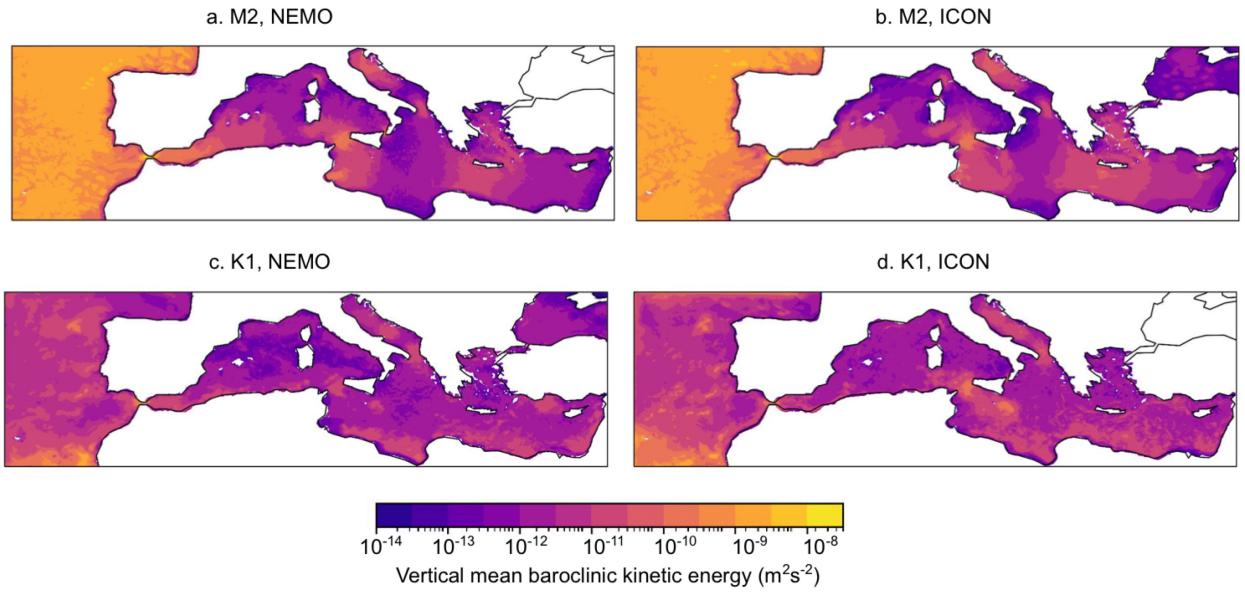

Figure 4.2: Vertical mean baroclinic kinetic energy in the Mediterranean Sea during March 2022, for the M2 component in a. NEMO and b. ICON and for the K1 component in c. NEMO and d. ICON.

propagation that were not mentioned in previous literature: the northern Adriatic Sea and the Cretan Passage. The K1 tidal component has a different distribution of baroclinic kinetic energy, with particularly high kinetic energy in NEMO in the southern Adriatic Sea and the Malta Bank (as discussed in Oddo et al. (2023)), as well as along the African coast in the south-east of the basin. The K1 baroclinic kinetic energy is weaker in NEMO than in the ICON experiment, but appears in broadly similar regions in the two models. The K1 internal tide is bottom-trapped rather than freely propagating at mid-latitudes (Nakamura et al., 2000; Li et al., 2017), so it is unsurprising to see the K1 baroclinic kinetic energy concentrated on the steep bathymetry of the eastern Mediterranean coasts.

In order to better visualise the propagation of internal tides in the Mediterranean Sea, the kinetic energy is also evaluated in Figure 4.2, considering the separate zonal and meridional components of the current at specific depths. Figure 4.3 shows the baroclinic M2 currents at the vertical level closest to 150m in each model. In both models, the propagation of internal tides is visible in the western Mediterranean inflowing current inside the Gibraltar Strait. This current typically flows from the Gibraltar Strait along the north African coast at depths of 0-150m, which has particularly clear wave structures in the baroclinic

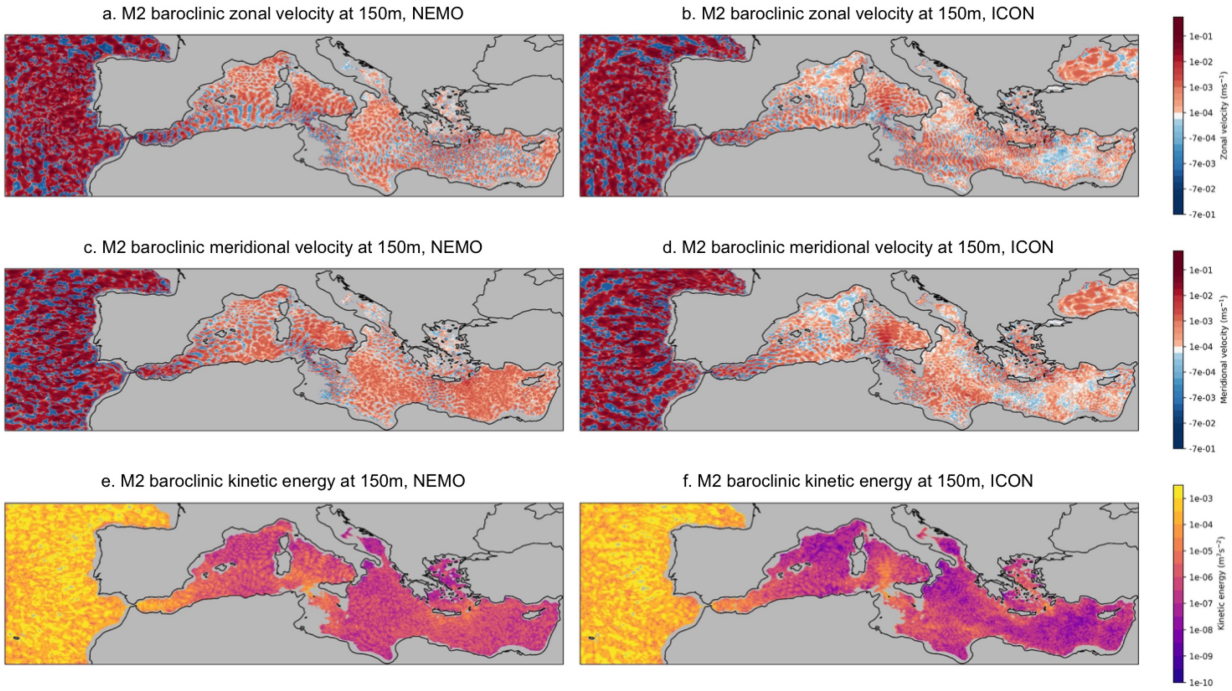

Figure 4.3: Maps of baroclinic M2 current amplitude at the closest vertical level to 150m for a. zonal velocity component in NEMO, b. zonal velocity component in ICON, c. meridional velocity component in NEMO, d. meridional velocity component in ICON, e. kinetic energy in NEMO, and f. kinetic energy in ICON.

zonal velocity (Figures 4.3a and b). The waves are also seen in the Tyrrhenian Sea, and in several regions of the eastern Mediterranean, most notably to the west of Crete. There are some key differences between the two experiments: the NEMO experiment shows higher kinetic energy in the western Mediterranean whereas the ICON experiment has more kinetic energy in the Tyrrhenian Sea, but the regions showing propagating wave structures are broadly similar in the two models.

These waves at the M2 frequency are also visible at deeper layers: Figure 4.4 shows the same currents at 300m and Figure 4.5 at 1000m. At 300m, the kinetic energy is lower than at 150m, but the internal tides are still apparent in the same regions. However, at around 1000m, the structures begin to break down. Since the Sicily Strait is shallower than 1000m at its deepest point, the Mediterranean is split into eastern and western basins, and internal tides are unable to propagate across. In the deeper layers of Figures 4.4 and 4.5, we see an emergence of baroclinic kinetic energy at the M2 frequency in the Hellenic Arc region, a steep topographic feature between the deep eastern Mediterranean and shallow Aegean

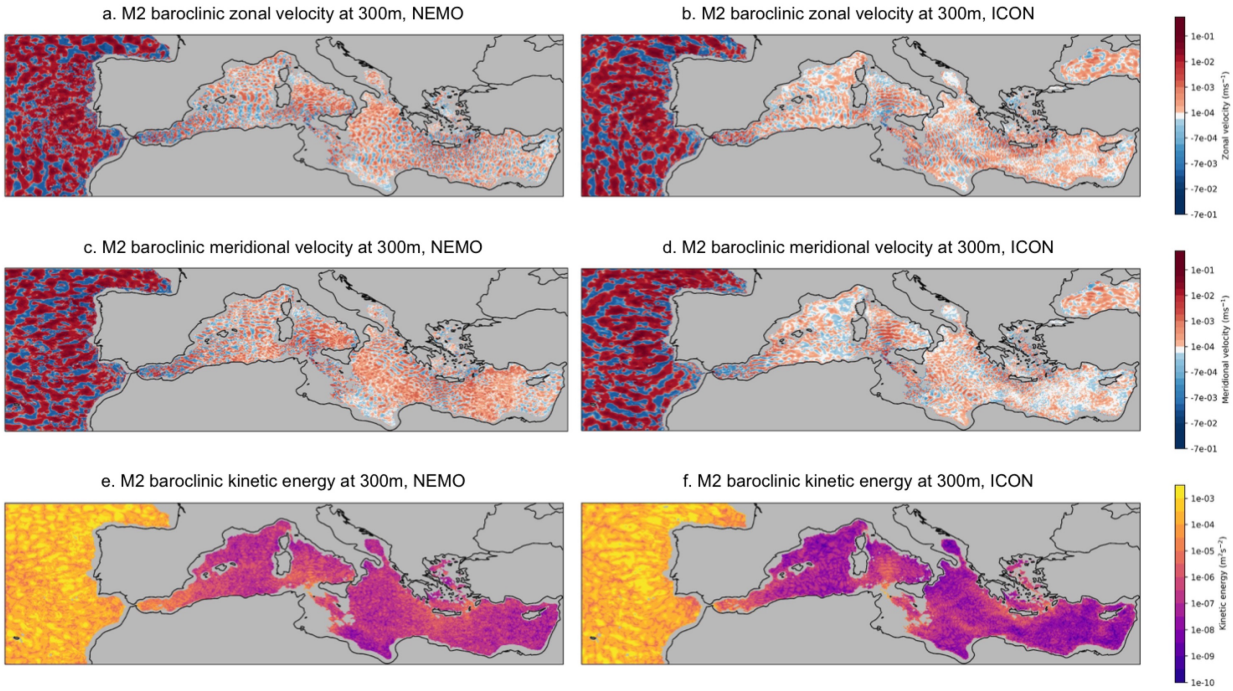

Figure 4.4: Maps of baroclinic M2 current amplitude at the closest vertical level to 300m for a. zonal velocity component in NEMO, b. zonal velocity component in ICON, c. meridional velocity component in NEMO, d. meridional velocity component in ICON, e. kinetic energy in NEMO, and f. kinetic energy in ICON.

Sea. This has not been described before as a site for potential internal tide generation in the eastern Mediterranean Sea, and explains the wave propagation found in the Ionian Sea.

Rotary spectra of the baroclinic kinetic energy throughout the water column are plotted in several key points. These are the centres of the points in Figure 4.1, as well as in four further regions, which appear to have internal tide propagation in the maps of Figures 4.3-4.5. These are the Algerian Sea (37.70°N, 5.23°E), the Tyrrhenian Sea (39.73°N, 11.50°E), and two points in the Ionian Sea (35.90°N, 20.46°E and 33.50°N, 19.48°E), which are the centre points of regions shown in Figure 4.8. Three of these eight spectra are shown in Figure 4.6 – the Gibraltar Strait, Sicily Strait, and northern Ionian Sea – while the others can be found in Appendix D. Chapter 2.5 contains a description of the calculation of the rotary spectrum and more information on its use.

In the Gibraltar Strait (Figure 4.6 a-b), we see baroclinic kinetic energy at both diurnal and semidiurnal frequencies throughout the whole depth. This can also be split into clockwise

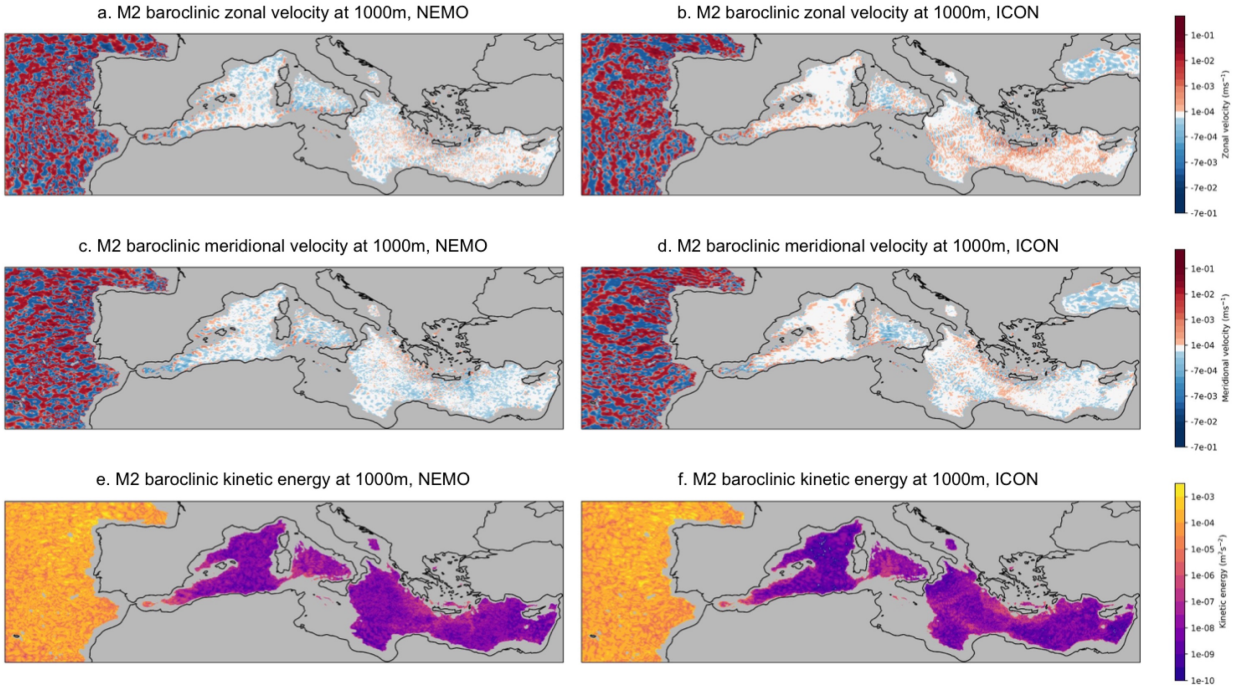

Figure 4.5: Maps of baroclinic M2 current amplitude at the closest vertical level to 1000m for a. zonal velocity component in NEMO, b. zonal velocity component in ICON, c. meridional velocity component in NEMO, d. meridional velocity component in ICON, e. kinetic energy in NEMO, and f. kinetic energy in ICON.

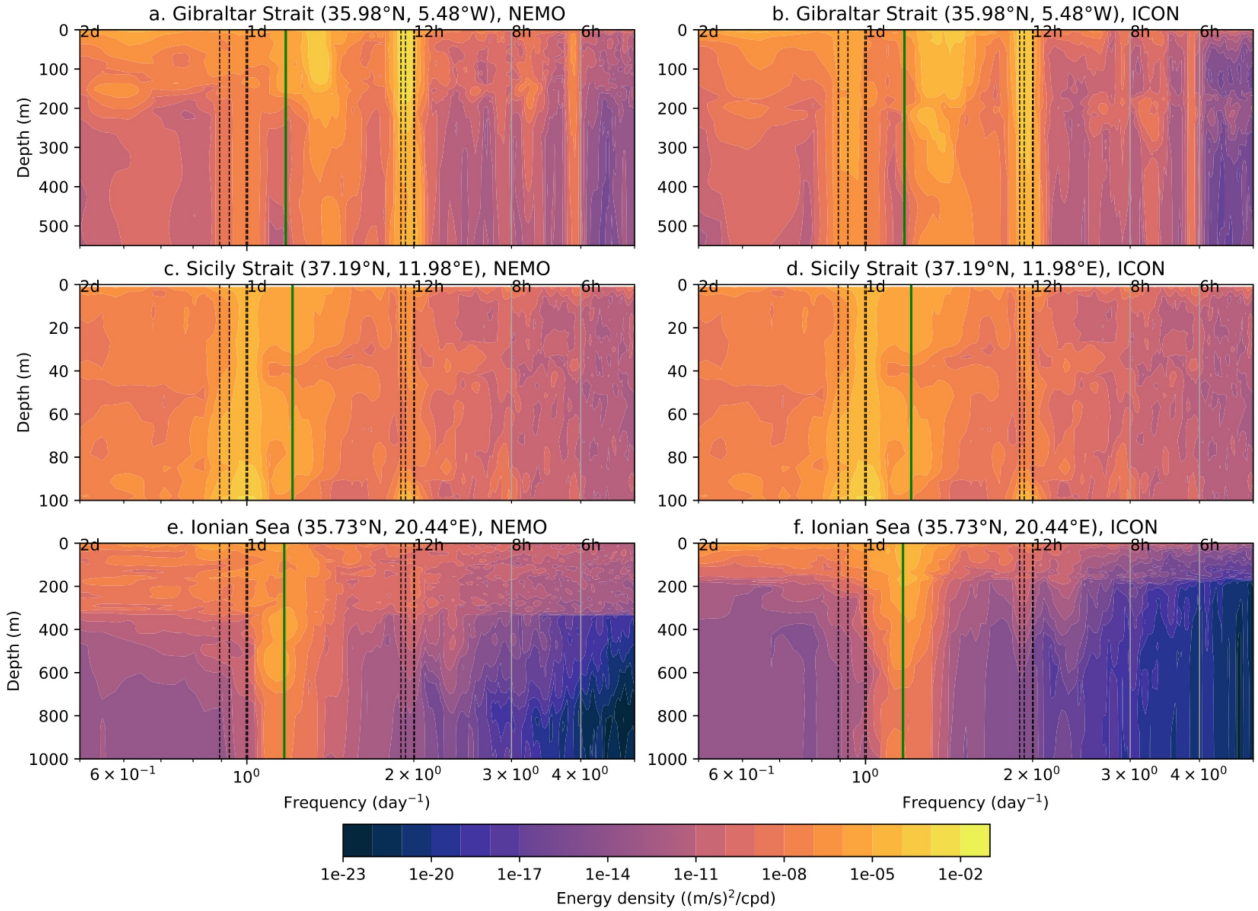

Figure 4.6: Rotary spectra of combined clockwise and counterclockwise baroclinic horizontal currents at three points: the Gibraltar Strait (35.98°N, 5.48°W) (a-b), Sicily Strait (37.19°N, 11.98°E) (c-d), and Ionian Sea (35.73°N, 20.44°E) (e-f), evaluated from NEMO (left) and ICON (right) model simulations through the vertical column. Dashed black lines represent the tidal frequencies included in NEMO and the green line indicates the inertial frequency at the latitude of the point.

and counterclockwise components, as in Figure 4.7, where we see the emergence of kinetic energy from the clockwise component in the upper (incoming) layer and counterclockwise in the lower (outflowing) layer, features which are particularly prominent in NEMO.

In the Sicily Strait (Figure 4.6 c-d), the bottom-trapped diurnal internal tide is more prominent, while there is only a small amount of semidiurnal baroclinic kinetic energy close to the surface: demonstrating further the result of Figure 4.2, which showed that the M2 internal tide is relatively important in the western basin, while K1 is more prominent in the central Mediterranean Sea. Contrastingly, in the Ionian Sea (Figures 4.6 e-f), baroclinic kinetic energy depends strongly on depth, with some semidiurnal baroclinic kinetic

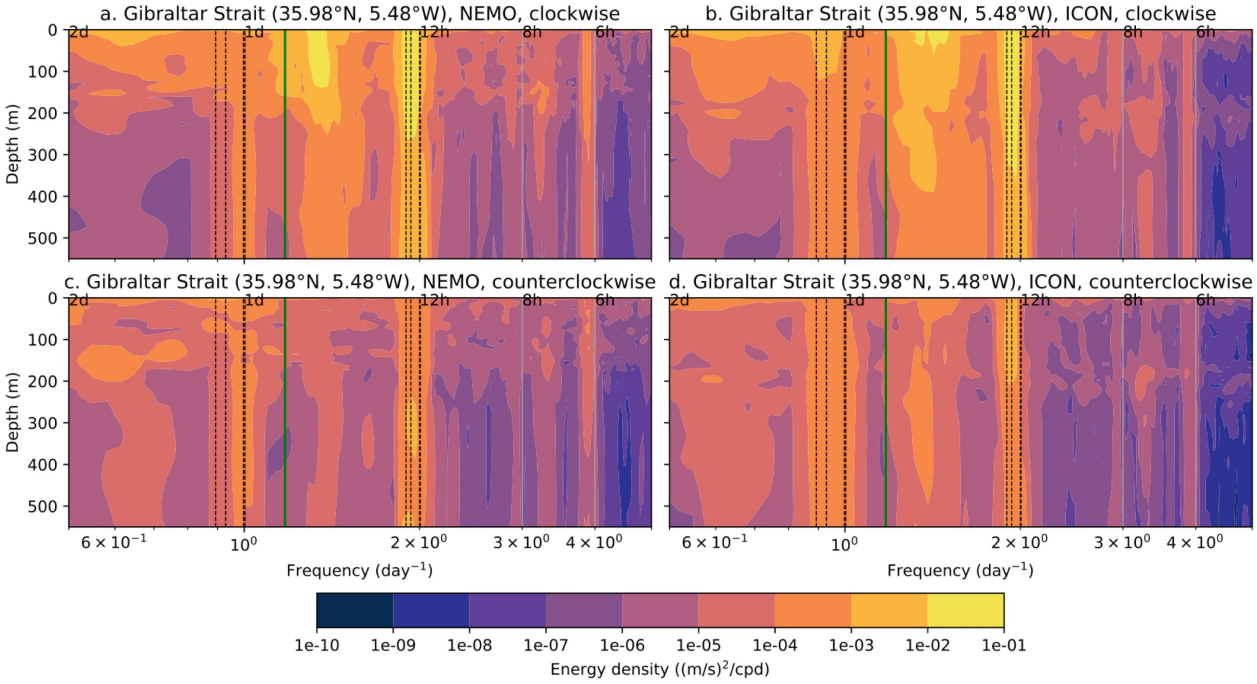

Figure 4.7: Rotary spectra of baroclinic horizontal currents in the Gibraltar Strait (35.98°N, 5.48°W), as in Figure 4.6 a-b, but shown here for separate clockwise (a-b) and counterclockwise (c-d) components, for NEMO (left) and ICON (right). Dashed black lines represent the tidal frequencies included in NEMO and the green line indicates the inertial frequency at the latitude of the point.

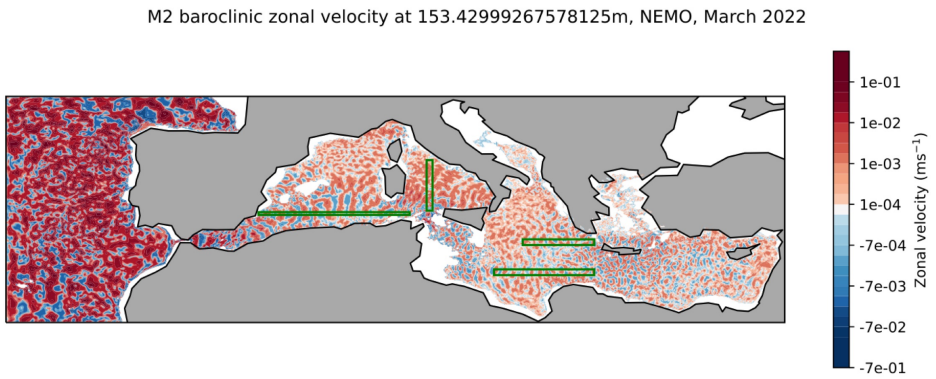

Figure 4.8: Map of M2 baroclinic zonal velocity for NEMO at 150m (as in Figure 4.3a), with regions for wavenumber analysis marked in green boxes.

energy in the upper layers. As discussed in Chapter 3, this region shows some interaction between the diurnal internal tide and near-inertial waves, particularly in NEMO, where the near-inertial peaks at 400-600m stretch toward the diurnal frequency. This analysis of the baroclinic kinetic energy further confirms that the wave-wave interactions seen in Chapter 3 refer to interactions between internal tides and near-inertial waves.

4.3.2 Wavenumber spectra

Typical wavelengths of the first two modes of the M2 internal tide in the global ocean are 100-160km and 45-80km (Li et al., 2015), and typical wavelengths for the first three modes of the K1 internal tide are 200-400km, 100-200km, and 60-120km (Li et al., 2017). Several regions are chosen for wavenumber analysis, following propagation paths of the M2 internal tide seen in Figures 4.3-4.5. Figure 4.8 shows a map of these new analysis regions.

Wavenumber spectra of the tidal baroclinic velocity of the M2 and K1 components are calculated along these paths using the periodogram as described in Chapter 2.5. These spectra are calculated along the physical path of the wave rather than over time, so the x-axis represents the number of wavelengths per kilometre rather than the number of cycles per day (as in previous spectra). The data used to calculate the periodogram is from the harmonic analysis of currents for each tidal component, along the length of the paths of

Figure 4.8. Several parallel lines (five for the Algerian Sea, ten for the other regions) are averaged after the periodogram is calculated for each line.

The wavenumber spectra for the M2 and K1 components respectively along each of these paths are in Figures 4.9 and 4.10. In Figure 4.9, the largest density peak in many regions are at wavelengths greater than 200km. These can be attributed to seiches in the Mediterranean Sea, which include modes at frequencies close to that of the M2 tidal component, at 11.4 hours and 12 hours (Schwab and Rao, 1983; Lozano and Candela, 1995) (see Chapter 3). The peak most relevant to internal tides is at around 100km and is visible in the Algerian Sea and Ionian Sea, in both experiments but most prominently NEMO. This is the first vertical mode of the M2 internal tide. A second mode also appears in Figure 4.9 a, c, e, and f, at a deeper level and higher wavenumber than the first.

For the K1 internal tide (Figure 4.10), vertical modes have longer wavelengths, and there are not any known seiches in the Mediterranean Sea close to the K1 tidal frequency of one day. This means that internal tide modes are more straightforward to distinguish, and the models can resolve more modes due to the longer wavelengths. Figure 4.10 shows multiple resolved modes of the diurnal internal tide in several regions (Figs. 4.10 e, f, g, h), close to the typical wavelengths from Li et al. (2017), demonstrating the presence of the K1 internal tide in many parts of the Mediterranean Sea. The signal is lacking in the Algerian Sea and Tyrrhenian Sea, particularly in NEMO, suggesting that the western basin is dominated instead by the incoming semidiurnal internal tide through the Gibraltar Strait.

4.3.3 Energy available for internal tides

The conversion of barotropic tidal energy to baroclinic energy for internal tide generation can be calculated for the Mediterranean Sea as an estimate of the energy available for internal tide generation, according to Li and von Storch (2020). This conversion, C, formally represents the internal tide generation through both the bottom form drag and the surface form drag. However, the contribution of the surface form drag is negligible compared to the bottom form drag, so here the bottom form drag term is the only one used. This is still

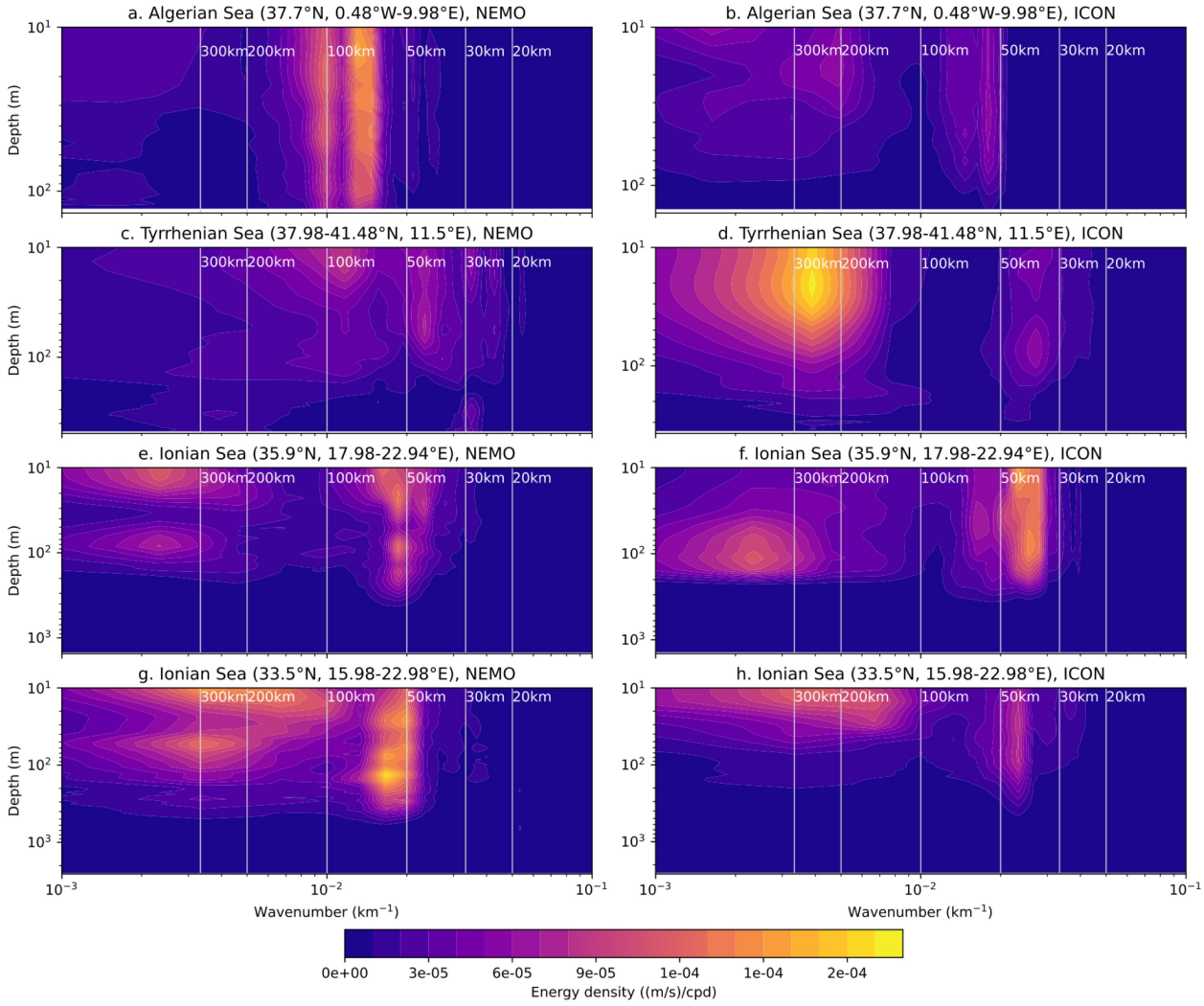

Figure 4.9: Wavenumber energy density spectra of M2 baroclinic currents for four regions (as in Figure 4.8): a-b. Zonal velocity, Algerian Sea, NEMO and ICON, c-d. Meridional velocity, Tyrrhenian Sea, NEMO and ICON, e-f. Zonal velocity, Ionian Sea (north), NEMO and ICON, g-h. Zonal velocity, Ionian Sea (south), NEMO and ICON.

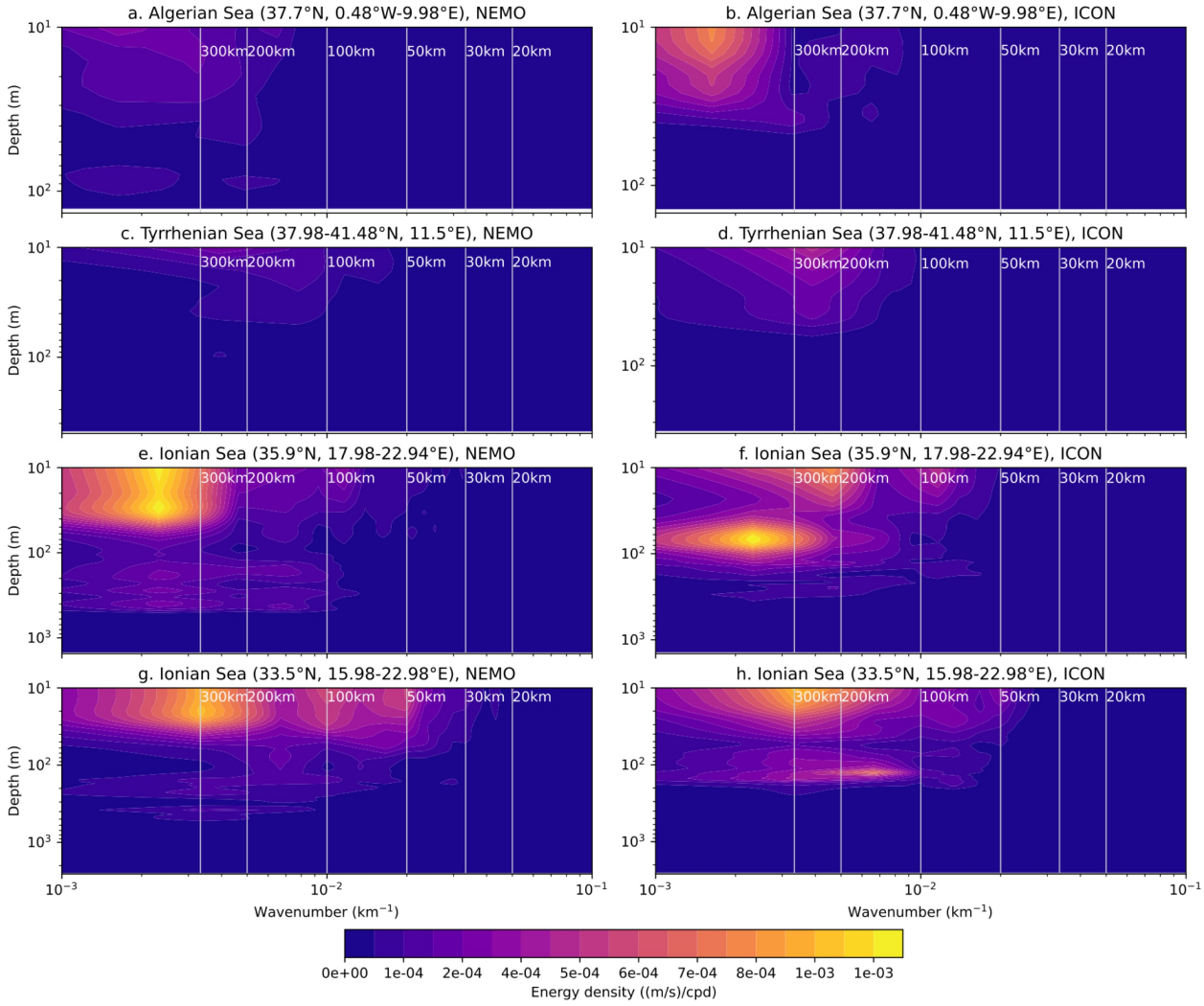

Figure 4.10: Wavenumber energy density spectra of K1 baroclinic currents for four regions (as in Figure 4.8): a-b. Zonal velocity, Algerian Sea, NEMO and ICON, c-d. Meridional velocity, Tyrrhenian Sea, NEMO and ICON, e-f. Zonal velocity, Ionian Sea (north), NEMO and ICON, g-h. Zonal velocity, Ionian Sea (south), NEMO and ICON.

considered to be a good approximation of C. C is defined as:

$$C = \int_{-d}^{\eta} g\rho' W \, dz \tag{4.1}$$

where ρ' is the density perturbation induced by wave motions, W is the tidal vertical velocity, η is the sea surface height, and d is the depth of the ocean. W was extracted from the vertical velocity using:

$$\frac{\partial U}{\partial x} + \frac{\partial V}{\partial y} + \frac{\partial W}{\partial z} = 0 \tag{4.2}$$

where U and V are the barotropic tidal velocities. This means that W is a linear function of z, since U and V are not dependent on z.

The value for ρ' is derived from the temperature and salinity data over the analysis period, which were initially used to calculate the full density ρ. This full density is then decomposed into:

$$\rho(x, y, z, t) = \rho_0 + \rho_b(x, y, z) + \rho'(x, y, z, t) \tag{4.3}$$

where ρ_0 is the constant reference density, and ρ_b is the background time-mean density averaged at each grid point, meaning that $\rho_0 + \rho_b$ is the total background mean density. The time-varying density ρ' is the remaining component of ρ. In practical terms, ρ' is obtained by subtracting the time-mean density from the full density ρ.

Once C is calculated using the values of U and V for each of the eight tidal components included in the NEMO experiment, it is summed to find a total value for C. The positive value of C means that barotropic energy is converted to baroclinic energy which is available for the generation of internal tides. Figure 4.11 shows a map of C for the Mediterranean Sea in the two experiments. These maps further confirm and quantify the generation sites of internal tides, which were already shown to an extent through baroclinic kinetic energy in Figure 4.2.

Barotropic energy is being converted to baroclinic energy for internal tide generation in

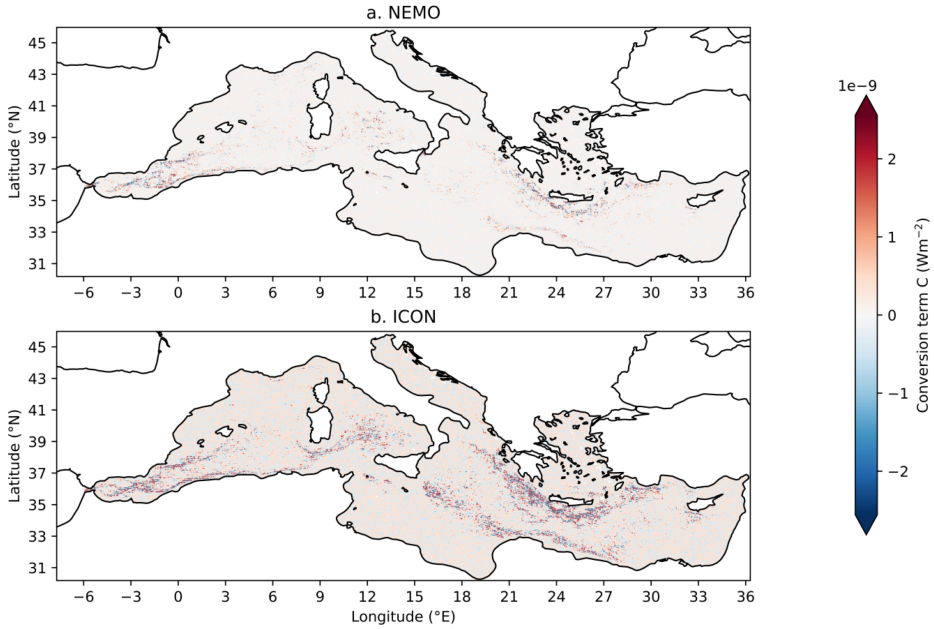

Figure 4.11: Maps of the barotropic to baroclinic energy conversion term (C) in the Mediterranean Sea, for a. NEMO, and b. ICON.

a wide variety of regions, most notably in the Gibraltar Strait/Alboran Sea, Tyrrhenian Sea, the Cretan Seas, Sicily Strait, Malta Bank (particularly in ICON), Ionian Sea, and in the eastern Mediterranean Sea more generally. Looking at these regions more closely in Figure 4.12, with reference to the bathymetry maps in Figures 4.1 and 4.16, we can see that the narrow and steep Gibraltar Strait (Figure 4.12 a, d) is a major generator of kinetic energy, where tidal velocity is high. The narrow passage in the Sicily Strait and the steepest slope in the Malta Bank regions (Figure 4.12 b, e) are the next most significant regions for generation of kinetic energy, with large values of the conversion term C particularly widespread in the ICON experiment. The higher values of C in ICON in the Malta Bank likely come from the stronger baroclinic K1 kinetic energy seen in Figure 4.2. Finally, the Hellenic Arc (Figure 4.12 c, f), where the deeper Ionian and Levantine Seas meet the shallow Aegean Sea, also has large values of C, and this provides a map of the specific generation region that could explain the propagating wave patterns seen in the Ionian Sea in the baroclinic kinetic energy maps in Figures 4.3-4.5.

It should be noted that there are some negative values in the results for C at the regions of internal tide generation. This is a known problem when calculating C (Li and von Storch,

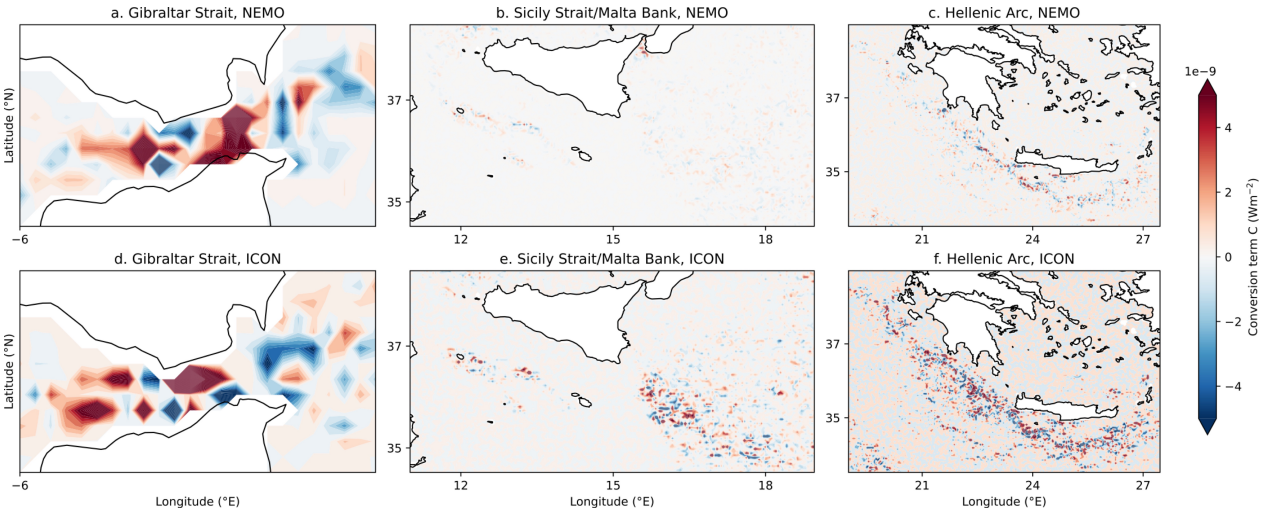

Figure 4.12: Maps of the barotropic to baroclinic energy conversion term (C) in key regions of the Mediterranean Sea: the Gibraltar Strait/Alboran Sea (a, d), the Sicily Strait/Malta Bank (b, e), and the Hellenic Arc region (c, f).

2020), since internal tides generated at a site may interfere with the propagation paths of internal tides generated elsewhere. This can cause ρ' and W to become out of phase which leads to negative values of C. In the global ocean, Li and von Storch (2020) found that C is a good estimate for the barotropic to baroclinic energy conversion, but the same has not been directly assessed for a semi-enclosed basin such as the Mediterranean Sea, where the problem of interference could be greater.

We can quantify internal tide generation by taking an area-weighted mean over each of the regions, although the aforementioned caveats should be considered. To account for the problem of negative values due to interference, only points with positive values are included in the calculation. The area-weighted mean values of the regions in Figure 4.12 are in Table 4.2. Although the highest mean values are in the Gibraltar Strait, the maximum values of C in both experiments are in the Hellenic Arc. In all regions, the maximum values are much larger than the mean values: the maximum values are shown since the mean values are highly sensitive to region selection.

	Mean (Wm^{-2})		Maximum (Wm^{-2})	
	NEMO	**ICON**	**NEMO**	**ICON**
Mediterranean Sea	1.781×10^{-10}	4.108×10^{-10}	2.821×10^{-8}	5.410×10^{-8}
Gibraltar Strait	1.552×10^{-9}	1.629×10^{-9}	1.963×10^{-8}	3.931×10^{-8}
Sicily Strait/Malta Bank	1.277×10^{-10}	3.447×10^{-10}	7.734×10^{-9}	2.868×10^{-8}
Hellenic Arc	2.948×10^{-10}	8.535×10^{-10}	2.821×10^{-8}	5.410×10^{-8}

Table 4.2: Area-weighted mean and maximum values for C within the regions of Figure 4.12, in Wm^{-2}.

4.4 Assessment of model differences

The two models broadly show internal tide generation and propagation in the same regions of the Mediterranean Sea. However, although they are similar in resolution and have some common features (see Section 4.2), the models show several differences in their representation of internal tides, particularly in the wavenumber analysis (see Figures 4.9 and 4.10). There are several possible reasons for this, including the differences in the implementation of barotropic tides. An intercomparison of barotropic tides between the two models is shown in the figures in Appendix C. Internal tide generation and propagation is mainly affected by the stratification and bathymetry of the models.

It is expected that models with a more stratified ocean would be more likely to have larger internal tidal propagation. The energy per unit volume in a propagating internal tide at the semidiurnal frequency, E_f according to Baines (1982) and Green et al. (2010), is:

$$E_f = 0.5\rho_0(u' + w' + N^2\eta^2) \tag{4.4}$$

where ρ_0 is the constant reference density, u' and w' are perturbation velocities in the horizontal and vertical directions respectively, N is the Brunt-Väisälä frequency, and η is the displacement of a streamline.

Figure 13 shows profiles of the squared Brunt-Väisälä frequency, both as a Mediterranean Sea average and for some of the key regions discussed in previous sections. We see that for the basin mean profile (Fig. 4.13a), the water column provided by the ICON simula-

tion is more stratified than that of NEMO across all vertical levels. This explains the larger kinetic energy and longer wave propagation seen at many depths such as in Figure 4.4 in the Eastern Mediterranean. The shape of the two profiles also differs: the profile from the ICON simulation has a second peak at around 1750m, while the NEMO experiment profile only has a subsurface peak. A Mediterranean Sea observed profile such as those in Cuypers et al. (2012) typically looks more like that of the NEMO experiment, with only one peak close to the surface, whereas the ICON experiment's profile has a double peak which appears more like a typical Atlantic Ocean profile such as those from Emery et al. (1984). This demonstrates that the internal tides may be overestimated by the ICON simulation in the Mediterranean Sea, due to high stratification. In other regions, we see that the ICON experiment has a generally more stratified profile than the NEMO experiment in several key regions for internal tide generation and propagation. There are some regions (Gibraltar Strait, Malta Bank, Algerian Sea, Ionian Sea) where the profile from the ICON simulation has higher stratification both close to the surface and in the deeper levels, with an intermediate layer where the NEMO experiment profile is more stratified, below 500m in most regions. However, since most of the internal tide propagation in the Mediterranean Sea occurs in the intermediate layers rather than in the abyssal layers, the upper 500m of the regions from Figure 4.13 are shown in Figure 4.14, where ICON has a higher stratification. We see that in Figure 4.12 e-f that ICON has greater internal tide generation in several regions, particularly at the Malta Bank and in the Hellenic Arc, compared to the NEMO experiment. It should be noted that the lack of vertical resolution at deeper levels in both experiments could be a hindrance to the generation and propagation of internal tides below 500m in the models.

The generation of internal tides is sensitive to changes in bathymetry, since internal tides are generated along the topography. The model bathymetry, as described in Table 4.1, comes from different sources in each experiment, and although they have the same resolution (30 arc-seconds), it is interpolated differently in each model due to the differing model horizontal grids. These bathymetry variations, although they are usually small, could impact the generation regions of internal tides, and therefore their energy and direction of propagation. Figure 4.15 shows the bathymetry differences between the two models. It is clear that although the differences in bathymetry are not large in most of the domain, the

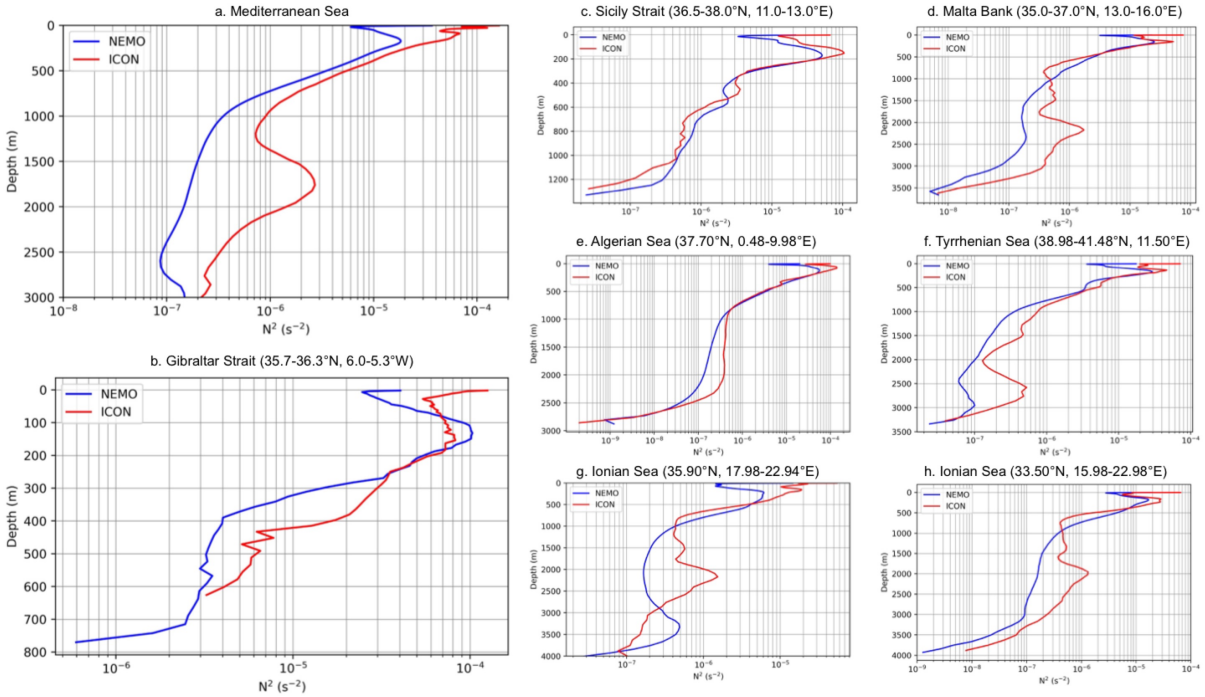

Figure 4.13: Vertical profiles of the Brunt Väisälä frequency for the NEMO simulation (blue) and the ICON simulation (red), for a. the Mediterranean Sea, and the regions indicated in Figures 4.1 and 4.8. These are b. the Gibraltar Strait, c. Sicily Strait, d. Malta Bank, e. Algerian Sea, f. Tyrrhenian Sea, g. Ionian Sea (north), and h. Ionian Sea (south).

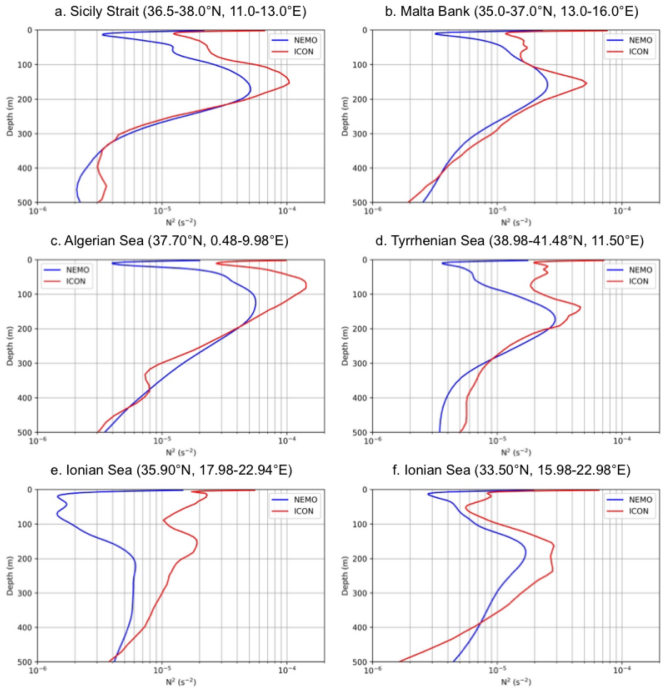

Figure 4.14: Vertical profiles of the Brunt Väisälä frequency for NEMO (blue) and ICON (red), for regions in a. Sicily Strait, b. Malta Bank, c. Algerian Sea, d. Tyrrhenian Sea, e. Ionian Sea (north), and f. Ionian Sea (south). The Gibraltar Strait is not shown here, since its full depth is already shown in Figure 4.13.

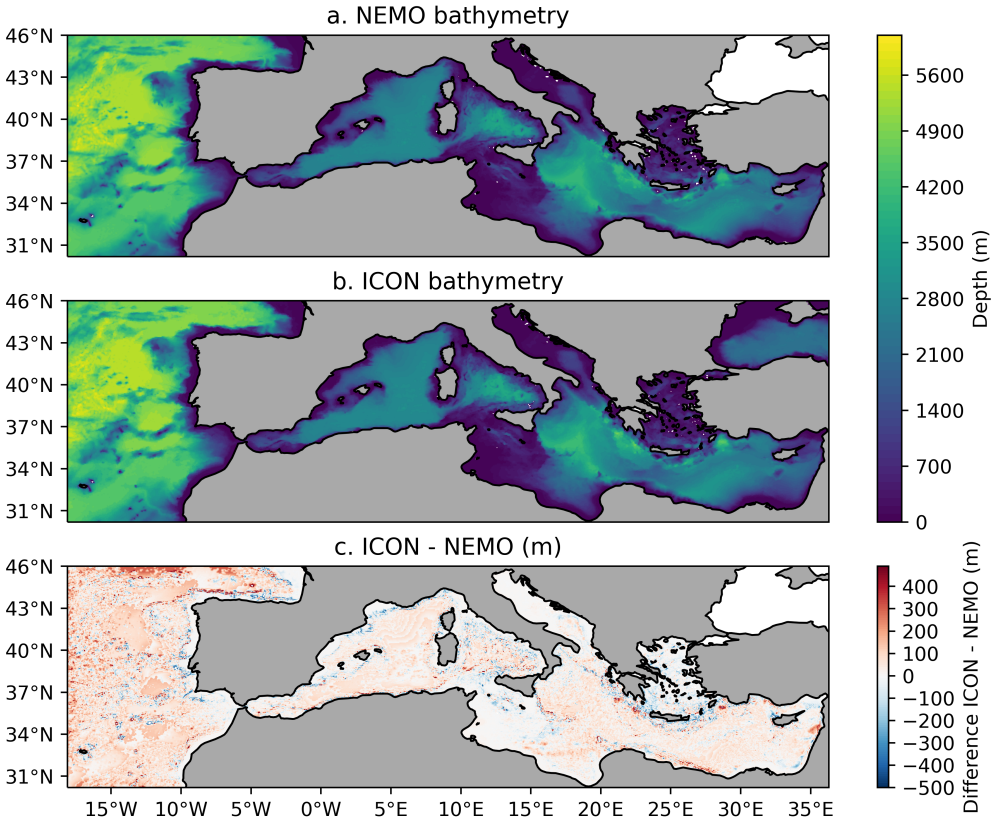

Figure 4.15: Model bathymetry for a. NEMO, b. ICON, and c. Difference (ICON - NEMO).

ICON bathymetry is slightly deeper than that of NEMO in many areas. However, in Figure 4.16, we can see that this is not the case in some key regions. In the narrowest part of the Gibraltar Strait, the most important region in the Mediterranean Sea for internal tide generation, the bathymetry is deeper in the NEMO implementation than it is in that of ICON. This is likely to affect the generation of internal tides and their propagation throughout the western Mediterranean basin. Another key bathymetry difference is in the Malta Bank (Figure 4.16h): in the ICON implementation the bathymetry is steeper and placed differently in comparison to the NEMO experiment, and the Ionian Sea is deeper while the Sicily Strait passage is shallower in the ICON experiment compared to that of NEMO. Finally, the deeper Ionian Sea also affects the Hellenic Arc region (Figure 4.16i).

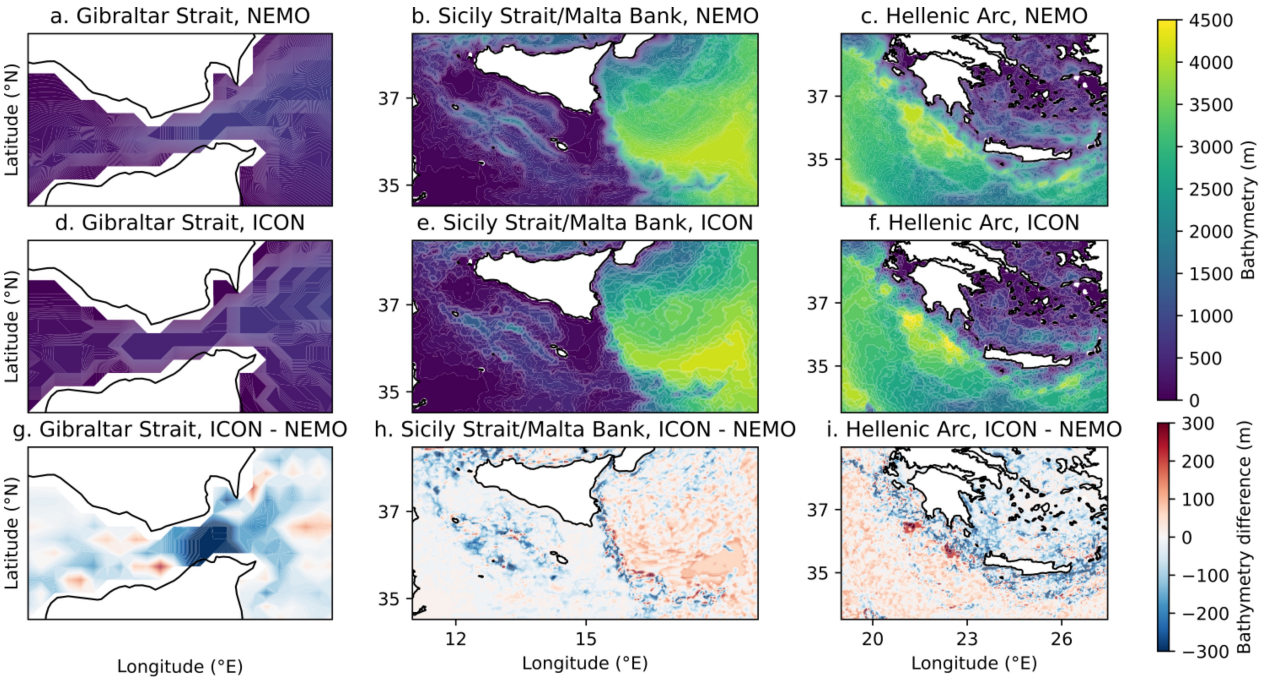

Figure 4.16: Model bathymetry in key regions for internal tide generation: Gibraltar Strait/Alboran Sea (a, d, g), Sicily Strait/Malta Bank (b, e, h), and Hellenic Arc (c, f, i), for NEMO (a, b, c), ICON (d, e, f), and the difference between models, ICON - NEMO (g, h, i).

4.5 Conclusions

Internal tides in the Mediterranean Sea were mapped in the whole basin for the first time. Three major generation sites are found: firstly, the Gibraltar Strait and Alboran Sea, secondly, the Sicily Strait and Malta Bank in the central Mediterranean Sea, and finally, the Hellenic Arc, as well as several minor generation sites in the Adriatic Sea. Both diurnal and semidiurnal internal tides were analysed, with a particular focus on the M2 and K1 components. It was found that the two components have different importance in different regions, with M2 being more prominent in the Western Mediterranean Sea and Cretan Passage, and K1 being most important in the central and southeastern parts of the basin. Semidiurnal internal tides propagate for up to hundreds of kilometres in the Mediterranean Sea, both in the eastern and western basins, particularly in the Algerian Sea, Tyrrhenian Sea, and Ionian Sea, which respectively propagate from the three key generation sites listed above. The first two modes of the M2 internal tide and first three modes of the K1 internal tide are resolved by the numerical models, and have wavelengths comparable to Li

et al. (2015, 2017) for the M2 and K1 components respectively in the NEMO experiment, whereas the ICON-O simulation has shorter wavelengths than suggested by the literature in several regions.

The two numerical experiments found similar generation sites and propagation regions for internal tides, but the specific wavelengths, the propagation direction, and propagation distance varies between the two experiments. Some reasons for this include differences in stratification, model bathymetry, and the calculation of barotropic tides, as well as particularly differing configurations of key regions such as the Gibraltar Strait between the two model implementations. The barotropic tidal amplitudes and phases provided by the NEMO and ICON experiments are compared to a global barotropic model used as a reference Egbert and Ray (2003) in Appendix C. However, further validation through satellite data at the sea surface, as well as using data from cruises in some isolated regions, such as that of Oddo et al. (2023), could be used to better understand which model has a more accurate representation of internal tides.

This work was an initial step in mapping internal tides for the first time throughout the Mediterranean basin using a high-resolution numerical model. Next steps for the study of internal tides in the Mediterranean Sea could include an analysis of interactions with other mesoscale phenomena, particularly near-inertial waves, as was briefly discussed in Chapter 3 as well as in this chapter of this work, and the interaction between internal tides and mesoscale eddies, which are a key feature in the Mediterranean Sea circulation. Further to this, it is clear that high resolution, both in the horizontal and vertical components, and realistic bathymetry are important to simulate internal tides accurately, especially in a complex coastal ocean with steep topography and narrow straits, such as the Mediterranean Sea. It is possible that internal tides are generated in other regions of steep topography such as small islands and seamounts, and narrow straits such as the Messina Strait, which are not properly resolved by the model implementations used in this work (in ICON, the Messina Strait is closed, in NEMO, it is open but poorly resolved). A regional study of the central Mediterranean Seas with sub-kilometre scale horizontal resolution would be a particularly useful step in understanding the internal tides in this region.

Chapter 5: Summary

In this thesis, numerical experiments were carried out to investigate the wider effects of both barotropic and internal tides in the Mediterranean Sea. This led to a better understanding of the scales at which tides have an impact, and the phenomena with which they interact. In particular, internal tides in the Mediterranean Sea were investigated, advancing our knowledge on their generation sites and demonstrating that internal tides propagate over long distances in the basin. Further to these results, the numerical model used for the majority of the experiments was improved in its topographic configuration in the Gibraltar Strait, and a more sophisticated vertical mixing scheme was tested and implemented. In the next section, I return to discuss the outcomes of the questions posed in Chapter 1.4.

5.1 Conclusions

The first part of this thesis compares a tidal model to a similar implementation of the same model without tides, to find how tides interact at spatial and temporal scales away from the direct impact of tides on the sea surface height. Tides impact a wide variety of phenomena in the Mediterranean Sea, interacting with free barotropic oscillations and near-inertial internal waves. Tides also interact with the topography: internal tides appear to be generated in several regions. Further to this, tides increase the mixed layer depth across the basin, and enhance deep water mass formation rates in the Western Mediterranean Deep Water and Levantine Intermediate Water formation regions.

During this initial study of tides in the Mediterranean Sea, it became clear that the vertical motion at two points in the central Gibraltar Strait were inaccurate in the experiment with tides, and four tests modifying the bathymetry were performed to rectify this. It was found that a smoothed bathymetry in the Gibraltar Strait improved both the vertical motion in the Strait and crucially the mass transport in and out of the Mediterranean Sea, compared to the original tidal experiment. The parameterization used for vertical mixing was also tested, through a suite of experiments that used a variety of parameter values within the

turbulent kinetic energy (TKE) mixing scheme, comparing it to the Richardson number-based parameterization that was used for previous experiments. These experiments were validated against observations of temperature and salinity. Many of the TKE experiments performed less well than the control parameterization, but one which used enhanced vertical diffusion without a Langmuir cell parameterization was comparable to the Richardson number-based parameterization. This scheme was then used for the final experiment.

The final experiment was a study on internal tides in the Mediterranean Sea, motivated by the findings of the first experiments, but using the updated Gibraltar Strait bathymetry and vertical mixing scheme, and comparing it to a second hydrodynamic numerical model of the ocean, ICON-O. Internal tides are widespread in the Mediterranean Sea. The key generation sites are 1. the Gibraltar Strait, 2. the Sicily Strait and Malta Bank regions of the central Mediterranean Sea, and 3. the Hellenic Arc. Semidiurnal internal tides propagate over long distances in 1. the Algerian Sea, generated at the Gibraltar Strait, 2. the Tyrrhenian Sea, generated at the Sicily Strait, and 3. the Ionian Sea, generated at the Hellenic Arc. Internal tides generated at the Malta Bank are mostly diurnal, so they dissipate close to the generation site. The model implementations are able to resolve the first two vertical modes of the M2 internal tide and the first three modes of the K1 internal tide, which are at wavelengths comparable to previous literature from the global ocean (Li et al., 2015, 2017).

Both the NEMO and ICON-O experiments have broadly the same sites of generation and propagation of internal tides. However, they differ in their stratification, bathymetry, and implementation of barotropic tides, which lead to differences in the results of each model when analysing internal tides. The ICON-O implementation is also less able to resolve multiple modes of the internal tides, which is likely due to its slightly lower resolution.

5.2 Limitations of this work

This thesis represents a step forward in our understanding of tides and their interactions in the Mediterranean Sea. However, there are limitations to this work, which could be improved upon for future experiments in this field.

Firstly, neither model is run at a horizontal resolution high enough to realistically represent the Gibraltar Strait. Although the values of mass transport are realistic in the Strait in the NEMO implementation, a higher-resolution model with a realistic bathymetry would improve the accuracy of the dynamics of the region overall, likely also impacting the generation of internal tides. An unstructured grid or nested model of the Mediterranean Sea and Gibraltar Strait would be required to achieve a realistic configuration in the region.

Another limitation of this work comes from the TKE configuration. Although the TKE scheme has more sophisticated model physics than the Richardson number-based parameterization, and the configuration chosen had comparable validation results, there is a lot of room for improvement here. Coupling the ocean model with a wave model allows for a more sophisticated configuration of the Langmuir cell parameterization, which would be a first step towards this. Another possibility would be to conduct idealised experiments in a small region, in order to fully understand the impacts of changing each parameter within the TKE scheme, and how each parameter influences the others. Further to this, it could be the case that different parameter values, or even different parameterizations, are optimal for different parts of the basin. Gutjahr et al. (2021) found that mixing scheme performance was not uniform across the global ocean, and considering the results of the sensitivity tests, this is also the case within the Mediterranean Sea. Further customisation by region could improve results.

A limitation to the study on internal tides is that a single month of data, although enough to understand the distribution of internal tides in the Mediterranean Sea, doesn't allow for accurate validation of the models. It is clear that there are some differences between the models, and a longer dataset would allow for the models to be compared to data from tide gauges as well as Argo floats and the observed mass transport at the Gibraltar Strait. This would clarify which model better represents internal tides in the Mediterranean Sea. Moreover, a longer model integration time would allow for an analysis of internal tides by season, which would be an interesting route for future work.

5.3 Future study

Although the scientific questions set out for this work have been answered, there are still many open questions in this field, and my thesis has raised some questions that could be studied in the future. Studies that resolve some of the limitations in the above section would naturally be a first step for future work, but other questions that were raised in Chapters 3-4 would also lead to valuable results for our understanding of Mediterranean Sea dynamics.

Chapter 3 described the interactions between tides and other high-frequency phenomena in the Mediterranean Sea. It is also important to understand their interactions with lower frequency phenomena, particularly the Mediterranean Sea Overturning Circulation, which was not done as part of this work. A study on the Mediterranean Sea Overturning Circulation would require a model run of several decades, to allow the circulation to fully spin-up. It is known that tides impact the global meridional overturning circulation (Munk and Wunsch, 1998), so a study specific to this phenomenon in the Mediterranean Sea would represent a step forward in our knowledge of the region.

Barotropic modes are an important phenomenon in the Mediterranean Sea, but there are no recent studies calculating their frequencies with state-of-the-art techniques. A study using an up-to-date numerical model, such as the NEMO configuration used in this work, which confirms all the barotropic oscillation periods in the Mediterranean Sea and its sub-basins, would be an important new dataset for studies of a wide variety of processes in the region.

Another useful approach for studying both barotropic and internal tides would be to use an ensemble of experiments. Since this work has shown that changing the bathymetry configuration at the Gibraltar Strait has effects on the vertical motion of the entire Mediterranean Sea, an ensemble based on this would be a natural next step. This would be particularly interesting for the study of internal tides, which are generated at the Gibraltar Strait topography.

Bibliography

Agresti, V., 2018: Effects of tidal motion on the Mediterranean Sea General Circulation. Ph.D. thesis, University of Bologna, doi:10.6092/unibo/amsdottorato/8516.

Alford, M. H., M. C. Gregg, V. Zervakis, and H. Kontoyiannis, 2012: Internal wave measurements on the Cycladic Plateauof the Aegean Sea. *J. Geophys. Res.*, **117**, C01 015, doi:10.1029/2011JC007488.

Ali, E., W. Cramer, J. Carnicer, E. Georgopoulou, N. J. M. Hilmi, G. L. Cozannet, and P. Lionello, 2022: Cross-Chapter Paper 4: Mediterranean Region. *Climate Change 2022: Impacts, Adaptation and Vulnerability. Contribution of Working Group II to the Sixth Assessment Report of the Intergovernmental Panel on Climate Change [H.-O. Pörtner, D.C. Roberts, M. Tignor, E.S. Poloczanska, K. Mintenbeck, A. Alegría, M. Craig, S. Langsdorf, S. Löschke, V. Möller, A. Okem, B. Rama (eds.)]*, Cambridge University Press, Cambridge, UK and New York, NY, USA, 2233–2272, doi:10.1017/9781009325844.021.

Arbic, B. K., 2022: Incorporating tides and internal gravity waves within global ocean general circulation models: A review. *Progr. Oceanogr.*, **206 (102824)**, doi:10.1016/j.pocean.2022.102824.

Arbic, B. K., A. J. Wallcraft, and E. J. Metzger, 2010: Concurrent simulation of the eddying general circulation and tides in a global ocean model. *Ocean Modell.*, **32 (3)**, 175–187, doi:10.1016/j.ocemod.2010.01.007.

Argo, 2022: Argo float data and metadata from Global Data Assembly Centre (Argo GDAC). *SEANOE*, doi:10.17882/42182.

Armi, L., and D. Farmer, 1985: The internal hydraulics of the Strait of Gibraltar and associated sills and narrows. *Oceanol. Acta*, **8 (1)**, 37–46.

Axell, L. B., 2002: Wind-driven internal waves and Langmuir circulations in a numerical ocean model of the southern Baltic Sea. *J. Geophys. Res. Oceans*, **107 (C11)**, 3204, doi:10.1029/2001JC000922.

Baines, P. G., 1982: On internal tide generation models. *Deep Sea Res., Part A*, **29 (3)**, 307–338.

Becker, J. J., and Coauthors, 2009: Global Bathymetry and Elevation Data at 30 Arc Seconds Resolution: SRTM30_PLUS. *Marine Geodesy*, **32 (4)**, 355–371, URL `http://topex.ucsd.edu/sandwell/publications/124_MG_Becker.pdf`.

Bertotti, L., J.-R. Bidlot, R. Buizza, L. Cavaleri, and M. Janousek, 2011: Deterministic and ensemble-based prediction of Adriatic Sea sirocco storms leading to 'acqua alta' in Venice. *Q. J. R. Meteorol. Soc.*, **137 (659)**, 1446–1466, doi:10.1002/qj.861.

Beuvier, J., and Coauthors, 2012: Spreading of the Western Mediterranean Deep Water after winter 2005: Time scales and deep cyclone transport. *J. Geophys. Res. Oceans*, **117 (C7)**, doi:10.1029/2011JC007679.

Blanke, B., and P. Delécluse, 1993: Variability of the Tropical Atlantic Ocean Simulated by a General Circulation Model with Two Different Mixed-Layer Physics. *J. Phys. Oceanogr.*, **23 (7)**, 1363 – 1388, doi:10.1175/1520-0485(1993)023<1363:VOTTAO>2.0.CO;2.

Buijsman, M. C., and Coauthors, 2014: Three-Dimensional Double-Ridge Internal Tide Resonance in Luzon Strait. *J. Phys. Oceanogr.*, **44 (3)**, 850 – 869, doi:10.1175/JPO-D-13-024.1.

Candela, J., C. Winant, and A. Ruiz, 1990: Tides in the Strait of Gibraltar. *J. Geophys. Res. Oceans*, **95 (C5)**, 7313–7335, doi:10.1029/JC095iC05p07313.

Cartwright, D. E., 1999: *Tides: A Scientific History*. Cambridge University Press, Cambridge, UK.

Clementi, E., and Coauthors, 2019: Mediterranean Sea Analysis and Forecast (CMEMS MED-Currents, EAS5 system) (Version 1) [Data set]. *Copernicus Monitoring Environment Marine Service (CMEMS)*, doi: 10.25423/CMCC/MEDSEA_ANALYSIS_FORECAST_PHY_006_013_EAS5.

Clementi, E., and Coauthors, 2021: Mediterranean Sea Physical Analysis and Forecast (CMEMS MED-Currents, EAS6 system).

Copernicus Monitoring Environment Marine Service (CMEMS), doi: 10.25423/CMCC/MEDSEA_ANALYSISFORECAST_PHY_006_013_EAS6.

Coppini, G., and Coauthors, 2023: The Mediterranean Forecasting System – Part 1: Evolution and performance. *Ocean Sci.*, **19 (5)**, 1483–1516, doi:10.5194/os-19-1483-2023.

Craik, L. D. D., and S. Leibovich, 1976: A rational model for Langmuir circulations. *J. Fluid Mech.*, **73 (3)**, 401–426, doi:10.1017/S0022112076001420.

Cuypers, Y., P. Bouruet-Aubertot, C. Marec, and J.-L. Fuda, 2012: Characterization of turbulence from a fine-scale parameterization and microstructure measurements in the Mediterranean Sea during the BOUM experiment. *Biogeosciences*, **9 (8)**, 3131–3149, doi: 10.5194/bg-9-3131-2012.

Delrosso, D., 2020: Numerical modelling and analysis of riverine influences in the Mediterranean Sea. Ph.D. thesis, University of Bologna, doi:10.6092/unibo/amsdottorato/9392.

Di Muzio, E., M. Riemer, A. H. Fink, and M. Maier-Gerber, 2019: Assessing the predictability of Medicanes in ECMWF ensemble forecasts using an object-based approach. *Q. J. R. Meteorol. Soc.*, **145 (720)**, 1202–1217, doi:10.1002/qj.3489.

Dunphy, M., and K. G. Lamb, 2014: Focusing and vertical mode scattering of the first mode internal tide by mesoscale eddy interaction. *J. Geophys. Res. Oceans*, **119 (1)**, 523–536, doi:10.1002/2013JC009293.

Durski, S. M., S. M. Glenn, and D. B. Haidvogel, 2004: Vertical mixing schemes in the coastal ocean: Comparison of the level 2.5 Mellor-Yamada scheme with an enhanced version of the K profile parameterization. *J. Geophys. Res. Oceans*, **109 (C1)**, doi:10.1029/2002JC001702.

Egbert, G. D., and S. Y. Erofeeva, 2002: Efficient inverse modeling of barotropic ocean tides. *J. Atmosph. Oceanic Tech.*, **19.2**, 183–204.

Egbert, G. D., and R. D. Ray, 2003: Semi-diurnal and diurnal tidal dissipation from TOPEX/Poseidon altimetry. *Geophys. Res. Lett.*, **30 (17)**, 1907, doi: 10.1029/2003GL017676.

Emery, W. J., W. G. Lee, and L. Magaard, 1984: Geographic and Seasonal Distributions of Brunt–Väisälä Frequency and Rossby Radii in the North Pacific and North Atlantic. *J. Phys. Oceanogr.*, **14**, 294–317, doi:10.1175/1520-0485(1984)014<0294:GASDOB>2.0.CO;2.

EMODnet Bathymetry Consortium, 2020: EMODnet Digital Bathymetry Digital Terrain Model (DTM). doi:10.12770/bb6a87dd-e579-4036-abe1-e649cea9881a.

Escudier, R., and Coauthors, 2021: A High Resolution Reanalysis for the Mediterranean Sea. *Front. Earth Sci.*, **9 (702285)**, doi:10.3389/feart.2021.702285.

Farmer, D. M., L. Armi, L. Armi, and D. M. Farmer, 1988: The flow of Atlantic water through the Strait of Gibraltar. *Prog. Oceanogr.*, **21 (1)**, 1–103, doi:10.1016/0079-6611(88)90055-9.

Fernández, V., L. Umlauf, S. Dobricic, H. Burchard, and N. Pinardi, 2006: Validation and intercomparison of two vertical-mixing schemes in the Mediterranean Sea. *Ocean Sci. Discuss.*, **3 (6)**, 1945–1976, URL `https://hal.science/hal-00298452`.

Fox-Kemper, B., and Coauthors, 2019: Challenges and Prospects in Ocean Circulation Models. *Front. Mar. Sci.*, **6**, doi:10.3389/fmars.2019.00065.

Galloudec, O. L., and Coauthors, 2022: Global Ocean Physical Analysis and Forecasting Product. *Copernicus Monitoring Environment Marine Service (CMEMS)*, doi:10.48670/moi-00016.

García Lafuente, J., E. Bruque Pozas, J. C. Sánchez Garrido, G. Sannino, and S. Sammartino, 2013: The interface mixing layer and the tidal dynamics at the eastern part of the Strait of Gibraltar. *J. Mar. Syst.*, **117-118**, 31–42, doi:10.1016/j.jmarsys.2013.02.014.

Gaspar, P., Y. Grégoris, and J.-M. Lefevre, 1990: A simple eddy kinetic energy model for simulations of the oceanic vertical mixing: Tests at station Papa and long-term upper ocean study site. *J. Geophys. Res. Oceans*, **95 (C9)**, 16 179–16 193, doi:10.1029/JC095iC09p16179.

Gasparini, G. P., D. A. Smeed, S. Alderson, S. Sparnocchia, A. Vetrano, and S. Mazzola,

2004: Tidal and subtidal currents in the Strait of Sicily. *J. Geophys. Res.*, **109**, C02 011, doi:10.1029/2003JC002011.

Gates, L. D., S. Hagemann, and C. Golz, 1993: Observed historical discharge data from major rivers for climate model validation. *Tech. Rep.*, **307**.

GEBCO Bathymetric Compilation Group 2014, 2014: The GEBCO_2014 Grid, version 20150318. *NERC EDS British Oceanographic Data Centre NOC*, URL `www.gebco.net`.

Gent, P. R., 2018: A commentary on the Atlantic meridional overturning circulation stability in climate models. *Ocean Modell.*, **122**, 57–66, doi:10.1016/j.ocemod.2017.12.006.

Giordani, H., C. Lebeaupin-Brossier, F. Léger, and G. Caniaux, 2017: A PV-approach for dense water formation along fronts: Application to the Northwestern Mediterranean. *J. Geophys. Res. Oceans*, **122 (2)**, 995–1015, doi:https://doi.org/10.1002/2016JC012019.

Giorgetta, M. A., and Coauthors, 2018: ICON-A, the Atmosphere Component of the ICON Earth System Model: I. Model Description. *J. Adv. Modell. Earth Systems*, **10 (7)**, 1613–1637, doi:10.1029/2017MS001242.

Gonzalez, N. M., R. Waldman, G. Sannino, H. Giordani, and S. Somot, 2023: Understanding tidal mixing at the Strait of Gibraltar: A high-resolution model approach. *Progr. Oceanogr.*, **212**, 102 980, doi:10.1016/j.pocean.2023.102980.

Green, J., J. Simpson, S. Thorpe, and T. Rippeth, 2010: Observations of internal tidal waves in the isolated seasonally stratified region of the western Irish Sea. *Continental Shelf Res.*, **30 (2)**, 214–225, doi:10.1016/j.csr.2009.11.004.

Guo, Z., S. Wang, A. Cao, J. Xie, J. Song, and X. Guo, 2023: Refraction of the M2 internal tides by mesoscale eddies in the South China Sea. *Deep Sea Res. Part I: Oceanogr. Res. Pap.*, **192**, 103 946, doi:10.1016/j.dsr.2022.103946.

Gutjahr, O., N. Brüggemann, H. Haak, J. H. Jungclaus, D. A. Putrasahan, K. Lohmann, and J.-S. von Storch, 2021: Comparison of ocean vertical mixing schemes in the Max Planck Institute Earth System Model (MPI-ESM1.2). *Geosci. Model Dev.*, **14 (5)**, 2317–2349, doi:10.5194/gmd-14-2317-2021.

Halpern, D., Y. Chao, C.-C. Ma, and C. R. Mechoso, 1995: Comparison of tropical Pacific temperature and current simulations with two vertical mixing schemes embedded in an ocean general circulation model and reference to observations. *J. Geophys. Res. Oceans*, **100 (C2)**, 2515–2522, doi:10.1029/94JC03043.

Harzallah, A., M. Alioua, and L. Li, 2014: Mass exchange at the Strait of Gibraltar in response to tidal and lower frequency forcing as simulated by a Mediterranean Sea model. *Tellus A: Dyn. Meteorol. Oceanogr.*, **66 (1)**, 23 871, doi:10.3402/tellusa.v66.23871.

Hersbach, H., and Coauthors, 2023: ERA5 hourly data on single levels from 1979 to present (Copernicus Climate Change Service (C3S) Climate Data Store (CDS)). doi: 10.24381/cds.adbb2d47.

Hilt, M., and Coauthors, 2020: Numerical modelling of hydraulic control, solitary waves and primary instabilities in the Strait of Gibraltar. *Ocean Modell.*, **151**, 101 642, doi: 10.1016/j.ocemod.2020.101642.

Izquierdo, A., and U. Mikolajewicz, 2019: The role of tides in the spreading of Mediterranean Outflow waters along the southwestern Iberian margin. *Ocean Modell.*, **133**, 27–43, doi:10.1016/j.ocemod.2018.08.003.

Jacox, M. G., and Coauthors, 2022: Global seasonal forecasts of marine heatwaves. *Nature*, **604**, 486–490, doi:10.1038/s41586-022-04573-9.

Kang, D., 2012: Barotropic and Baroclinic Tidal Energy. *Energy Conservation*, A. Z. Ahmed, Ed., IntechOpen, Rijeka, chap. 2, doi:10.5772/52293.

Karagiorgos, J., V. Vervatis, and S. Sofianos, 2020: The Impact of Tides on the Bay of Biscay Dynamics. *J. Mar. Sci. Eng.*, **8 (8)**, doi:10.3390/jmse8080617.

Kelly, S. M., and P. F. J. Lermusiaux, 2016: Internal-tide interactions with the Gulf Stream and Middle Atlantic Bight shelfbreak front. *J. Geophys. Res. Oceans*, **121**, 6271–6294, doi:10.1002/2016JC011639.

Korn, P., and Coauthors, 2022: ICON-O: The Ocean Component of the ICON Earth System Model—Global Simulation Characteristics and Local Telescoping Capability. *J. Adv. Modell. Earth Syst.*, **14 (10)**, e2021MS002 952, doi:10.1029/2021MS002952.

Lafuente, J. G., J. M. Vargas, F. Plaza, T. Sarhan, J. Candela, and B. Bascheck, 2000: Tide at the eastern section of the Strait of Gibraltar. *J. Geophys. Res. Oceans*, **105 (C6)**, 14 197–14 213, doi:10.1029/2000JC900007.

Lahaye, N., J. Gula, and G. Roullet, 2020: Internal Tide Cycle and Topographic Scattering Over the North Mid-Atlantic Ridge. *J. Geophys. Res. Oceans*, **125 (12)**, e2020JC016 376, doi:10.1029/2020JC016376.

Lamy, A., C. Millot, and J. M. Molines, 1981: Bottom Pressure and Sea Level Measurements in the Gulf of Lions. *J. Phys. Oceanogr.*, **11**, 394–409, doi:10.1175/1520-0485(1981)011<0394:BPASLM>2.0.CO;2.

Large, W. G., J. C. McWilliams, and S. C. Doney, 1994: Oceanic vertical mixing: A review and a model with a nonlocal boundary layer parameterization. *Rev. Geophys.*, **32 (4)**, 363–403, doi:10.1029/94RG01872.

Leder, N., and M. Orlić, 2004: Fundamental Adriatic seiche recorded by current meters. *Ann. Geophys.*, **22 (5)**, 1449–1464.

Lee, H.-C., A. Rosatib, and M. J. Spelman, 2006: Barotropic tidal mixing effects in a coupled climate model: Oceanic conditions in the Northern Atlantic. *Ocean Modell.*, **11**, 464–477, doi:10.1016/j.ocemod.2005.03.003.

Li, Q., and Coauthors, 2019: Comparing Ocean Surface Boundary Vertical Mixing Schemes Including Langmuir Turbulence. *J. Adv. Model. Earth Syst.*, **11 (11)**, 3545–3592, doi:10.1029/2019MS001810.

Li, Z., and J.-S. von Storch, 2020: M2 Internal-Tide Generation in STORMTIDE2. *J. Geophys. Res. Oceans*, **125 (8)**, e2019JC015 453, doi:10.1029/2019JC015453.

Li, Z., J.-S. von Storch, and M. Müller, 2015: The M2 Internal Tide Simulated by a 1/10° OGCM. *J. Phys. Oceanogr.*, **45 (12)**, 3119 – 3135, doi:10.1175/JPO-D-14-0228.1.

Li, Z., J.-S. von Storch, and M. Müller, 2017: The K1 internal tide simulated by a 1/10° OGCM. *Ocean Modell.*, **113**, 145–156, doi:10.1016/j.ocemod.2017.04.002.

Logemann, K., L. Linardakis, P. Korn, and C. Schrum, 2021: Global tide simulations with ICON-O: testing the model performance on highly irregular meshes. *Ocean Dyn.*, **71**, 43–57, doi:10.1007/s10236-020-01428-7.

Lozano, C. J., and J. Candela, 1995: The M2 tide in the Mediterranean Sea: Dynamic analysis and data assimilation. *Oceanol. Acta*, **18 (4)**, 419–441.

Madec, G., P. Delecluse, M. Crepon, and M. Chartier, 1991: A Three-Dimensional Numerical Study of Deep-Water Formation in the Northwestern Mediterranean Sea. *J. Phys. Oceanogr.*, **21 (9)**, 1349–1371, doi:10.1175/1520-0485(1991)021<1349:ATDNSO>2.0.CO;2.

Madec, G., P. Delecluse, M. Imbard, and C. Levy, 1998: OPA 8.1 Ocean general circulation model reference manual. *Note du Pôle de modélisation*, **11**, URL `https://www.nemo-ocean.eu/wp-content/uploads/Doc_OPA8.1.pdf`.

Madec, G., and Coauthors, 2019: *NEMO ocean engine*. doi:10.5281/zenodo.1464816.

Maicu, F., 2023: A coupled ocean-atmosphere system for short term forecasting in the southern european seas. Ph.D. thesis, University of Bologna, doi:10.48676/unibo/amsdottorato/10911.

Mauritzen, C., Y. Morel, and J. Paillet, 2001: On the influence of Mediterranean Water on the Central Waters of the North Atlantic Ocean. *Deep Sea Res., Part I*, **48 (2)**, 347–381, doi:S0967-0637(00)00043-1.

McDonagh, B., E. Clementi, A. C. Goglio, and N. Pinardi, 2023: The characteristics of tides and their effects on the general circulation of the Mediterranean Sea. *EGUsphere [preprint]*, doi:10.5194/egusphere-2023-2251.

Medvedev, I. P., I. Vilibić, and A. B. Rabinovich, 2020: Tidal Resonance in the Adriatic Sea: Observational Evidence. *J. Geophys. Res. Oceans*, **125 (8)**, e2020JC016 168, doi:10.1029/2020JC016168.

Melet, A., R. Hallberg, S. Legg, and K. Polzin, 2013: Sensitivity of the Ocean State to the Vertical Distribution of Internal-Tide-Driven Mixing. *J. Phys. Oceanogr.*, **43 (3)**, 602 – 615, doi:10.1175/JPO-D-12-055.1.

Mellor, G. L., and T. Yamada, 1982: Development of a turbulence closure model for geophysical fluid problems. *Rev. Geophys.*, **20 (4)**, 851–875.

Merrifield, M. A., P. E. Holloway, and T. M. S. Johnston, 2001: The generation of internal tides at the Hawaiian Ridge. *Geophys. Res. Lett.*, **28 (4)**, 559–562, doi: 10.1029/2000GL011749.

Mihanović, H., M. Orlić, and Z. Pasarić, 2009: Diurnal thermocline oscillations driven by tidal flow around an island in the Middle Adriatic. *J. Marine Sys.*, **78**, S157–S168, doi: 10.1016/j.jmarsys.2009.01.021.

Misra, V., A. Mishra, and H. Li, 2016: The sensitivity of the regional coupled ocean-atmosphere simulations over the Intra-Americas seas to the prescribed bathymetry. *Dyn. Atmos. Oceans*, **76**, 29–51, doi:10.1016/j.dynatmoce.2016.08.007.

Morozov, E. G., K. Trulsen, M. G. Velarde, and V. I. Vlasenko, 2002: Internal Tides in the Strait of Gibraltar. *J. Phys. Oceanogr.*, **32 (11)**, 3193–3206, doi:10.1175/1520-0485(2002)032<3193:ITITSO>2.0.CO;2.

Munk, W., and C. Wunsch, 1998: Abyssal recipes II: energetics of tidal and wind mixing. *Deep Sea Res., Part I*, **45 (12)**, 1977–2010, doi:10.1016/S0967-0637(98)00070-3.

Müller, M., H. Haak, J. Jungclaus, J. Sündermann, and M. Thomas, 2010: The effect of ocean tides on a climate model simulation. *Ocean Modell.*, **35 (4)**, 304–313, doi: 10.1016/j.ocemod.2010.09.001.

Nagai, T., and T. Hibiya, 2015: Internal tides and associated vertical mixing in the Indonesian Archipelago. *J. Geophys. Res. Oceans*, **120 (5)**, 3373–3390, doi: 10.1002/2014JC010592.

Nakamura, T., T. Awaji, T. Hatayama, K. Akitomo, T. Takizawa, T. Kono, Y. Kawasaki, and M. Fukasawa, 2000: The Generation of Large-Amplitude Unsteady Lee Waves by Subinertial K1 Tidal Flow: A Possible Vertical Mixing Mechanism in the Kuril Straits. *J. Phys. Oceanogr.*, **30**, 1601–1621, doi:10.1175/1520-0485(2000)030<1601:TGOLAU>2.0.CO;2.

Naranjo, C., J. Lafuente, G. Sannino, and J. Sanchez-Garrido, 2014: How much do tides affect the circulation of the Mediterranean Sea? From local processes in the Strait of Gibraltar to basin-scale effects. *Prog. Oceanogr.*, **127**, 108–116, doi:j.pocean.2014.06.005.

Niwa, Y., and T. Hibiya, 2001: Numerical study of the spatial distribution of the M2 internal tide in the Pacific Ocean. *J. Geophys. Res. Oceans*, **106 (C10)**, 22 441–22 449, doi:10.1029/2000JC000770.

Oddo, P., P. Poulain, S. Falchetti, A. Storto, and G. Zappa, 2023: Internal tides in the central Mediterranean Sea: observational evidence and numerical studies. *Ocean Dyn.*, **73**, 145–163, doi:10.1007/s10236-023-01545-z.

Pacanowski, R. C., and S. G. H. Philander, 1981: Parameterization of Vertical Mixing in Numerical Models of Tropical Oceans. *J. Phys. Oceanogr.*, **11 (11)**, 1443–1451, doi:10.1175/1520-0485(1981)011<1443:POVMIN>2.0.CO;2.

Palma, M., and Coauthors, 2020: Short-term, linear, and non-linear local effects of the tides on the surface dynamics in a new, high-resolution model of the Mediterranean Sea circulation. *Ocean Dyn.*, **70**, 935–963, doi:10.1007/s10236-020-01364-6.

Pettenuzzo, D., W. Large, and N. Pinardi, 2010: On the corrections of ERA-40 surface flux products consistent with the Mediterranean heat and water budgets and the connection between basin surface total heat flux and NAO. *J. Geophys. Res.*, **115 (C06022)**, doi:10.1029/2009JC005631.

Pinardi, N., P. Cessi, F. Borile, and C. L. P. Wolfe, 2019: The Mediterranean Sea Overturning Circulation. *J. Phys. Oceanogr.*, **49 (7)**, 1699 – 1721, doi:10.1175/JPO-D-18-0254.1.

Pinardi, N., M. Zavatarelli, E. Arneri, A. Crise, and M. Ravaioli, 2006: The physical, sedimentary and ecological structure and variability of shelf areas in the Mediterranean Sea.

Pinardi, N., and Coauthors, 2015: Mediterranean Sea large-scale low-frequency ocean variability and water mass formation rates from 1987 to 2007: A retrospective analysis. *Prog. Oceanogr.*, **132**, 318–332, doi:10.1016/j.pocean.2013.11.003.

Robinson, A. R., W. G. Leslie, A. Theocharis, and A. Lascaratos, 2001: Mediterranean Sea Circulation. *Ocean Currents [J. Steele, S. Thorpe, K. Turekian (eds.)]*, Elsevier, 283–306.

Rodgers, K. B., and Coauthors, 2014: Strong sensitivity of Southern Ocean carbon uptake and nutrient cycling to wind stirring. *Biogeosciences*, **11 (15)**, 4077–4098, doi: 10.5194/bg-11-4077-2014.

Röske, F., 2006: A global heat and freshwater forcing dataset for ocean models. *Ocean Modell.*, **11 (3)**, 235–297, doi:10.1016/j.ocemod.2004.12.005.

Sanchez-Roman, A., G. Jorda, G. Sannino, and D. Gomis, 2018: Modelling study of transformations of the exchange flows along the Strait of Gibraltar. *Ocean Sci.*, **14 (6)**, 1547–1566, doi:10.5194/os-14-1547-2018.

Sannino, G., A. Carillo, G. Pisacane, and C. Naranjo, 2015: On the relevance of tidal forcing in modelling the Mediterranean thermohaline circulation. *Prog. Oceanogr.*, **134**, 304–329, doi:10.1016/j.pocean.2015.03.002.

Sannino, G., M. Herrmann, A. Carillo, V. Rupolo, V. Ruggiero, V. Artale, and P. Heimbach, 2009: An eddy-permitting model of the Mediterranean Sea with a two-way grid refinement at the Strait of Gibraltar. *Ocean Modell.*, **30 (1)**, 56–72, doi: /10.1016/j.ocemod.2009.06.002.

Sannino, G., J. C. Sánchez Garrido, L. Liberti, and L. Pratt, 2014: *Exchange Flow through the Strait of Gibraltar as Simulated by a σ-Coordinate Hydrostatic Model and a z-Coordinate Nonhydrostatic Model*, chap. 3, 25–50. American Geophysical Union (AGU), doi:10.1002/9781118847572.ch3.

Schwab, D. J., and D. B. Rao, 1983: Barotropic oscillations of the Mediterranean and Adriatic Seas. *Tellus A*, **35A (5)**, 417–427, doi:10.1111/j.1600-0870.1983.tb00216.x.

Shapiro, R., 1970: Smoothing, filtering, and boundary effects. *Rev. Geophys.*, **8 (2)**, 359–387, doi:10.1029/RG008i002p00359.

Soto-Navarro, J., F. Criado-Aldeanueva, J. García-Lafuente, and A. Sánchez-Román, 2010: Estimation of the Atlantic inflow through the Strait of Gibraltar from climatological and in situ data. *J. Geophys. Res. Oceans*, **115 (C10)**, doi:10.1029/2010JC006302.

Soto-Navarro, J., S. Somot, F. Sevault, J. Beuvier, F. Criado-Aldeanueva, J. García-Lafuente, and K. Béranger, 2015: Evaluation of regional ocean circulation models for the Mediter-

ranean Sea at the Strait of Gibraltar: volume transport and thermohaline properties of the outflow. *Clim. Dyn.*, **44**, 1277–1292, doi:10.1007/s00382-014-2179-4.

St. Laurent, L. C., H. L. Simmons, and S. R. Jayne, 2002: Estimating tidally driven mixing in the deep ocean. *Geophys. Res. Lett.*, **29 (2106)**, doi:10.1029/2002GL015633.

Sánchez-Román, A., J. García-Lafuente, J. Delgado, J. Sánchez-Garrido, and C. Naranjo, 2012: Spatial and temporal variability of tidal flow in the Strait of Gibraltar. *J. Mar. Syst.*, **98**, 9–17, doi:10.1016/j.jmarsys.2012.02.011.

Sánchez-Román, A., G. Sannino, J. García-Lafuente, A. Carillo, and F. Criado-Aldeanueva, 2009: Transport estimates at the western section of the Strait of Gibraltar: A combined experimental and numerical modeling study. *J. Geophys. Res. Oceans*, **114 (C6)**, doi:10.1029/2008JC005023.

Teixeira, M. A., 2019: Langmuir Circulation and Instability. *Encyclopedia of Ocean Sciences (Third Edition)*, J. K. Cochran, H. J. Bokuniewicz, and P. L. Yager, Eds., third edition ed., Academic Press, Oxford, 92–106, doi:10.1016/B978-0-12-409548-9.04176-2.

Tirodkar, S., R. Murtugudde, M. R. Behera, and S. Balasubramanian, 2022: A Comparative Study of Vertical Mixing Schemes in Modeling the Bay of Bengal Dynamics. *Earth and Space Sci.*, **9 (8)**, e2022EA002 327, doi:10.1029/2022EA002327.

Tsimplis, M. N., R. Proctor, and R. A. Flathe, 1995: A two-dimensional tidal model for the Mediterranean Sea. *J. Geophys. Res.*, **100 (C8)**, 16 223–16 239, doi:10.1029/95JC01671.

Umlauf, L., and H. Burchard, 2005: Second-order turbulence closure models for geophysical boundary layers. A review of recent work. *Cont. Shelf Res.*, **25 (7)**, 795–827, doi:10.1016/j.csr.2004.08.004.

von Storch, J.-S., E. Hertwig, V. Lüschow, N. Brüggemann, H. Haak, P. Korn, and V. Singh, 2023: Open-ocean tides simulated by ICON-O, version icon-2.6.6. *Geosci. Model Dev.*, **16**, 5179–5196, doi:10.5194/gmd-16-5179-2023.

Vázquez, A., N. Stashchuk, V. Vlasenko, M. Bruno, A. Izquierdo, and P. C. Gallacher, 2006: Evidence of multimodal structure of the baroclinic tide in the Strait of Gibraltar. *Geophys. Res. Lett.*, **33 (17)**, doi:10.1029/2006GL026806.

Waldman, R., N. Brüggemann, A. Bosse, M. Spall, S. Somot, and F. Sevault, 2018: Overturning the Mediterranean Thermohaline Circulation. *Geophys. Res. Lett.*, **45 (16)**, 8407–8415, doi:10.1029/2018GL078502.

Wong, A. P. S., and Coauthors, 2020: Argo Data 1999–2019: Two Million Temperature-Salinity Profiles and Subsurface Velocity Observations From a Global Array of Profiling Floats. *Front. Mar. Sci.*, **7**, doi:10.3389/fmars.2020.00700.

Wüst, G., 1961: On the vertical circulation of the Mediterranean Sea. *J. Geophys. Res. (1896-1977)*, **66 (10)**, 3261–3271, doi:10.1029/JZ066i010p03261.

Zhao, Z., M. H. Alford, J. A. MacKinnon, and R. Pinkel, 2010: Long-Range Propagation of the Semidiurnal Internal Tide from the Hawaiian Ridge. *J. Phys. Oceanogr.*, **40 (4)**, 713–736, doi:10.1175/2009JPO4207.1.

Appendices

A Distribution of Argo floats

In Section 2.4, Argo observational data of temperature and salinity are used to validate the experiments against observations. The tables in this appendix show the number of measurements, segmented by layer and region for 2017 (used in Section 2.4.6) and 2017-19 (used in Section 2.4.7), for both salinity and temperature.

Region	0-10m	10-30m	30-60m	60-100m	100-150m	150-300m	300-600m	600-1000m	1000-2000m
Mediterranean Sea	*74,140*	*179,034*	*268,028*	*354,700*	*300,498*	*620,393*	*615,111*	*430,445*	*124,158*
Alboran Sea	2,631	4,673	6,988	9,243	10,734	19,206	10,467	6,285	3,240
South-west Mediterranean (west)	8,293	25,662	38,853	51421	57,587	87,161	74,187	20,331	18,702
North-west Mediterranean	10,367	17,187	25,577	33,624	28,062	59,545	44,081	33,493	39,563
South-west Mediterranean (west)	3,200	4,721	7,047	9,313	7,766	16,062	17,031	12,520	13,001
Tyrrhenian Sea (south)	6,419	16,914	24,976	32,411	24,946	48,620	36,500	15,066	5,229
Tyrrhenian Sea (north)	429	606	861	1,044	513	1,044	888	129	3
Ionian Sea (west)	309	912	1,407	1,851	1,125	1,449	1,068	114	9
Ionian Sea (south-east)	6,123	15,099	22,632	30,207	21,609	60,702	98,670	103,476	6,993
Ionian Sea (north-east)	6,559	17,945	27,014	35,706	30,491	70,683	58,266	52,150	5,912
Adriatic Sea (south)	2,994	8,142	12,102	15,708	5,709	12,822	17,022	4,263	348
Adriatic Sea (north)	0	0	0	0	0	0	0	0	0
Levantine Sea (west)	5,991	15,420	22,926	30,351	27,432	56,820	79,401	65,691	12,705
Aegean Sea	8,719	20,794	31,166	41,618	26,990	64,077	53,771	17,457	3,693
Levantine Sea (central-north)	5,081	12,853	19,287	25,633	25,192	60,441	67,779	70,011	6,780
Levantine Sea (central-south)	5,273	13,390	20,184	27,456	29,594	53,607	40,851	20,711	5,721
Levantine Sea (east)	1,752	4,716	7,008	9,114	2,748	8,154	15,129	8,748	2,259

Table A.1: Number of observations from Argo floats of salinity in 2017, segmented by layer and region within the Mediterranean Sea.

Region	0-10m	10-30m	30-60m	60-100m	100-150m	150-300m	300-600m	600-1000m	1000-2000m
Mediterranean Sea	*74,096*	*175,138*	*262,639*	*353,425*	*300,555*	*620,528*	*615,306*	*430,508*	*124,197*
Alboran Sea	2,592	4,405	6,957	9,243	10,734	19,206	10,467	6,285	3,240
South-west Mediterranean (west)	8,284	24,300	37,751	51,412	57,587	87,161	74,187	20,331	18,702
North-west Mediterranean	10,325	17,095	25,425	33,591	28,062	59,545	44,081	33,493	39,563
South-west Mediterranean (west)	3,200	4,709	7,008	9,274	7,766	16,062	17,031	12,520	13,001
Tyrrhenian Sea (south)	6,403	16,450	24,949	32,442	24,958	48,620	36,500	15,066	5,229
Tyrrhenian Sea (north)	429	606	861	1,044	513	1,044	888	129	3
Ionian Sea (western part)	309	906	1,379	1,851	1,125	1,449	1,068	114	9
Ionian Sea (south-east)	6,123	15,010	22,255	30,105	21,609	60,702	98,670	103,476	6,993
Ionian Sea (north-east)	6,542	17,475	25,882	35,629	30,491	70,683	58,266	52,150	5,912
Adriatic Sea (south)	2,994	7,838	12,022	15,708	5,709	12,822	17,022	4,263	348
Adriatic Sea (north)	0	0	0	0	0	0	0	0	0
Levantine Sea (west)	5,985	15,206	22,502	29,985	27,432	56,820	79,401	65,691	12,705
Aegean Sea	8,797	20,687	30,535	41,422	27,005	64,122	53,861	17,472	3,693
Levantine Sea (central-north)	5,079	12,446	18,696	25,600	25,192	60,441	67,779	70,011	6,780
Levantine Sea (central-south)	5,282	13,379	19,822	27,244	29,624	53,697	40,956	20,759	5,760
Levantine Sea (east)	1,752	4,626	6,595	8,875	2,748	8,154	15,129	8,748	2,259

Table A.2: Number of observations from Argo floats of temperature in 2017, segmented by layer and region within the Mediterranean Sea.

Region	0-10m	10-30m	30-60m	60-100m	100-150m	150-300m	300-600m	600-1000m	1000-2000m
Mediterranean Sea	*204,719*	*439,394*	*658,096*	*872,901*	*770,914*	*1,606,468*	*1,619,818*	*1,211,663*	*740,617*
Alboran Sea	6,342	10,959	16,275	21,371	20,968	35,907	21,535	13,590	9,539
South-west Mediterranean (west)	17,449	47,886	72,243	95,294	100,384	161,169	145,514	56,166	69,331
North-west Mediterranean	30,805	45,479	67,685	89,690	83,412	191,490	196,005	171,752	223,180
South-west Mediterranean (west)	10,685	16,657	24,942	33,236	31,599	61,575	61,993	49,323	55,912
Tyrrhenian Sea (south)	16,957	38,779	57,549	75,132	56,659	114,497	96,344	50,835	53,963
Tyrrhenian Sea (north)	896	1,561	2,237	2,634	1,481	2,142	1,580	253	4
Ionian Sea (western part)	1,653	4,639	7,198	9,564	8,650	3,940	2,170	190	12
Ionian Sea (south-east)	17,742	40,337	60,717	81,088	62,211	159,398	221,733	222,826	61,844
Ionian Sea (north-east)	15,326	41,327	61,882	81,801	66,797	155,103	135,685	113,496	30,031
Adriatic Sea (south)	6,810	16,396	24,338	31,717	15,676	33,321	40,965	13,077	735
Adriatic Sea (north)	829	2,205	3,246	4,300	2,842	2,763	0	0	0
Levantine Sea (west)	22,364	44,110	65,852	87,662	81,431	177,629	220,786	177,964	74,145
Aegean Sea	18,221	43,919	66,176	88,224	61,079	142,131	124,526	44,898	11,603
Levantine Sea (central-north)	24,633	49,826	74,651	99,795	112,692	235,906	241,964	228,650	129,522
Levantine Sea (central-south)	9,875	24,679	37,210	50,477	53,779	101,277	75,719	44,263	16,952
Levantine Sea (east)	4,132	10,635	15,895	20,916	11,254	28,220	33,299	24,380	3,844

Table A.3: Number of observations from Argo floats of salinity in 2017-2019, segmented by layer and region within the Mediterranean Sea.

Region	0-10m	10-30m	30-60m	60-100m	100-150m	150-300m	300-600m	600-1000m	1000-2000m
Mediterranean Sea	*204,580*	*425,631*	*629,756*	*856,953*	*766,421*	*1,606,732*	*1,620,244*	*1,211,848*	*740,684*
Alboran Sea	6,231	10,368	16,120	21,361	20,968	35,907	21,535	13,590	9,539
South-west Mediterranean (west)	17,355	45,007	69,580	94,936	100,365	161,169	145,514	56,166	69,331
North-west Mediterranean	30,615	44,007	65,036	88,733	83,286	191,490	196,005	171,752	223,180
South-west Mediterranean (west)	10,668	16,414	24,224	32,926	31,571	61,575	61,993	49,323	55,912
Tyrrhenian Sea (south)	16,880	37,781	56,197	74,537	56,664	114,497	96,344	50,835	53,963
Tyrrhenian Sea (north)	896	1,520	2,187	2,634	1,481	2,142	1,580	253	4
Ionian Sea (western part)	1,653	4,276	6,732	9,513	8,650	3,940	2,170	190	12
Ionian Sea (south-east)	17,740	39,495	58,589	79,915	62,027	159,395	221,733	222,826	61,844
Ionian Sea (north-east)	15,287	40,218	59,075	81,356	66,755	155,103	135,685	113,496	30,031
Adriatic Sea (south)	6,805	15,639	23,733	31,609	15,676	33,321	40,965	13,077	735
Adriatic Sea (north)	825	1,972	3,106	4,300	2,842	2,763	0	0	0
Levantine Sea (west)	22,343	42,927	61,035	79,384	77,406	177,617	220,786	177,964	74,145
Aegean Sea	18,935	43,645	64,197	87,488	61,085	142,206	124,676	44,923	11,603
Levantine Sea (central-north)	24,318	47,339	69,168	98,065	112,544	235,900	241,964	228,650	129,522
Levantine Sea (central-south)	9,898	24,649	36,132	49,854	53,847	101,487	75,995	44,423	17,019
Levantine Sea (east)	4,131	10,374	14,645	20,342	11,254	28,220	33,299	24,380	3,844

Table A.4: Number of observations from Argo floats of temperature in 2017-2019, segmented by layer and region within the Mediterranean Sea.

B The characteristics of tides and their effects on the general circulation of the Mediterranean Sea: Supplementary material

B.1 Preliminary experiments

As discussed in Section 2 and Table 2 of the manuscript, there are some differences between the two experiments which are not directly related to the implementation of tidal forcing. Some preliminary experiments were carried out to assess the impact of changing the timestep and time-stepping scheme, as was required for stability in the tidal experiment.

Figure B.1 shows the differences in sea surface height and currents over a four-year experiment with a change in the time integration scheme. From this, we see that changes in sea surface height are on the order of 5 mm, and currents change on the order of 5×10^{-4} ms^{-1}. These are both negligible with respect to the changes due to tidal forcing. Changes in salinity (Fig. B.2) are also negligible, on the order of 10^{-4} PSU, which is 10% of the magnitude of the changes due to tides (see Section 6 of the manuscript).

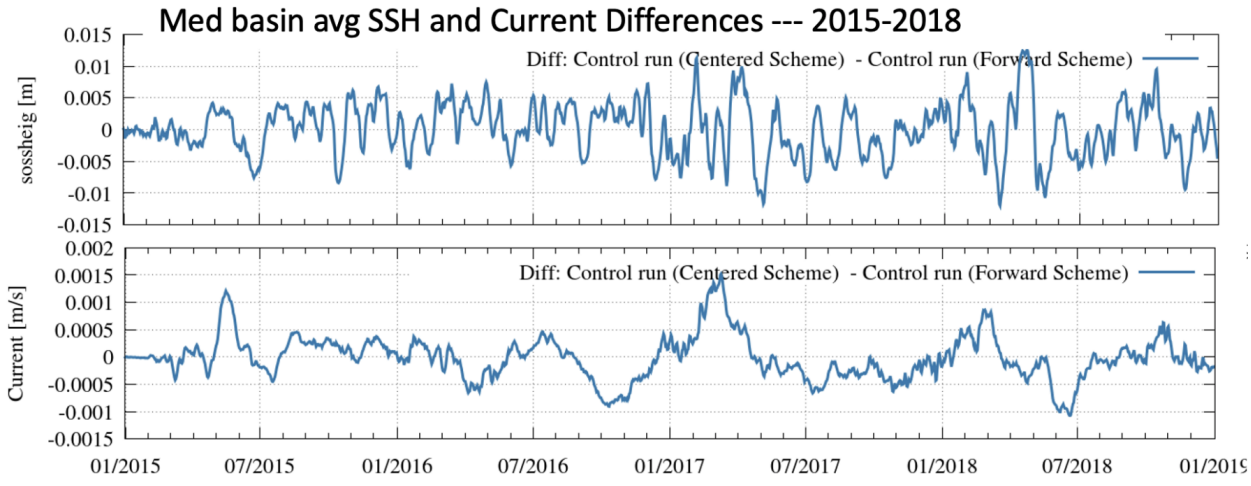

Figure B.1: Differences between Mediterranean Sea average sea level (top) and currents (bottom), computed from control runs with forward and centred time integration schemes.

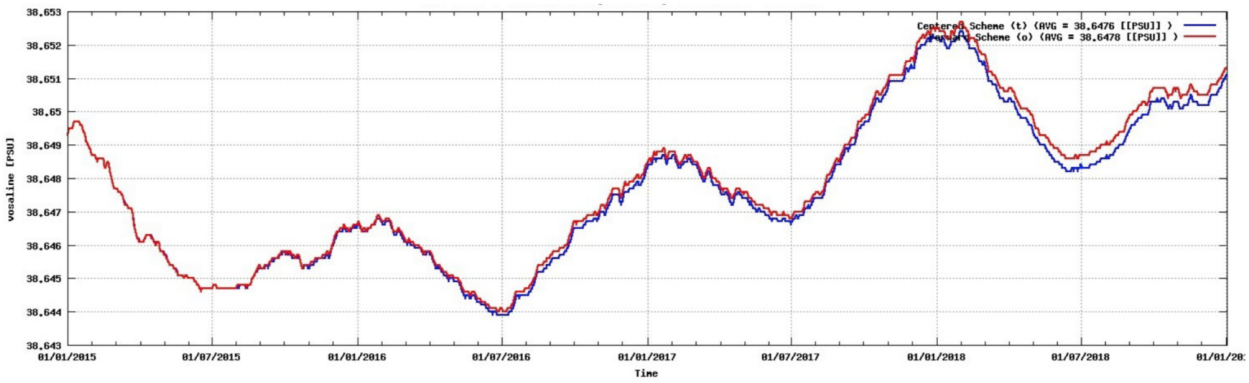

Figure B.2: Time-series of Mediterranean Sea average salinity, computed from control runs with forward and centred time integration schemes. The centred time integration scheme is in blue and the forward scheme is in red.

B.2 The Gibraltar Strait

Mass transport at the Gibraltar Strait is affected by tides, as was shown by authors including Gonzalez et al. (2023), Harzallah et al. (2014), and Naranjo et al. (2014). Net water mass transport through the strait at a given longitude, over the five-year period, was calculated as:

$$\bar{Q}(x) = \int_{South}^{North} \int_{z}^{\eta} \bar{u} dz dy \tag{4.5}$$

where $\bar{Q}$ is the net water mass transport, η is the sea surface height, z is the depth, and $\bar{u}$ is the mean zonal velocity. This transport can be split into eastward and westward components:

$$\bar{Q}_{in}(x) = \int_{South}^{North} \int_{z}^{\eta} \bar{u} H(u) dz dy \tag{4.6}$$

$$\bar{Q}_{out}(x) = \int_{South}^{North} \int_{z}^{\eta} \bar{u} H(-u) dz dy \tag{4.7}$$

where Q_{in} is the upper-layer eastward transport, Q_{out} is the lower-layer westward transport, and H is the Heaviside step function, $H = 1$ if $u > 0$, $H = 0$ otherwise.

The effects of tides on the Gibraltar Strait mass transport are detailed in Table B.1. Al-

Experiment	Inflow ($\bar{Q}_{in}$)	Outflow ($\bar{Q}_{out}$)	Net Transport ($\bar{Q}$)
Model without tides	0.85 Sv	-0.80 Sv	0.045 Sv
Tidal model	0.88 Sv	-0.84 Sv	0.043 Sv
Observations (Soto-Navarro et al., 2010)	0.81$\pm$0.06 Sv	-0.78$\pm$0.05 Sv	0.038$\pm$0.007 Sv

Table B.1: Mass transport at the 5.48°W section of the Gibraltar Strait in the experiment without tides, tidal experiment, and observations from Soto-Navarro et al. (2010). Values for model outputs are calculated as mean inflow and outflow transport in the Gibraltar Strait for the period 2017-2021.

though the net transport in the Gibraltar Strait is not largely affected by tides, both the inflow and outflowing transport are increased by tides. Within observational errors we cannot fully distinguish between the tide and no-tide experiments, but we can estimate a 5-10% larger inflow/outflow transport with respect to literature. We argue that this is due to the relatively coarse resolution of the model in the Gibraltar Strait, since Sannino et al. (2009) demonstrated that the required resolution for an accurate representation of the Gibraltar Strait would be at the sub-kilometer scale, many times greater than the one used in our model.

B.3 Spectra of additional regions

The kinetic energy analysis in Section 4 of the manuscript for three points (Gibraltar Strait, Tyrrhenian Sea, and Cretan Sea) are discussed, but six additional points were analysed, as shown in Fig. 4 of the manuscript. Figures equivalent to Figs 5-12 in the manuscript, but for these six points, are presented here. The figures are organised alphabetically by region. Note that only barotropic spectra of the Gulf of Gabes and North Adriatic are shown, since the regions are shallow.

B.3.1 Gulf of Gabes

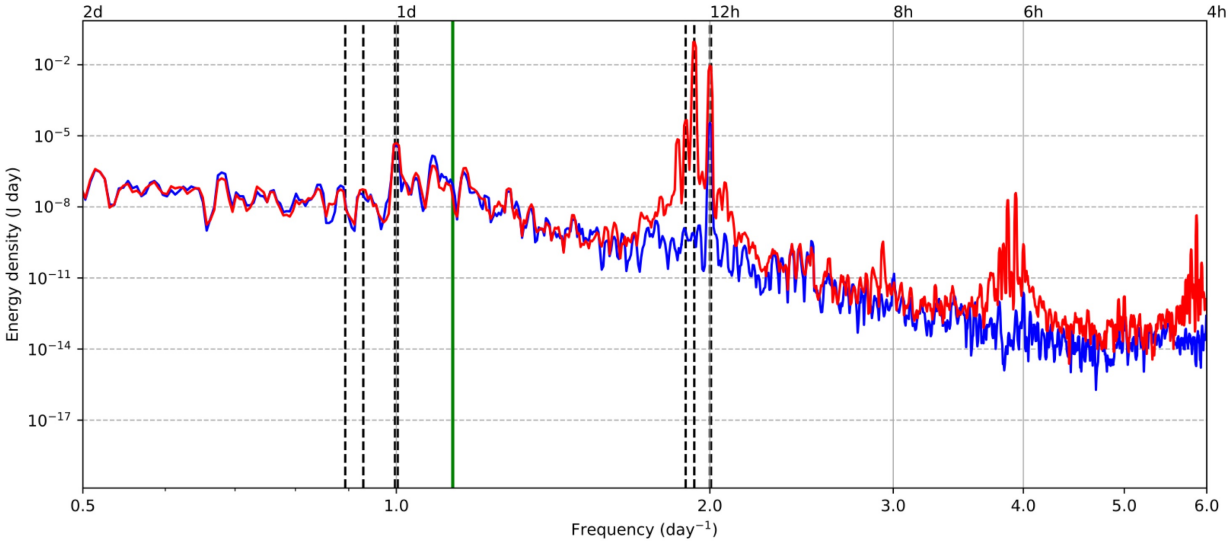

Figure B.3: Barotropic rotary spectrum of kinetic energy density at the Gulf of Gabes point (34.52°N, 11.42°E), averaged across all depths, for a six-month period (January-June 2019). Dashed lines represent the eight tidal components included in the model, and the green line is the inertial frequency.

B.3.2 Gulf of Lion

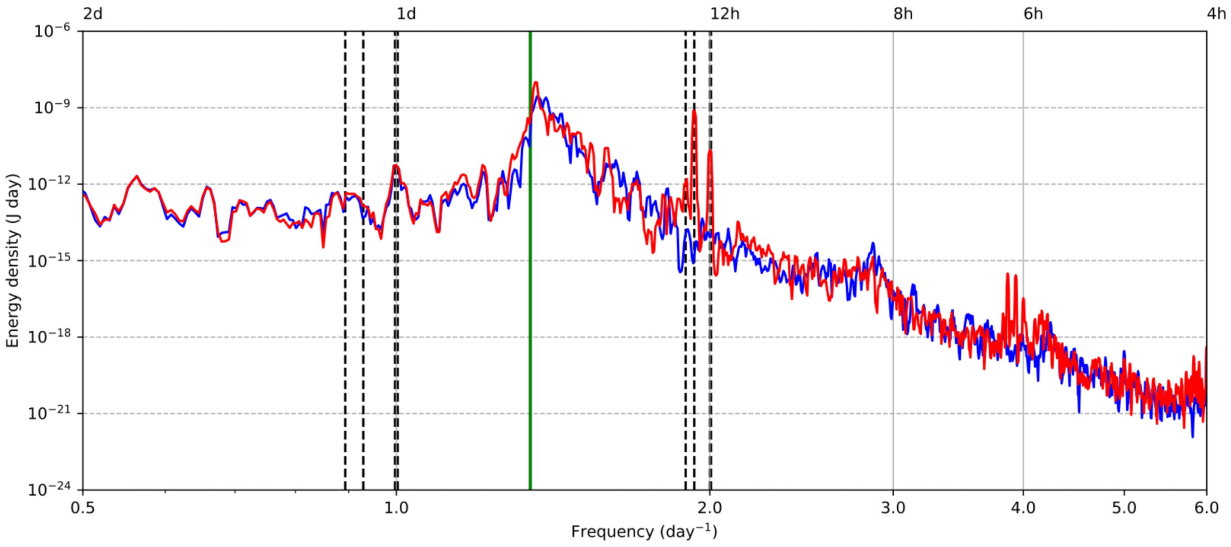

Figure B.4: Barotropic rotary spectrum of kinetic energy density at the Gulf of Lion point (42.27°N, 5.25°E), averaged across all depths, for a six-month period (January-June 2019). Dashed lines represent the eight tidal components included in the model, and the green line is the inertial frequency.

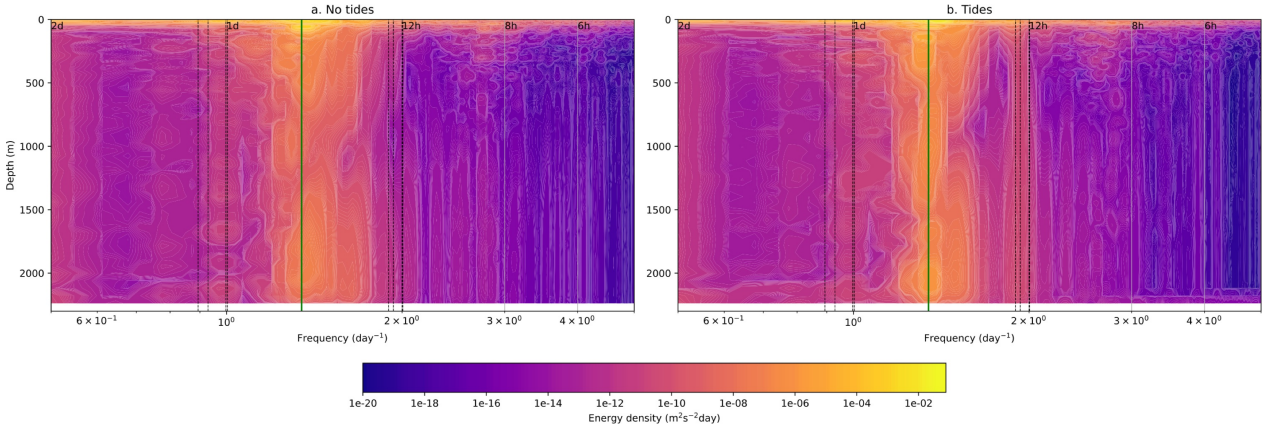

Figure B.5: Rotary spectrum of kinetic energy density at the Gulf of Lion point (42.27°N, 5.25°E), for all depths, in May 2019. Dashed lines represent the eight tidal components included in the model, and the green line is the inertial frequency.

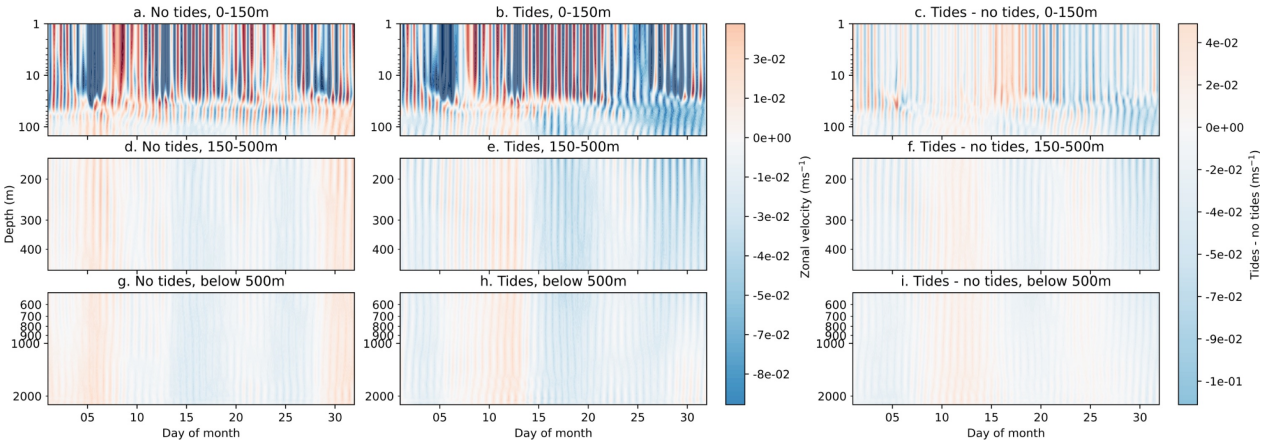

Figure B.6: Hovmoller plots of depth against time of hourly mean zonal velocity at a point at the Gulf of Lion point (42.27°N, 5.25°E) in May 2019, for a. Model without tides, 0-150m, b. Tidal model, 0-150m, c. Tidal model – model without tides, 0-150m, d. Model without tides, 150-500m, e. Tidal model, 150-500m, f. Tidal model – model without tides, g. Model without tides, below 500m, h. Tidal model, below 500m, i. Tidal model – model without tides, below 500m. Note that the depth scale is logarithmic.

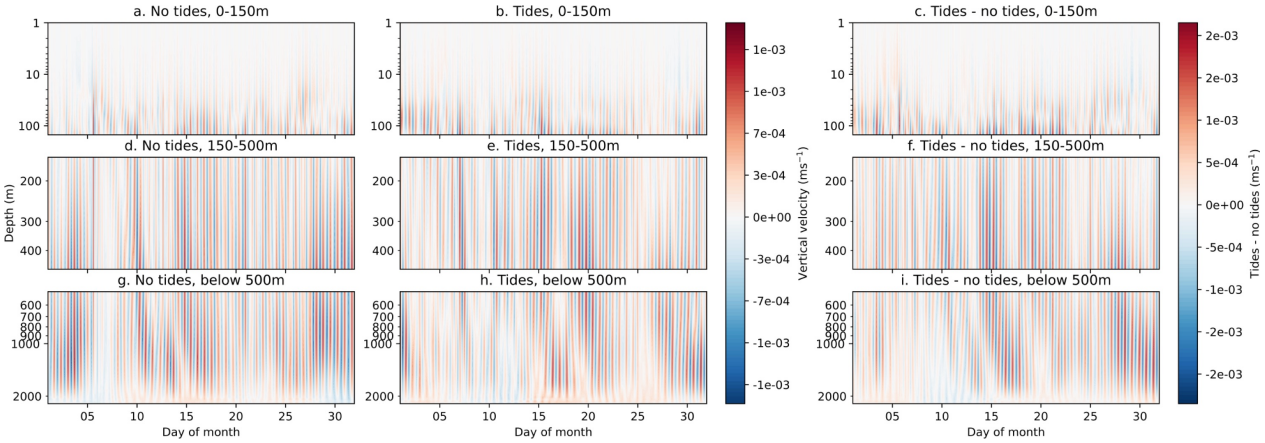

Figure B.7: Hovmoller plots of depth against time of hourly mean vertical velocity at a point at the Gulf of Lion point (42.27°N, 5.25°E) in May 2019, for a. Model without tides, 0-150m, b. Tidal model, 0-150m, c. Tidal model – model without tides, 0-150m, d. Model without tides, 150-500m, e. Tidal model, 150-500m, f. Tidal model – model without tides, g. Model without tides, below 500m, h. Tidal model, below 500m, i. Tidal model – model without tides, below 500m. Note that the depth scale is logarithmic.

B.3.3 Ionian Sea

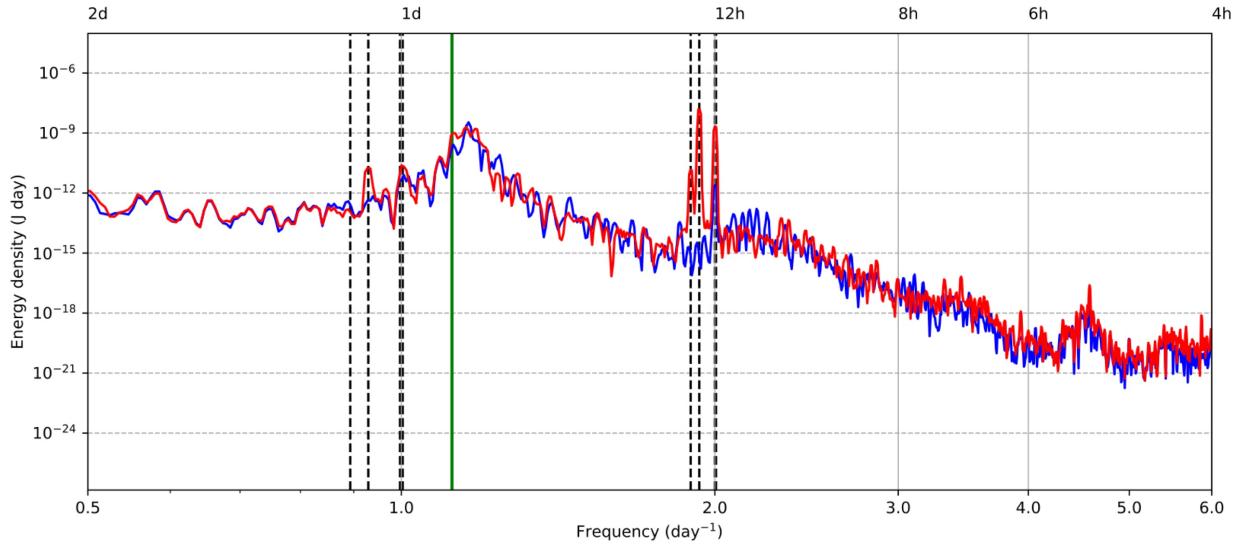

Figure B.8: Barotropic rotary spectrum of kinetic energy density at the Ionian Sea point (34.02°N, 20.00°E), averaged across all depths, for a six-month period (January-June 2019). Dashed lines represent the eight tidal components included in the model, and the green line is the inertial frequency.

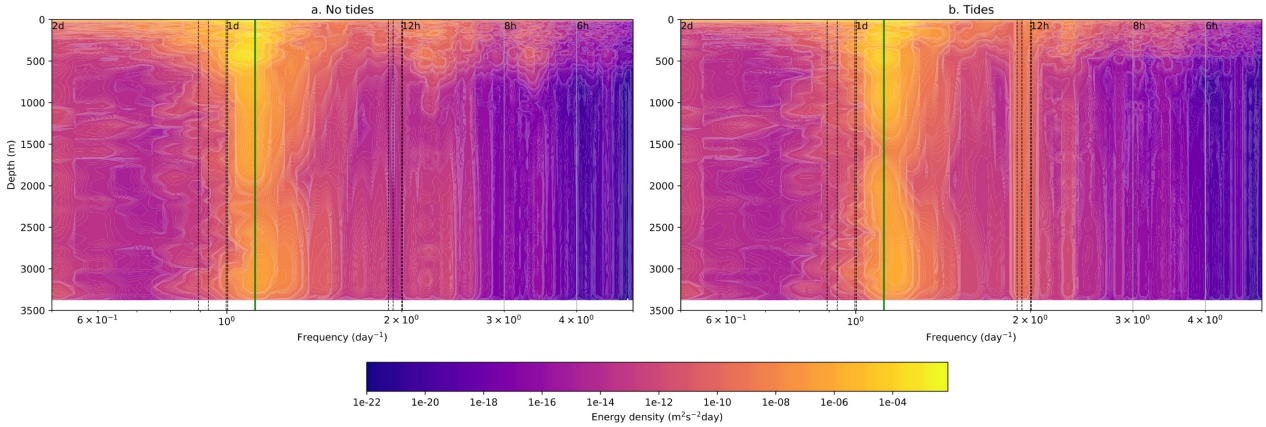

Figure B.9: Rotary spectrum of kinetic energy density at the Ionian Sea point (34.02°N, 20.00°E), for all depths, in May 2019. Dashed lines represent the eight tidal components included in the model, and the green line is the inertial frequency.

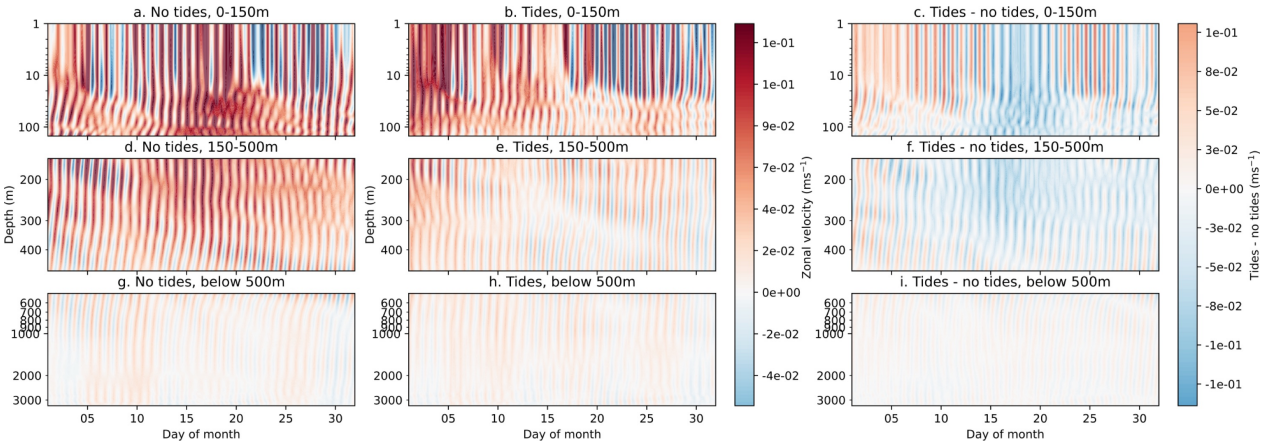

Figure B.10: Hovmoller plots of depth against time of hourly mean zonal velocity at a point at the Ionian Sea point (34.02°N, 20.00°E) in May 2019, for a. Model without tides, 0-150m, b. Tidal model, 0-150m, c. Tidal model – model without tides, 0-150m, d. Model without tides, 150-500m, e. Tidal model, 150-500m, f. Tidal model – model without tides, g. Model without tides, below 500m, h. Tidal model, below 500m, i. Tidal model – model without tides, below 500m. Note that the depth scale is logarithmic.

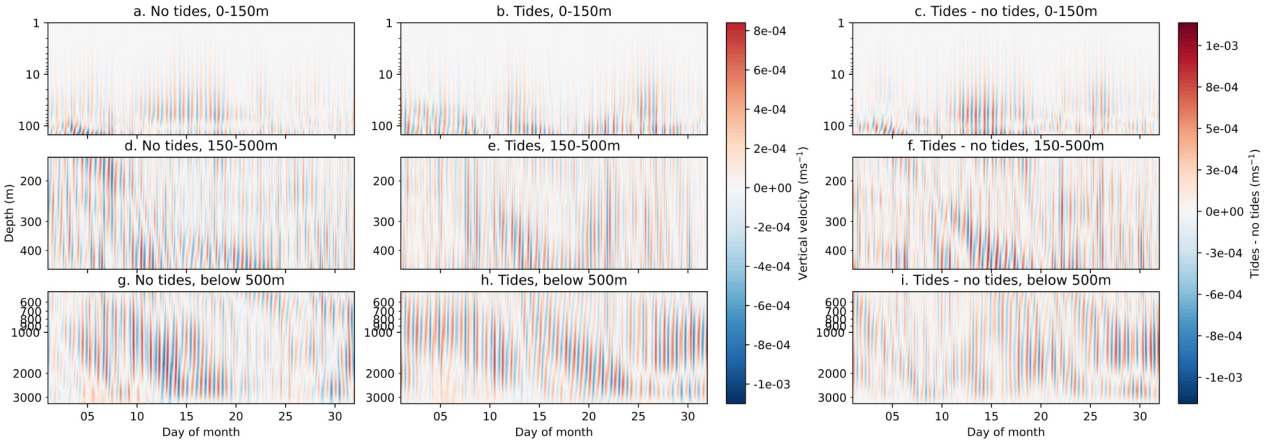

Figure B.11: Hovmoller plots of depth against time of hourly mean vertical velocity at a point at the Ionian Sea point (34.02°N, 20.00°E) in May 2019, for a. Model without tides, 0-150m, b. Tidal model, 0-150m, c. Tidal model – model without tides, 0-150m, d. Model without tides, 150-500m, e. Tidal model, 150-500m, f. Tidal model – model without tides, g. Model without tides, below 500m, h. Tidal model, below 500m, i. Tidal model – model without tides, below 500m. Note that the depth scale is logarithmic.

B.3.4 North Adriatic Sea

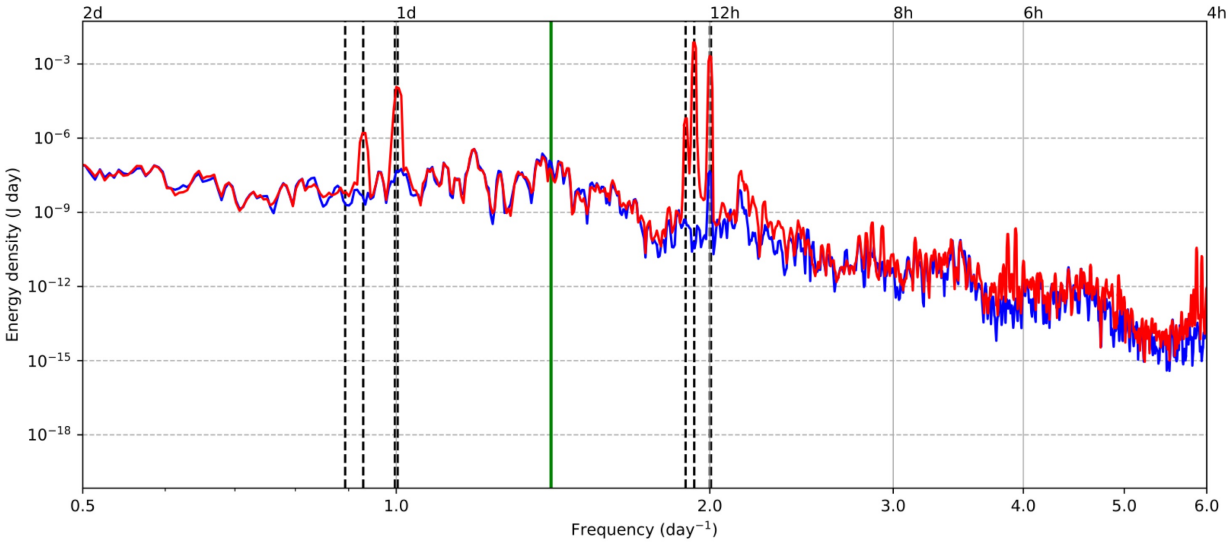

Figure B.12: Barotropic rotary spectrum of kinetic energy density at the North Adriatic Sea point (44.77°N, 13.00°E), averaged across all depths, for a six-month period (January-June 2019). Dashed lines represent the eight tidal components included in the model, and the green line is the inertial frequency.

B.3.5 Rhodes Gyre

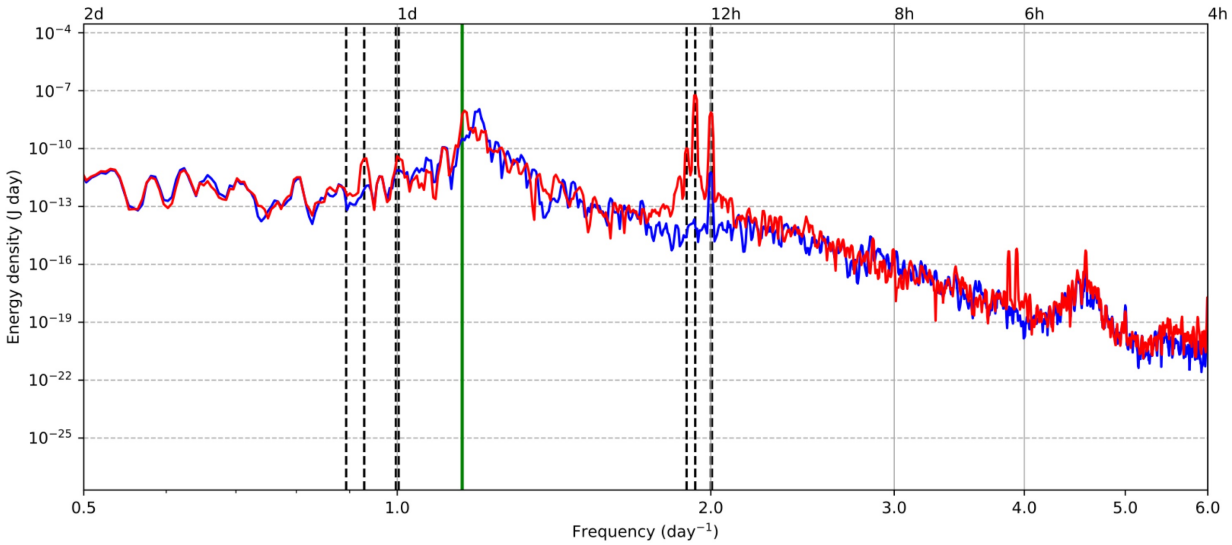

Figure B.13: Barotropic rotary spectrum of kinetic energy density at the Rhodes Gyre point (35.27°N, 28.25°E), averaged across all depths, for a six-month period (January-June 2019). Dashed lines represent the eight tidal components included in the model, and the green line is the inertial frequency.

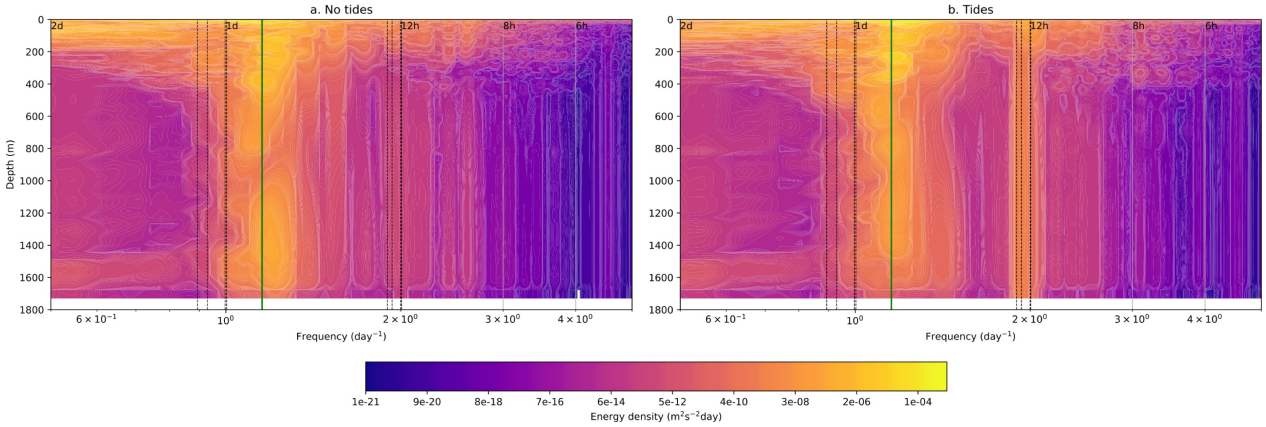

Figure B.14: Rotary spectrum of kinetic energy density at the Rhodes Gyre point (35.27°N, 28.25°E), for all depths, in May 2019. Dashed lines represent the eight tidal components included in the model, and the green line is the inertial frequency.

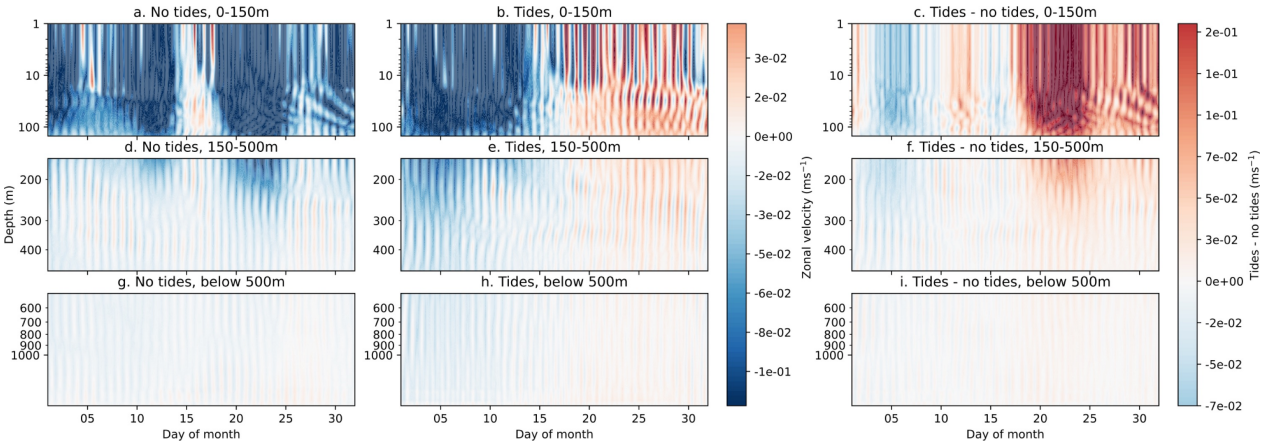

Figure B.15: Hovmoller plots of depth against time of hourly mean zonal velocity at a point at the Rhodes Gyre point (35.27°N, 28.25°E) in May 2019, for a. Model without tides, 0-150m, b. Tidal model, 0-150m, c. Tidal model – model without tides, 0-150m, d. Model without tides, 150-500m, e. Tidal model, 150-500m, f. Tidal model – model without tides, g. Model without tides, below 500m, h. Tidal model, below 500m, i. Tidal model – model without tides, below 500m. Note that the depth scale is logarithmic.

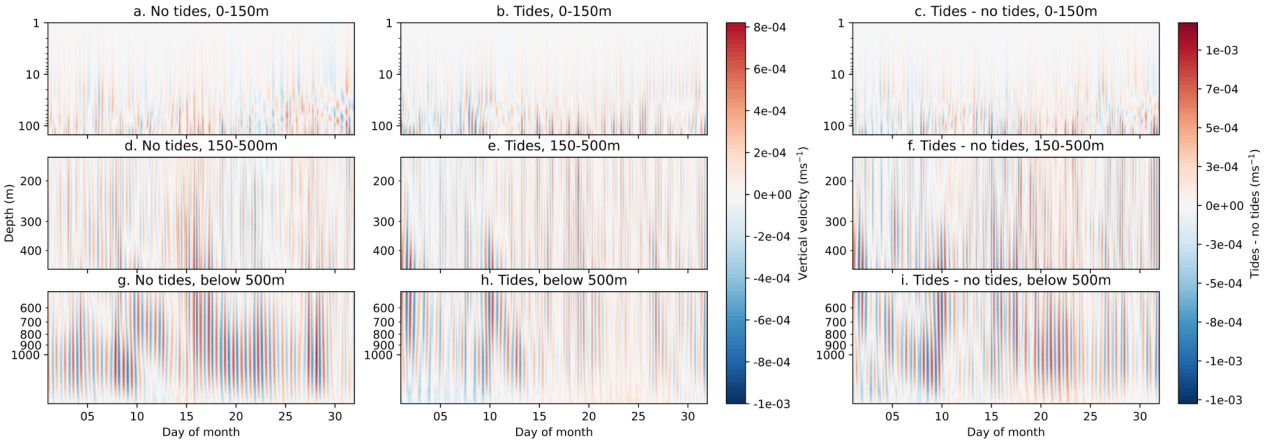

Figure B.16: Hovmoller plots of depth against time of hourly mean vertical velocity at a point at the Rhodes Gyre point (35.27°N, 28.25°E) in May 2019, for a. Model without tides, 0-150m, b. Tidal model, 0-150m, c. Tidal model – model without tides, 0-150m, d. Model without tides, 150-500m, e. Tidal model, 150-500m, f. Tidal model – model without tides, g. Model without tides, below 500m, h. Tidal model, below 500m, i. Tidal model – model without tides, below 500m. Note that the depth scale is logarithmic.

B.3.6 South Adriatic Sea

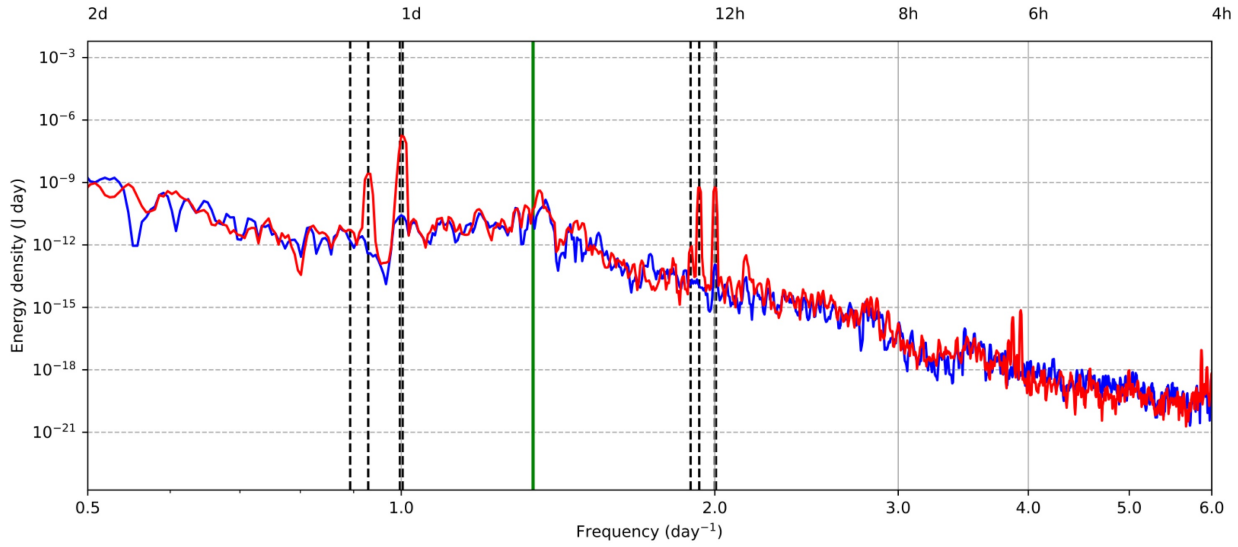

Figure B.17: Barotropic rotary spectrum of kinetic energy density at the South Adriatic Sea point (42.02°N, 18.00°E), averaged across all depths, for a six-month period (January-June 2019). Dashed lines represent the eight tidal components included in the model, and the green line is the inertial frequency.

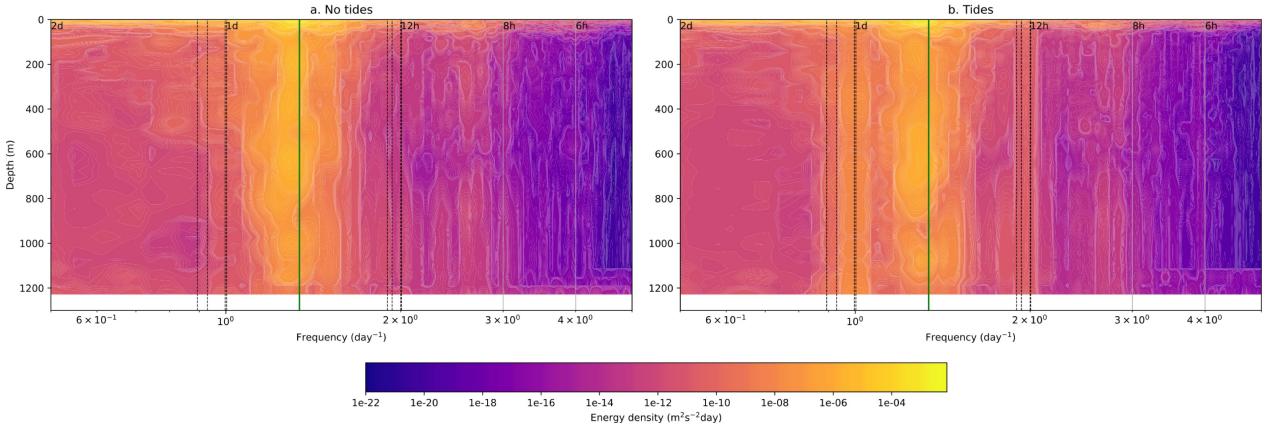

Figure B.18: Rotary spectrum of kinetic energy density at the South Adriatic Sea point (42.02°N, 18.00°E), for all depths, in May 2019. Dashed lines represent the eight tidal components included in the model, and the green line is the inertial frequency.

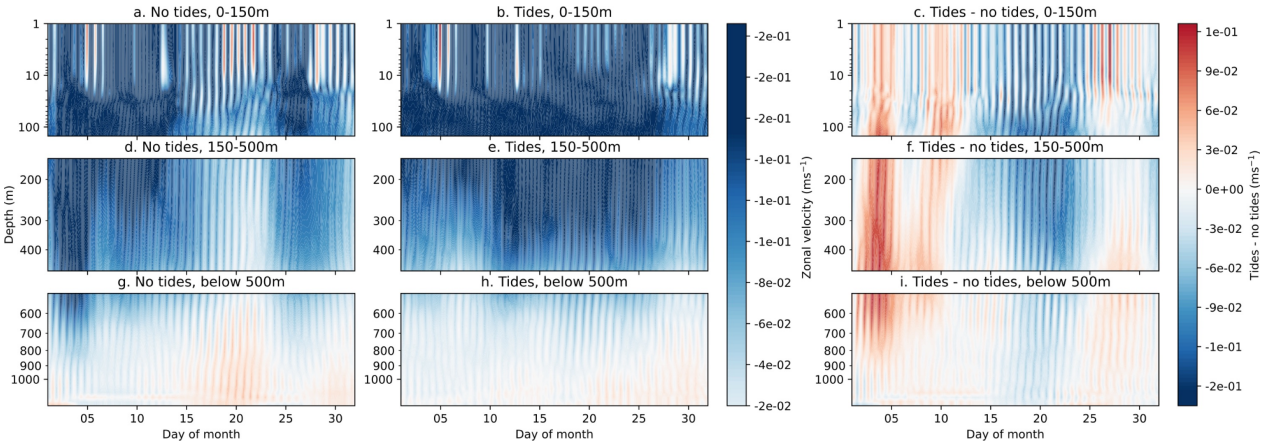

Figure B.19: Hovmoller plots of depth against time of hourly mean zonal velocity at a point at the South Adriatic Sea point (42.02°N, 18.00°E) in May 2019, for a. Model without tides, 0-150m, b. Tidal model, 0-150m, c. Tidal model – model without tides, 0-150m, d. Model without tides, 150-500m, e. Tidal model, 150-500m, f. Tidal model – model without tides, g. Model without tides, below 500m, h. Tidal model, below 500m, i. Tidal model – model without tides, below 500m. Note that the depth scale is logarithmic.

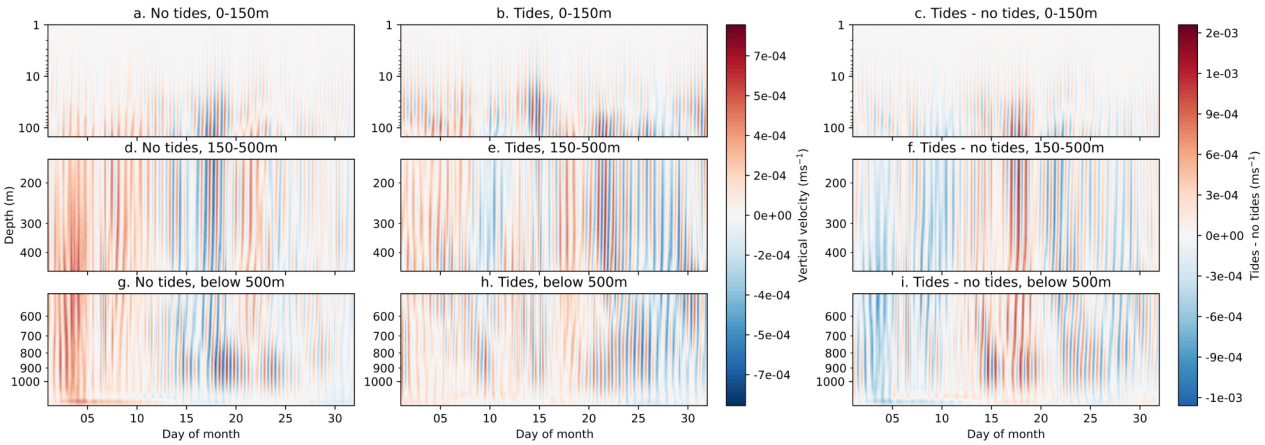

Figure B.20: Hovmoller plots of depth against time of hourly mean vertical velocity at a point at the South Adriatic Sea point (42.02°N, 18.00°E) in May 2019, for a. Model without tides, 0-150m, b. Tidal model, 0-150m, c. Tidal model – model without tides, 0-150m, d. Model without tides, 150-500m, e. Tidal model, 150-500m, f. Tidal model – model without tides, g. Model without tides, below 500m, h. Tidal model, below 500m, i. Tidal model – model without tides, below 500m. Note that the depth scale is logarithmic.

C Internal tides in the Mediterranean Sea: Model intercomparison

The generation, distribution, and propagation routes of internal tides in the Mediterranean Sea in NEMO and ICON experiment outputs are compared to one another in Chapter 4. Although the two experiments give broadly similar results, they differ in the exact generation sites and particularly in the wavelengths of the first modes of the M2 and K1 internal tides. One reason for this could be different representation of barotropic lunisolar tides in the two models. Here we briefly compare the barotropic tides in the two experiments.

The tidal amplitudes and phases were calculated through a harmonic analysis of sea surface height and compared to data from TPXO9 (Egbert and Ray, 2003). Amplitudes and phases, and the vector difference between each experiment and TPXO9, for the principal semidiurnal and diurnal tidal components (M2 and K1) are shown in Figures C.1 and C.2. For the analysed month, placements of the maximum amplitudes and amphidromic points are broadly correct in both the experiments within the Mediterranean Sea. However, it is clear that the models do not always correctly capture the tidal amplitude in key locations for internal tide generation. In the ICON implementation, areas close to the Gibraltar and Sicily Straits have particularly large differences from TPXO9 for the M2 component, and for the K1 component, the tidal amplitude is greatly underestimated in the western Mediterranean basin. In the NEMO experiment, the underestimation of K1 amplitude is limited to fewer areas, but notably is overestimated in the north Adriatic Sea, where K1 is typically large. The NEMO experiment represents the M2 component fairly well, with underestimation of tidal amplitude limited to a few regions.

Since the NEMO model includes eight tidal components, the root mean square error of the NEMO and ICON tidal amplitudes compared to TPXO9 were calculated for these eight components and are summarised in Figure C.3. NEMO has lower root mean square errors than ICON for all components apart from P1.

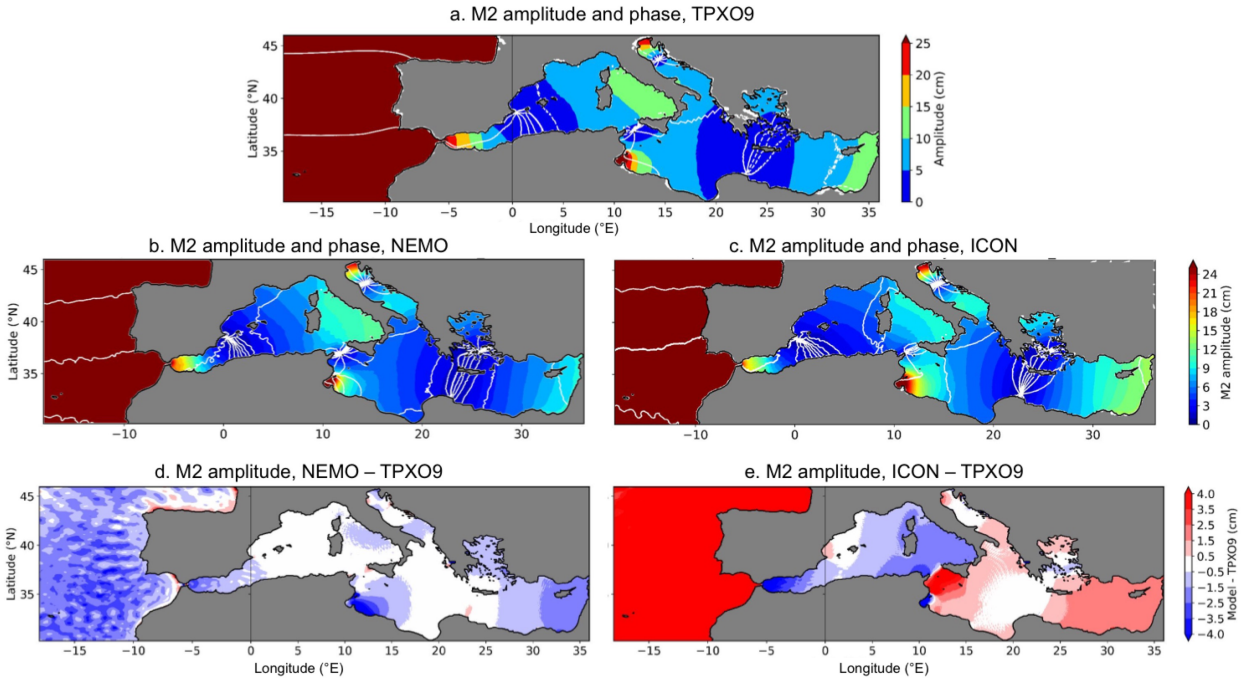

Figure C.1: Amplitude and phase of M2 tidal component in a. TPXO9, b. NEMO, and c. ICON for March 2022, and the amplitude difference between TPXO9 and d. NEMO and e. ICON.

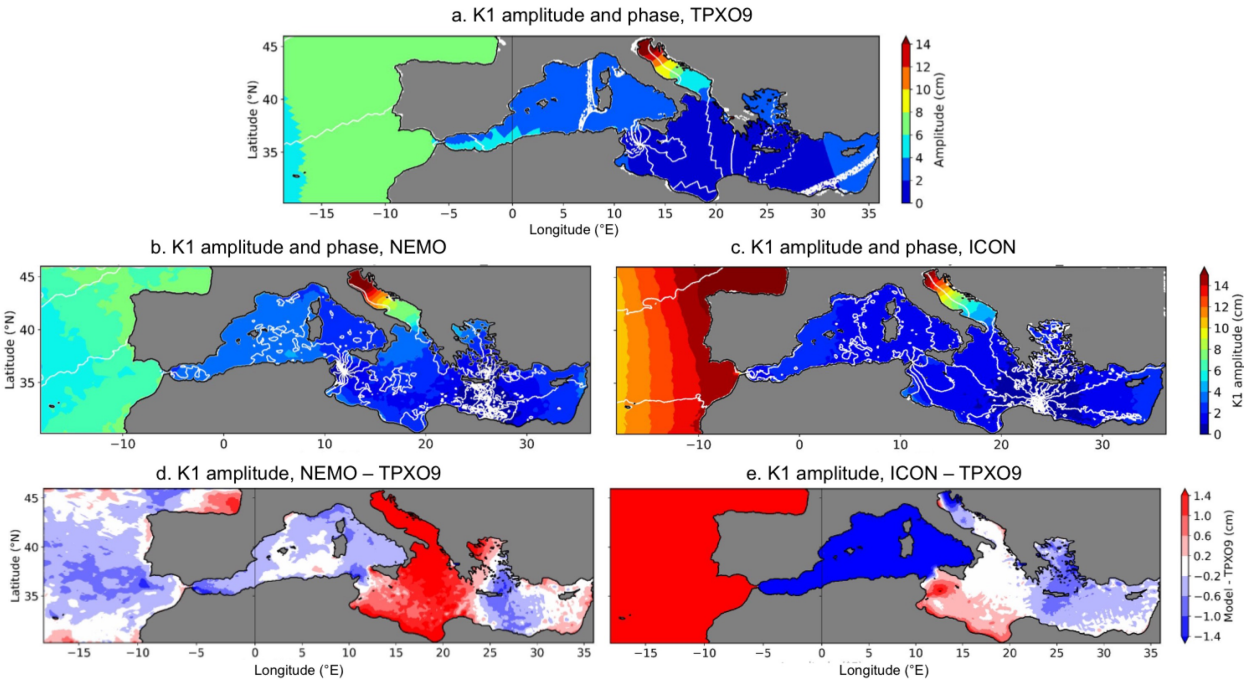

Figure C.2: Amplitude and phase of K1 tidal component in a. TPXO9, b. NEMO, and c. ICON for March 2022, and the amplitude difference between TPXO9 and d. NEMO and e. ICON.

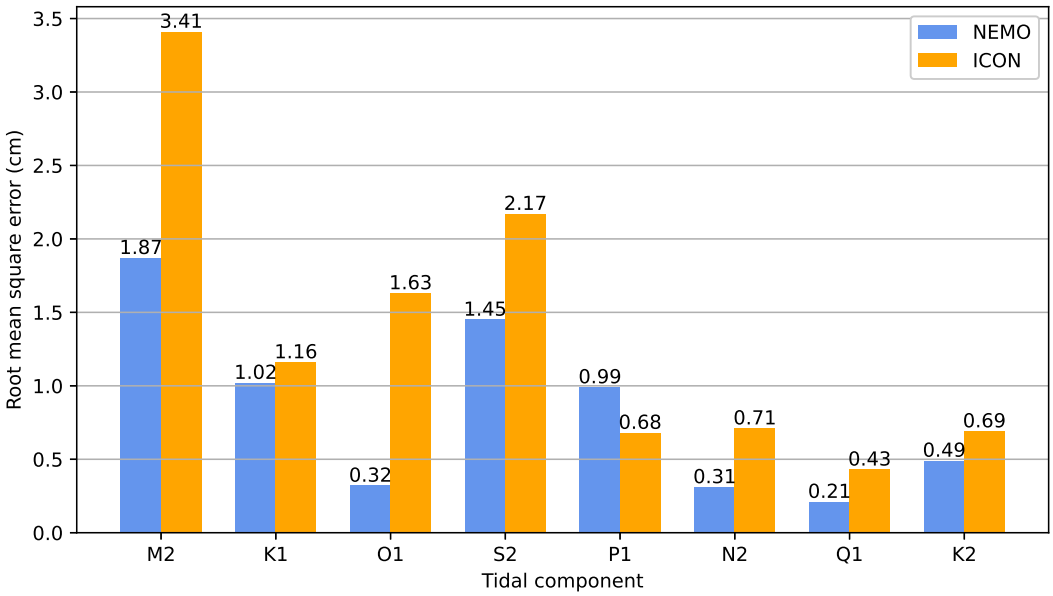

Figure C.3: Root mean square error of model tidal amplitude for eight tidal components compared to TPXO9 in the Mediterranean Sea for March 2022. NEMO is in blue and ICON is shown in orange.

D Internal tides in the Mediterranean Sea: Additional regional analysis

In Chapter 4.3.1, rotary spectra of three points: the Gibraltar Strait, Sicily Strait, and Ionian Sea (north), were shown. Spectra of the remaining points from Figure 4.1 are in the following figures.

D.1 Aegean Sea

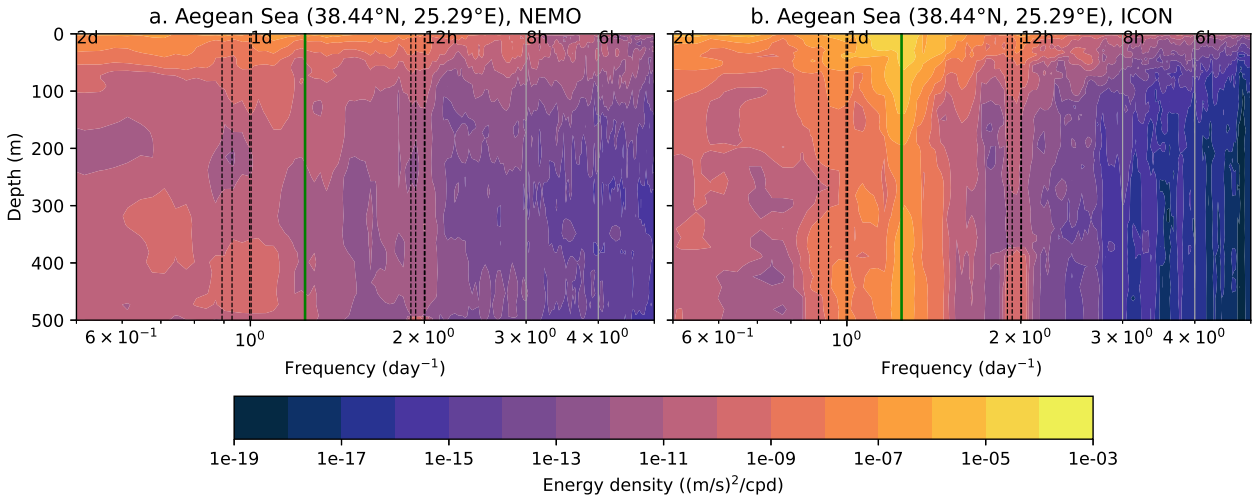

Figure D.1: Rotary spectra of baroclinic kinetic energy in the Aegean Sea (38.44°N, 25.29°E), for a. NEMO, and b. ICON, through all depths. Green vertical line is the inertial frequency at this latitude.

D.2 Algerian Sea

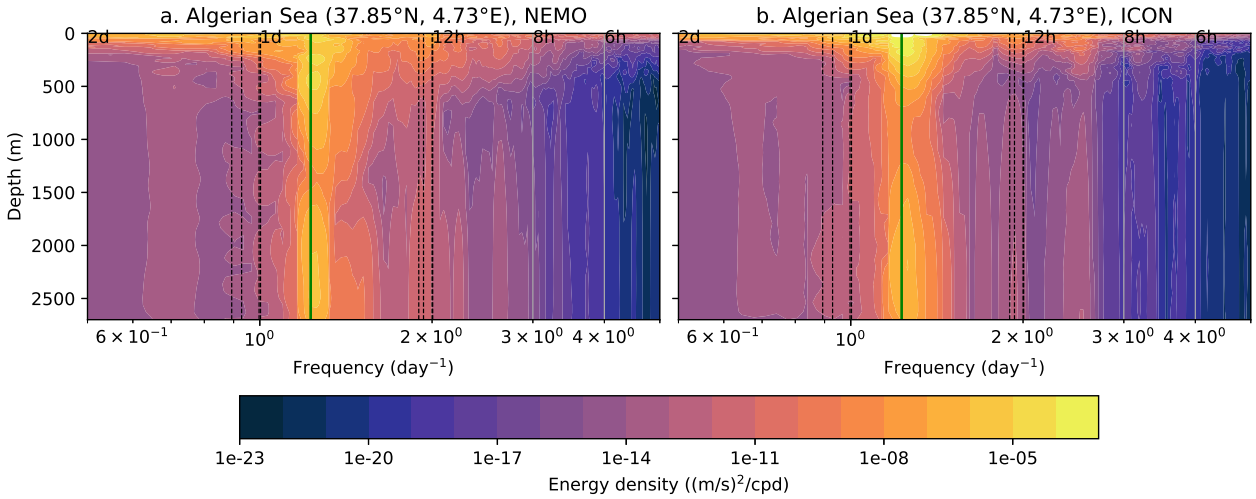

Figure D.2: Rotary spectra of baroclinic kinetic energy in the Algerian Sea (37.85°N, 4.73°E), for a. NEMO, and b. ICON, through all depths. Green vertical line is the inertial frequency at this latitude.

D.3 Ionian Sea (South)

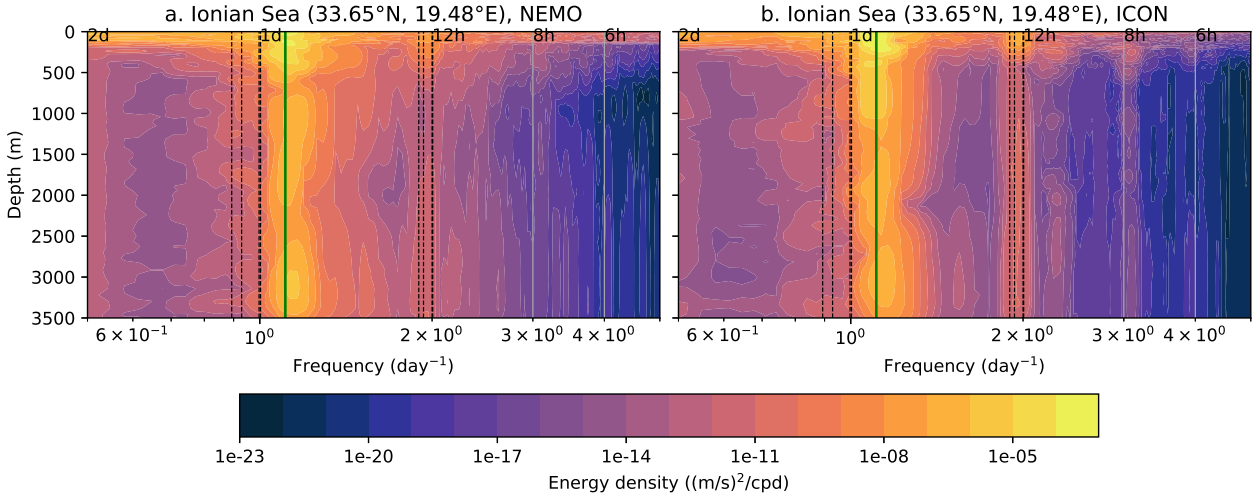

Figure D.3: Rotary spectra of baroclinic kinetic energy in the Ionian Sea (33.65°N, 19.48°E), for a. NEMO, and b. ICON, through all depths. Green vertical line is the inertial frequency at this latitude.

D.4 North Adriatic Sea

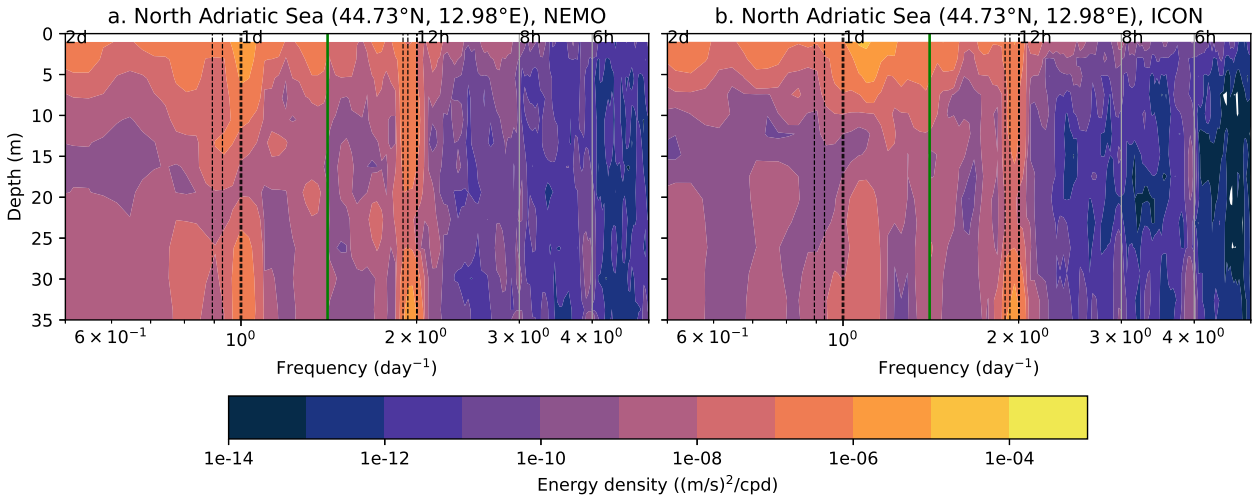

Figure D.4: Rotary spectra of baroclinic kinetic energy in the North Adriatic Sea (44.73°N, 12.98°E), for a. NEMO, and b. ICON, through all depths. Green vertical line is the inertial frequency at this latitude.

D.5 Tyrrhenian Sea

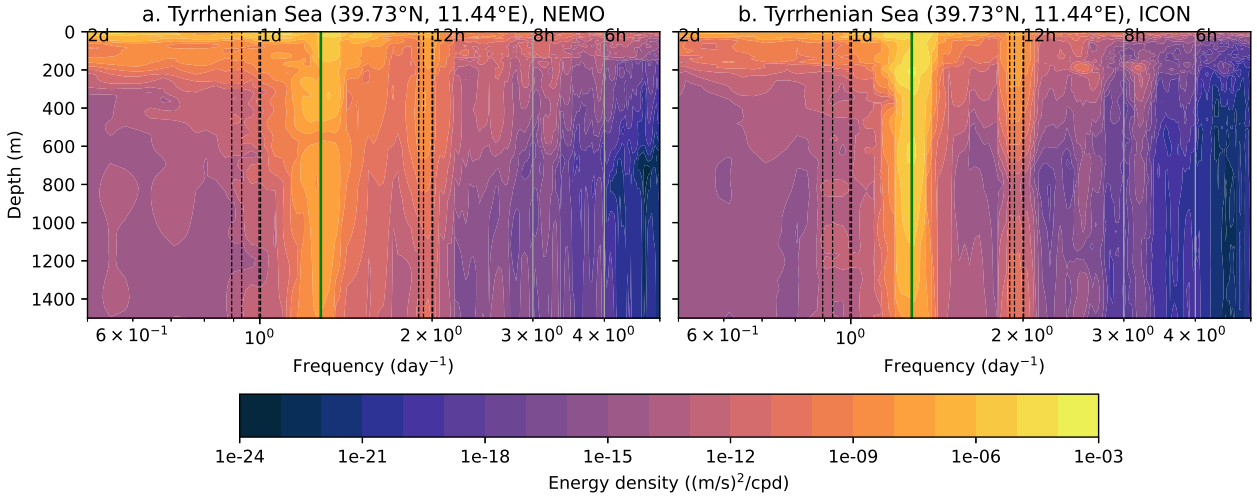

Figure D.5: Rotary spectra of baroclinic kinetic energy in the Tyrrhenian Sea (39.73°N, 11.44°E), for a. NEMO, and b. ICON, through all depths. Green vertical line is the inertial frequency at this latitude.